Electrospinning Scaffold Fabrication of Polymer Nanofibers and Sensors for Tissue Engineering Applications

Dennis LeRoy Edmondson

A dissertation
submitted in partial fulfillment of the
requirements for the degree of

Doctor of Philosophy

University of Washington

2013

Reading Committee:

Miqin Zhang, Chair

Richard Ellenbogen

James Park

Program Authorized to Offer Degree:

Materials Science and Engineering

University of Washington

ABSTRACT

Electrospinning Scaffold Fabrication of Polymer
Nanofibers and Sensors for Tissue Engineering Applications

Dennis LeRoy Edmondson

Chair of the Supervisory Committee:

Professor Miqin Zhang, PhD
Materials Science and Engineering

Well-ordered one-dimensional nanostructures (nanofibers) are enabling important new applications in textile, energy, structural, environmental, and bioengineering applications such as sensors, transducers, and energy harvesters, due to their unique anisotropic properties. Through electrospinning, polymeric, ceramic or metallic solutions can be ejected from an electrically charged syringe needle spinneret at an appropriate flow rate, collection distance, and voltage to form nanofiber filaments. A substantial electrical field gradient of 6,000 to 25,000 volts is required, depending on solution type, in the space between the charged syringe needle spinneret and an electrically grounded collection electrode. As solution flows from the syringe needle, Coulomb forces created by electrical charge on fibers can extend the stream into a fine, continuous group of filaments. The short transition from spinneret blunt needle tip to the stream occurs through formation of a Taylor cone droplet at an angle of around 30 degrees to the needle tip axis, which is a common characteristic for charged fluids in motion within

electric field gradients. The electric field gradient accelerates the filament stream onto a collecting target of opposite polarity between eight and thirty centimeters away. For best circumstances the polymeric solution should be dry upon reaching the grounded collecting electrode to yield a dry fibrous mat.

Resultant fiber diameter (or shape), porosity, morphology, and other characteristics can be controlled through modifying electrospinning solution material composition, voltage, solution flow rate (natural or forced), electric field strength, and distance between spinneret needle and fiber collector geometry. The collector component is very significant to the electrospinning process as the fiber collector geometry can be altered to control fiber deposition orientation. Electrospinning fabrication equipment designed for manufacturing nanofibers, especially for highly aligned fibers, can be used to develop effective scaffolds for cell proliferation and chemical attachment. Many electrospinner variations have been tried in the effort to create a bio-cellular scaffold environment on which cells can proliferate. The ability to promote substantial cell growth on an artificial scaffold brings research closer to fabrication of difficult organs, such as heart, neural conduits, intestinal tissue, and skeletal structure, to name but a few. Current laboratory and clinical trials focused on bladder and kidney are searching for the ideal technique for creating a fully functioning replacement organ by identifying the most reliable polymer fiber-cell compatibility scaffold that will both support cell proliferation and be biodegradable. A key aspect is developing a consistent method of aligning fibers through electrospinning. However, the challenges in large-scale production of highly aligned and uniform nanofibers limit the scope of their applications and commercialization.

This dissertation presents a powerful yet economical approach that integrates the concepts of stationary parallel-electrode gap method with centrifugal polymer dispersion to produce nanofibers with a high degree of alignment and uniformity at large scale. This approach was first demonstrated with polyvinylidene fluoride to illustrate how the experimental parameters regulate fiber production and piezoelectric response, leading to the production of aligned nanofibers up to four inches in length. Further work with chitosan and polyethylene oxide, a natural and a synthetic polymer, demonstrated the versatility of the system. The now-patented centrifugal electrospinning technology presented here has already opened new avenues of invention through mass production of aligned nanofibers, allowing development of novel sensors.

One novel device under development is a spiral-coiled biosensor. Biotelemetry has become an important part of medical research for advancing patient care by remotely monitoring continuing biological processes and physiological functions. Current biotelemetry systems are complex and require multiple electronic components to function, for example, battery, sensor element, and transmitter circuit. Another significant concern of current biotelemetry devices is direct wire coupling of the *in vivo* portion to external supporting equipment. Without the need for a power supply, the spirally coiled sensors in the nanofiber bundle generate and transmit an electrical signal wirelessly in response to deflections. The sensor is encapsulated within a thin biocompatible polymer shell of poydimethylsiloxane (PDMS) providing device integrity and moisture isolation. The results suggest that such a sensor can potentially function

as both mechanical and biotelemetry sensors for various *in vitro* and *in vivo* biomedical applications.

The following chapters discuss how combining technologies of selected organic polymer materials and fiber electro-spinning apparatus with cell immobilization procedures determines electrospun fiber mat effectiveness. Several examples demonstrate how a solution of electrospun, biocompatible nanofibers composed of polymer(s) can be used to control time rate of degradation and produce a nanofiber scaffold structure supporting attachment and proliferation of cells of interest for *in vitro* application. They show in detail how cells combined with artificial extra-cellular matrix (ECM) of desirable biocompatible and biodegradable characteristics are important to tissue engineering research. Several polymers, both natural and synthetic, including alginate, chitosan, polyethylene oxide (PEO), polycaprolactone (PCL), and piezoelectric polyvinylidene fluoride (PVDF) compositions for electrospinning are presented. Piezoelectric nanofibers that could offer many useful applications were electrospun. Solutions having different composition ratios producing random and semi-aligned nanofibers through standard electrospinning collector electrode techniques are discussed, as is a newly developed aligned fiber electrospinner that uses centrifugal force with pneumatic assistance to produce a highly viscous solution rendering the fibers electrospinable. A novel biotelemetry sensor owes its embryonic beginnings to highly aligned nanofibers created through centrifugal electrospinning. Through these techniques, simple, highly aligned piezoelectric polyvinylidene fluoride and tetrafluoralethane nanofibers can be fabricated to function as a standalone power source, sensor, and transmitter.

TABLE OF CONTENTS

		Page
List of Figures		iv
Table of Tables		xi
Acknowledgments		xii
CHAPTER 1: Introduction		1
CHAPTER 2: Background in Electrospinning		7
2.1	Electrospinning Tissue Engineering Nanofibers	12
2.2	Techniques of Electrospinning	13
2.3	Significant Variables Affecting Electrospinning	16
2.4	Processing Variables	17
2.5	Fiber Alignment and Collector Types	20
CHAPTER 3: Fabricating of Organic Polymer Scaffolds		22
3.1	Fiber Background Work in Electrospinning (Alginate and Chitosan)	22
3.2	Procedure Producing Alginate Fibers	25
3.3	Procedure Producing Chitosan Fibers	30
3.4	Aligning Fibers	36
CHAPTER 4: Cell Culture Procedure and Nanofiber Adhesion Approach		40
4.1	Cell Viability and Morphology Determination on Chitosan Nanofiber	41
4.2	Integrity of Nanofibrous Structure in Water	42
4.3	Cell Adhesion, Spreading, and Viability	43
CHAPTER 5: Polymer Nerve Guide Example Using Electrospun Nanofibers		46
5.1	Nanofiber Synthesis Procedures	46
5.1.1	Synthesis of chitosan-PCL nanofibers by electrospinning	47
5.2	Synthesis of Chitosan-PCL Cast Conduits	48
5.3	Microscopic Imaging of Nanofibrous Structures	48
5.4	Degradation of Nanofibrous Matrix	49
5.5	Nanofibrous Matrix Characterization	49

5.6 Cell Transfection 50
5.7 Cell Culture, Attachment, and Proliferation 50
5.8 Immunocytochemistry 51
5.9 Mechanical Testing 52
5.10 Statistical Analysis 52
5.11 Electrospun Chitosan-PCL 53
5.12 Physical Properties 53
5.13 Mechanical Strength 54
5.14 Nerve Conduit Pilot Study 59
5.15 Mechanical Strength 64
5.16 Nerve Conduit Pilot Study 67

CHAPTER 6: Introduction to CES and Alignment of Fibers 70
6.1 Centrifugal Electrospinning for the Production of Highly Aligned Long Nano- and Micron-Scale Fibers (4th example of ES Polymers) 71
6.2 New CES Electrospinner 74
6.3 Electrostatic Field Analysis Using ANSOFT® 75
6.4 Centrifugal Force Effects on Fiber 81
6.5 Experimental Setup 84
6.5.1. Spinneret Rotating Speed 85
6.5.2. Applied Voltage 85
6.5.3. Taylor cone 85
6.5.4. Polymer-feed rate 86
6.5.5. Spinneret-ground distance 86
6.5.6. Gap distance 86
6.6 Effect of Polymer Concentration 87
6.7 Production of Synthetic and Natural Polymer Fibers 94
6.8 Example of Significant Role Electrospinning has in Tissue Engineering 95
6.9 Characterization of CES Apparatus 97
6.9.1. Parameter optimization 97
6.9.2. Fabrication of chitosan 98
6.9.3 Viscosity measurements 99
6.9.4 Fiber characterization 99
6.10. Piezoelectric Characterization of Aligned Polyvinylidene Fluouride (PVDF) Nanofibers 100

CHAPTER 7: Nano-Fiber Mechanical Characterization 103
7.1 Nanotensile Tester to Characterize Fiber 104
7.2 Differential Load Transducer Design (DVRT) 108
7.3 Mechanical Force Transducer Parameters 112
7.3.1 The load transducer 113
7.4 Load Transducer Characterization 115
7.5 Measurement of Single Nanofibers 118
7.6 Fiber Orientation Strength Comparison 119

CHAPTER 8: Uni-axially Aligned PVDF Nanofibers as Sensor and Transmitter for Biotelemetry 122
8.1 PVDF Nanofibers Fabrication 124
8.2 Encasing of PVDF Nanofibrous Bundle in PDMS 124
8.3 Voltage-Current Signal Measurements 125
8.4 Biotelemetry Setup 126
8.5 Data Collection System 128
8.6 Voltage Signals at a Particular Loading and Distance 130
8.7 Voltage Signal at Different Loadings 132
8.8 Voltage Signal at Different Distances Between Transmitter and Receiver 134

CHAPTER 9: Conclusion 135

APPENDIX 1 137

REFERENCES 141

PUBLICATIONS 159

LIST OF FIGURES

Figure **Page**

Figure 1. Taylor droplet voltage-geometry history when high voltage applied [31]…… 8

Figure 2. Nanofiber applications…… 10

Figure 3. Basic Electrospinner with spinneret and collector separated by predetermined distance “d” allowing time for solvent evaporation to occur before fiber touches down on collector…… 15

Figure 4. SEM images of alginate-PEO nanofibers: (A), (B) and (C) are survey images of the nanofibers spun from solutions with alginate/PEO ratios of 70/30, 80/20, and 90/10, respectively. (A'), (B') and (C') are corresponding high magnification images of (A), (B) and (C). The insets are the fiber size distributions. All polymer solutions were prepared with addition of 0.5 wt% Triton X-100™ surfactant and 5 wt% DMSO cosolvent…… 28

Figure 5. (A) and (B) are XRD patterns and mechanical tensile modulus of alginate-based nanofibers, respectively. (C) and (D) are the SEM images of nanofibers after immersion in DI water for 1 and 15 days, respectively. The ratio of alginate/PEO is 80/20…… 29

Figure 6. Polymer solution shear viscosity as a function of shear rate, prepared from 0.5M acetic acid solution with different polymer concentrations and chitosan to PEO ratios (A) 2%, chitosan/PEO = 100/0; (B) 2.05%, chitosan/PEO = 90/10; (C) 2.1%, chitosan/PEO = 80/20; and (D) 2.2%, chitosan/PEO = 60/40…… 32

Figure 7. SEM images of the products electrospun from solutions of different chtiosan/PEO weight ratios and polymer concentrations: (A) 100/0 and 2%; (B) 90/10 and 2.05%; (C) 80/20 and 2.1%; and (D) 60/40 and 2.2%. The corresponding viscosity of these solutions is shown in Figure 4…… 33

Figures 8A – 8E. SEM images of electrospun structures (chitosan/PEO ratio = 90/10) prepared from 0.5M acetic acid solutions containing: (A) 0.3 % Triton X-100™, (B) and (C) 0.3% Triton X-100™ and 10% DMSO. Fibers in image B (average fiber diameter = 43 ± 8 nm) were collected on a stationary collector whereas fibers in image C (average fiber diameter = 65 ± 11 nm) were collected on a cylindrical collector with a rotating speed of 2000 rpm. Images D and E are the high-magnification images of B and C, respectively. The average diameter of electrospun nano-fibers was determined by measuring the diameters of the nanofibers in 100 different points of a 645 × 484 SEM image using Microsoft photo shop program (Photoshop 7.0). Fiber size distribution of the electrospun fibers of the images C and D of Figure 2…… 36

Page

Figure 9. (A) A fiber bundle collected on the surface of a thin copper wire mounted on a rotating drum; (B) high-resolution SEM image of aligned nanofibers in the bundle. The chitosan/PEO ratio was 90/10 with 0.3% surfactant and 10% DMSO…… 38

Figure 10. Evaluation of cellular compatibility of alginate based nanofibers (alginate/PEO is 80/20) *in vitro*. SEM images of chondrocytes grown on alginate nanofibers: (A) survey image, (B) high magnification image, and (C) fluorescence image of cells on nanofibers with the live/dead cell stain…… 40

Figure 11. SEM images of the chitosan/PEO fibers with ratio of 90/10 and 50/50 showing the morphology of fiber structure after immersing in water (pH 7.5 at room temperature) in different time. All conditions for the fiber preparations were same as in Figure 3 (C)….. 44

Figure 12. Live (stained green) and dead (stained red) staining of the chondrocytes cultured for 1 day; (A) nanofibrous membrane of chitosan/PEO (90/10), and (B) solvent cast film of the same chitosan/PEO (90/10)…….. 44

Figure 13. SEM micrographs of osteoblasts (MG-63) (A and B) and chondrocytes (HTB-94) (C and D) seeded on nanofibrous membrane of chitosan/PEO (90/10) after 5 days and 3 days culture, respectively; (A) 800 × original magnification, (B) 3500× original magnification, (C) 800 × original magnification and (D) 2500 × original magnification. Magnified images show the attachment of both cell types with two fibrous structure of the electrospun membrane……..45

Figure 14. SEM micrographs of chitosan-PCL nanofibers prepared with different ratios of chitosan to PCL, showing the spinability of the solution in a wide range of chitosan-to-PCL ratios to produce bead-free nanofibers…… 56

Figure 15. Structural properties and chemical stability of chitosan-PCL nanofibrous matrices. (a) SEM image of as-synthesized chitosan-PCL nanofibers (chitosan: PCL = 40:60) showing bead free fiber morphology. (b) TEM micrograph of chitosan-PCL nanofibers showing no visible phase segregation or porosity. (c) WAXD patterns of blend nanofibers with varying component ratios of chitosan to PCL; the blend with a ratio of 40/60 or above showed significantly reduced crystallinity signifying increased miscibility. (d) SEM (upper row) and TEM (bottom row) images of bulk nanofiber materials after incubation with lysozyme-PBS solution for various durations revealing no apparent morphological change, phase segregation, or decomposition of the fiber constructs, demonstrating structural and chemical stability……. 57

Page

Figure 16. Spinability of chitosan-PCL solution over storage time. (a) Shear viscosity of chitosan-PCL solution (chitosan: PCL = 40:60) as a function of solution storage time at room temperature, showing that the solution viscosity decreases over time after solution preparation and there is a time window beyond which no fibrous structure can be obtained. (b) SEM images of chitosan-PCL nanofibers prepared with chitosan-PCL solutions at different storage times, showing that the viscosity and thus, the storage time of the solution directly influence the spinability, and only solutions with short storage times yielded bead-free structures. Fiber morphology obtained from the solution with a storage time less than 5 min was marked as 0 hr……..... 58

Figure 17. (a) DSC thermograms of blend nanofibers (chitosan: PCL = 40:60) acquired before nanofibers were incubated in a lysozyme-PBS mixture and at different time points after the incubation. A physical mixture of chitosan and PCL at the same ratio was shown as a reference. (b) FTIR spectra of as-synthesized chitosan-PCL nanofibers and the nanofibers incubated PBS/lysozme solutions for different times……. 60

Figure 18. Adherence and proliferation of Schwann and PC12 cells on various materials. (a) SEM images of Schwann cells (top row) grown on various materials for 1 day and PC12 (bottom row) on various materials for 7 days. (b) Confocal images of PC12 cells on PCL nanofibers, chitosan-PCL nanofibers, and chitosan-PCL films, stained with an NGF receptor (green) antibody and DAPI (blue). (c) The numbers of Schwann cells (top) and PC12 cells (bottom) on various materials as a function of culture time, assessed by the alamar Blue assay. Values are means of three independent experiments; error bars correspond to standard error of mean……. 62

Figure 19. Mechanical properties and cellular compatibility of chitosan-PCL nanofibrous conduits. Tensile (a) and compressive (b) test results for tubular constructs at both dry and wet states for various nanofibrous conduits where PLGA and collagen nanofibrous conduits served for comparison. The solvent casting chitosan-PCL conduit in b was used to counter illustrate the superior mechanical properties of the nanofibrous structure. *Compressive testing of the solvent cast tube at 50% compression resulted in premature sample fracture. (c) Confocal microscopic images of Schwann cells (green) and PC12 cells (red) co-cultured on chitosan-PCL nanofibrous conduits, showing adherence of GFP-transfected Schwann (indicated by white arrows) and PC12 cells on the inner and outer surfaces of the conduit. (d) SEM micrographs of Schwann and PC12 co-cultured surface of the conduit at lower (top) and higher (bottom) magnifications showing neurite-like outgrowth of PC12 cells…… 65

Figure 20. SEM micrographs of Schwann and PC12 cells co-cultured on chitosan-PCL nanofibers for 7 days at lower (left) and higher (right) magnifications…… 67

Page

Figure 21. *In vivo* study of chitosan-PCL nanofibrous conduits for nerve regeneration in a rat sciatic defect model……. 68

Figure 22. Centrifugal electrospinning setup; (a) schematic of the setup, (b) photograph of the setup, polyethylene oxide (PEO) fibers electrospun between grounded platens and (d) photograph of the syringe-spinneret……. 76

Figure 23. (a) Schematic illustration of centrifugal electrospinning setup; (b) electrical field distribution with large gap; (c) and electric field distribution……. 77

Figure 24. Triangular mesh automatically generated by Ansoft®…… 78

Figure 25. Electric vector distribution using 20kv source. Images illustrate field distribution between high-voltage source and grounded collector electrodes allowing aligned fiber accumulation in gap…… 78

Figure 26. Electric-magnitude distribution of figure-6 with 20kv source…… 79

Figure-27. Voltage distribution with 20kv source…….. 79

Figure 28. Illustration of the (a) centrifugal electrospinning (CE) setup; (b) electric field distribution; (c) repulsive charge forces; (d) centrifugal and Coriolis effect…… 82

Figure 29. PVDF-TeFE electrospun between a 4 cm gap with a (a) stationary or (b) rotating (150 rpm) spinneret. Insets are FFT analysis of the fiber alignment…… 84

Figure 30. SEM images of fibers produced from (a) 20, (b) 22.5, (c) 25 and (d) 27.5 wt% PVDF in DMF/acetone. The scale bars represent 2 μm. The PVDF solutions were electrospun at 12 kV and 200 rpm and the fibers were removed from between a one-inch collector-collector gap. The fiber diameter distribution (e) was plotted with the median diameter represented by the interior horizontal line. The upper and lower horizontals designate the upper and lower quartiles. The error bars indicate the largest and smallest fiber diameter measured within a dataset of 50 fibers…….. 88

Figure 31a. Highly aligned PVDF fibers using the CE setup with a 20 wt% solution at 15kV and 225 rpm……. 89

Figure 31b. PVDF nanofibers and FFT analysis of the fiber alignment. PVDF fibers were fabricated using 70wt% PVDF plus 30wt% TeFE added to five times 60wt% DMF and 40wt% Acetone. Second composition was 70wt% PVDF-30wt% TeFE with 60wt% DMAC and 40wt% Acetone. Both cases were electrospun at 12KVdc and 425 rpm…… 90

Page

Figure 31c. Aligned (a) PEO and (b) chitosan-based fibers prepared on the CES. The scale bars represent 2 μm. PEO fibers were produced using 22KVdc, 300 rpm, and a 20-cm spinneret-electrode distance. Chitosan-based fibers were produced from using 22KVdc, 300 rpm, and a 20-cm spinneret-electrode distance……. 91

Figure 32. (a) (b) CES electrospinner developed in Zhang lab. (c) Thin mat consisting of aligned PVDF nanofibers produced with a 25 wt% solution, 20-cm spinneret to ground distance, 20 kVdc and 13-cm plate separation…….. 92

Figure 33. PVDF fibers produced at various spinneret rotational speeds. (a) SEM images of deposited PVDF nanofibers (scale bars = 20 μm). (b) FFT analysis illustrating the degree of alignment. (c) Arbitrary pixel intensity plotted from the radial summation of pixel intensity from the FFT analysis. (d) Fiber diameter distribution with the median diameter represented by the horizontal line shown in the middle of the bar. The error bars indicate the largest and smallest fiber diameters measured from a dataset of 50 fibers…… 93

Figure 34. PVDF fiber morphology as a function of the electrode gap width. SEM images of the PVDF nanofibers deposited on (a) 1-inch, (b) f=4-inch, and (c) 6-inch electrode gaps. The scale bars represent 2 μm. Insets in (a), (b), and (c) are the FFT analysis illustrating the degree of alignment. (d) Arbitrary pixel intensity plotted from the radial summation of pixel intensity from the FFT analysis…… 94

Figure 35. Schwann cells on chitosan-PCL cast film, random and aligned chitosan-PCL nanofiber mats after three days of cell culture. The scale bar represents 10 μm……. 96

Figure 36. CES electrospun technique with pressure assistance……. 98

Figure 37. Piezoelectric characterization of PVDF fibers. (a) Schematic of the setup employed to test the piezoelectric behavior of aligned and randomly-oriented PVDF-Tetra-FE and TBAC fibers. Fiber specimens were cast in PDMS, connected to electrodes, fixed via a clamp at one end and deflected at the opposite cantilever end. The resulting (b) piezoelectric voltage output was measured (n=3)…… 100

Figure 38. Piezoelectric characterization of PVDF nanofibers for states of centrifugally generated aligned fibers (Figure 33a), and statically collected aligned and random generated nanofibers…….. 101

Figure 39. Nano-tensile tester tension stretching 53 nanofibers…… 104

Figure 40. Overall schematic diagram of the device: P, differential fixture; Q, stepper motor; R, DVRT; S, noise canceling signal conditioner; T, stepper motor controller; U, DAQ; V, extra voltage display (generated from R); and W, computer…… 106

Page

Figure 41. (a) 39nm resolution tensile tester with ability to support 20nN, 0.015N, or 1.0N load transducer heads; (b) specimen holder having edges of window snipped once specimen-tape ends are secured to grippers; (c) diagram illustrates differential action frames with opposing springs; specimen is between upper and lower grippers, see Appendix-1. “A” – tensile/compression range of 100nm, +/- 30g / 1kg, and in configuration “B” using a DVRT– tensile range 10nm /20nN……. 107

Figure 42. Transducer types used on Zhang lab nano tensile tester. (a) a 10N, (b) a 30 gm, (c) a DVRT (differential voltage reluctance transformer). “A” – tensile/compression range of 100nm, +/- 30g / 1kg, and in configuration “B” using a DVRT– tensile range 10nm / 20nN…… 108

Figure 43a. Simplified form of differential fixture…… 109

Figure 43b. With specimen present on Frame “B”…… 109

Figure 44. Labview output display for nano-tensile tester. Curve illustrates tension andcompression for an up and down motion applied to load transducer…… 116

Figure 45. (a) Two separate tensile tests are conducted, one with specimen and one without, see Figures 1 and 2, (b) result from subtracting the two tensile tests arriving at specimens contribution……. 117

Figure 46. Alginate stress-strain curve for dry and wet specimens……. 117

Figure 47. SEM image of electrospun PEO nanofibers used for tensile test. Scale bar is 1-*μ*m……. 119

Figure 48. PVDF aligned fiber…… 120

Figure 49. PVDF random fiber…… 120

Figure 50. PVDF film……. 121

Figure 51. Aligned PVDF fiber bundle used to construct the coil (biotelemeter). (a) Photographic image of an aligned PVDF nanofiber bundle (scale: 3 mm). (b) SEM image of PVDF nanofirers in the bundle (scale: 1μm)……. 127

Figure 52. Schematic diagram of the test system for biotelemetry device. (a) Top view of the coil of PVDF nanofiber bundle. (b) Remote receiver antenna that receives the signal from the coil. (c) Experimental layout, where the aluminum beam (cantilever) brings the loading to the coil and foil strain gauge……. 127

Page

Figure 53. Schematic diagram of the testing system for the biotelemetry device showing connections of the PVDF nanofiber coil, receiving antenna, foil strain gauge, 440μF capacitor, and a computer equipped with a DAQ for data acquisition and analysis. The foil strain gauge is connected to the computer through an NI9219 signal conditioner. In addition to the wireless connection between the coil and receiving antenna, a direct wire connection is also established between the coil and the computer through a NI 9219 signal conditioner as a reference. The receiver antenna is connected to computer through a 34420A Agilant nanovolt meter. The aluminum beam is fixed on one end (base clamp) and is free on another end for bending. Photographic images show the PVDF coil affixed to the top surface of the aluminum beam (upper left corner, scale: 4 mm) and the foil strain gauge affixed to the bottom surface of the aluminum beam (upper right corner, scale bar: (2 mm)……..... 129

Figure 54. Voltage signal vs. time during periodic deflection of the free end of the cantilever beam by 0.5 mm. From top to bottom, are the signals received from the foil strain gauge via hard wire to strain gage signal conditioner displaying peak voltage per time of beam deflection to beam release giving sawtooth profile, PVDF spiral coil via wire connection, and copper wire antenna coil via wireless communication with both displaying flatten top due to a large capacitive load, 440μF, in order to extend the very low-frequency limit of our measurement set-up……. 131

Figure 55. Voltage signal vs. time for periodic beam deflections by 1 mm (left column) and 1.5 mm (right column). From top to bottom, are the signals received from the foil strain gauge via hard wire to strain gage signal conditioner displaying peak voltage per time of beam deflection to beam release giving sawtooth profile, PVDF spiral coil by wire connection, and copper wire antenna coil by wireless communication with both displaying flatten top due to a large capacitive load, 440μF, in order to extend the very low-frequency limit of our measurement set-up……. 133

Figure 56. The power output in watts for the three different deflections of 0.5mm, 1mm, and 1.5mm locations. …….. 133

Figure 57. Voltage signal vs. distance between the nanofiber sensor coil and receiving antenna verses Aluminum cantilever beam deflection of 0.5 mm……. 134

Figure 58a,b. Titanium Nano-tensile tester specimen clamp. The device is spring loaded and also having a tightening screw to finger tighten specimen. 1000 grit sand paper is super glued to clamping surface providing positive grabbing surface without crushing the fiber specimen. Spring loaded behind the hinge and also having a tightening screw to finger tighten specimen. 1000 grit sand paper is super glued to clamping surface providing positive grabbing surface without crushing the fiber specimen…… 137

Figure 59. Photograph of the experimental set up (in part) showing the PVDF nanofiber coil encased in PDMS, cantilever beam and tensile/compression tester……. 138

Page

Figure 60. Photograph of the experimental apparatus (in part) showing the foil strain gauge affixed to the bottom surface of the cantilever beam and used as a control strain sensor……. 139

Figure 61. Strain gauge voltage verses cantilever beam deflections of 0.5mm, 1.0mm, and 1.5mm……. 139

Figure 62. PVDF spiral coil voltage verses cantilever beam deflections of 0.5mm, 1.0mm, and 1.5mm…… 140

Figure 63. Voltages received by antenna verses cantilever beam deflections of 0.5mm, 1.0mm, and 1.5mm…… 140

LIST OF TABLES

Page

Table 1. Various Parameter Interactions Affecting Electrospinning Fiber 19

Table 2. Pros and Cons for Autograft and Allograft Applications 25

ACKNOWLEDGMENTS

To my advisor, Miqin Zhang, I wish to say that she was the “best” through her support, mentorship, and encouragement. She provided guidance and assistance in varied ways during my completion of this degree, and I thank her for this. Her enthusiasm for research is intoxicating and provided imaginative inspiration throughout the program; thank you again, Professor Zhang. I also would like to thank my committee members: Dr. Richard Ellenbogan, MD; Dr. James Parks, MD; Professor Qifeng Zhang, PhD; and GSR member, Professor Ming Fan, PhD — all of whom have taken personal time out of their schedules to provide support in my degree quest. I tried to pick the most inspiring committee possible and I think I did very well. I really do feel honored by their presence.

I truly am very appreciative to those Zhang lab members who participated and helped contribute to my lab support efforts. I would especially like to thank the following persons: Professor Narayan Bhattarai, now at NC A&T State University, and Dr. Dave Wood, who was always ready to help out and whose discussions and participation were appreciated. I would also like to say thank you to Bichtien Thach and Yen Cone in the Materials Science and Engineering Office for their help over the years in ordering equipment and chemical materials that supported my project and other associated projects in the Zhang lab. I would also like to thank Dr. Gerry Rossillini, MD, and his nurse Lim Lim, both located on campus in Hall Health, for keeping me as healthy as possible over these PhD pursuit years and scheduling me into University of Washington ER or hospital when required.

I would also especially like thank my wife, Julie, who in the beginning was over-whelmingly supportive, and as the years dragged on still supported my goal for both us even though the pursuit of this degree became stressful at home. I can only hope that the future doors these degrees will ajar will help compensate for some of the grief and loss of time for wife and grandchildren, and that it will become advantageously meaningful in making for happier times and lives from here on.

Lastly, I would like to acknowledge the two years of funding received from the Kaiser Foundation and additional funding provided by Professor Miqin Zhang that supported a lot of the work presented in this thesis.

CHAPTER 1: Introduction

Development of polymeric nanofibers, particularly composite structures that mimic the structure and function of the natural extracellular matrix (ECM), are of great interest in tissue engineering. Scaffolding materials to restore, maintain, or improve the function of human tissues are generating enormous scientific and technological interest because of the wide-ranging applications in biomedicine and biotechnology. The natural ECMs in the body are mainly composed of two classes of extracellular macromolecules: proteoglycans and fibrous proteins with fiber diameters ranging from 50 to 150 nanometers, depending on tissue type. Studies showed that the material size can substantially influence the morphology and function of cells grown on the ECM, and that cells attach and proliferate well in micro- and nano-structured materials.

A number of manufacturing processes have been explored to fabricate micro or nanoscale fibrous matrices, including drawing, self-assembly, template-directed synthesis, phase separation, and electrospinning. Among these techniques, electro-spinning has been widely accepted as the simplest, least expensive, and quickest means to fabricate ultrafine fibers, and has been employed to fabricate nanofibers from a variety of synthetic or natural polymers. Nanofibers derived from natural and synthetic polymers, capitalizing on favorable biological properties of natural polymer and mechanical strength of the synthetic polymer, represent a major advance in tissue engineering and regenerative medicine. However, the development of well-blended, natural–synthetic composite polymers remains an immense challenge due to the poor miscibility of the component polymers, where natural polymers are generally soluble in aqueous and polar solvents, but most synthetic

polymers are not. Poorly blended polymeric nanofibers exhibit weak mechanical strength and uncontrollable material properties as a result of inhomogeneities.

This thesis presents the development and characterization of a natural–synthetic polymeric nanofiber comprised of well-blended organic polymers. The design combines the technological advances in biocompatible polymers and nanotechnology to produce nanofibrous matrices with significantly improved mechanical and biological properties. Another area of nanofiber authentication is its characterization to determine suitable applications. To address this need, we developed a nano-tensile tester to determine elastic modulus and strength of the nanofibers we worked with. In these materials and devices, individual fibers are the primary constituents, and their mechanical properties are of vital importance to their targeted functions. Several experimental methods including atomic force microscopy (AFM) indentation, three-point bending, lateral and axial fiber vibration measurement, and direct axial tension tests, have been exploited in recent years to characterize the mechanical properties of nanofibers.

In AFM nano-indentation, the cylindrical contour of nanofibers will not quantify the correct contact stress and, therefore, it may offer intangible conditions in determining modulus. Analysis with AFM using three-point loading technique showed that small off-axis angles of inclination formed between the original and depressed location on the fiber and could provide higher axial fiber force than the value measured. Transverse and axial fiber vibration measurement techniques are complex and could lead to misinterpretation of the data, especially in axial vibration if a very tiny amount of load resistance contributed by the fiber is not taken into account. However, for proper mechanical property characterization,

the tensile test is the most relevant among other methods since the major failure mode for nanofibers is tensile deformation as they support axial loads in many applications.

This thesis reports design of a cost-effective tensile tester with resolution at nano-Newton and nanometer scales. Biotelemetry is a telemetric method used to remotely monitor, record, and measure basic physiological functions such as body temperature, blood pressure, muscle activity, bone stresses, breathing, and heart rate of living organisms. Since the development of the transistor and integrated circuit systems, biotelemetry has moved away from electronic tubes, making it possible to design small and low-power biotelemetry devices for implantation in the body. However, current implantable biotelemetry devices still need a separate sensor, power source, and transmitter onboard to function efficiently. The need for an onboard battery is more problematic as the power source miniaturization and prolonged service time remain a formidable challenge. These concerns are particularly critical in cardiac applications such as pacemakers, where battery replacement is inconvenient and potentially life threatening. Moreover, batteries must be carefully sealed because even a minute degree of moisture ingression can cause its failure. We have reported that a centrifugal electrospinning process produced long, aligned piezoelectric polyvinylidene fluoride (PVDF) nanofibers that showed a strong piezoelectric property when a small stress/strain was applied [208]. Unlike other biotelemetry devices, this tiny, dual-component device performs all three major required functions for biotelemetry applications: signal sensing, power source, and signal transmission.

Chapter 1 provides basic historical background on the origins of electrospinning. The process originated in the late 1800s when Load Rayleigh noticed how electric fields affected charged liquid drops. Many researchers over the years reevaluated the process until Sir Geoffrey Taylor discovered what is now recognized as the Taylor cone. The electrically charged Taylor cone is the best explanation to date on how suitable solutions designed for electrospinning can generate fibers. Chapter 2 discusses the background of electrospinning along with some history and techniques, useful applications, managing certain electrospinning processes, the use of nanofiber collectors, and variables affecting electrospinning parameters associated with alignment of nanofibers.

Chapter 3 covers procedures and materials used in fabricating organic polymer nanofiber scaffold from solutions made of either chitosan, alginate, or a combination of, and also other natural polymers such as collagen and gelatin. The importance in electro-spinning of voltages and nanofiber alignment illustrate significant aspects of this technique. Chapter 4 discusses biological application and considers cell adhesion, spreading, and viability in respect to success of organic polymer nanofiber scaffolds. The organic polymer chitosan is effective in cell immobilization and growth. Other points of emphasis are the importance of structural integrity and its significance in supporting cellular applications. Chapter 5 discusses a fairly in-depth procedure and characterization of nanofiber stability along with Schwann cell adaptability to highly aligned, structured organic polymer nanofiber scaffolds. Presented is an example of a polymer nerve guide using electrospun nanofibers of chitosan-PCL (poly(*e*-caprolactone) and how synthesis is done for two cast conduits. Cell

culturing, cell attachment, and cell proliferation are presented along with mechanical property characterizations.

Chapter 6 presents a novel electrospinning design that uses centrifugal force and a central rotating spinneret to distribute organic polymer nanofibers in a controllable method to create highly aligned nanofibers. Solutions of polyvinylidene fluoride (PVDF) and chitosan-PEO solution mixture are used. The nanofiber meshes are analyzed using a fast Fourier transform (FFT) technique showing the effectiveness of the centrifugal electrospinning (CES) system. Further significance of PVDF and its piezoelectric characteristics are explored using a bundle of PVDF nanofibers encased within another polymer, PDMS, which when dry presents a rubbery structure, with an electrode at each end. We demonstrated that fabricating highly aligned piezoelectric nanofibers can produce a useful sensor, which will be addressed in the final chapter.

The electrospinning of nanofibers as demonstrated by CES provided us with significant supplies of highly aligned nanofibers and we needed a device to measure the nanofiber modulus of elasticity. Chapter 7 presents a unique and versatile tensile testing apparatus capable of applying a pulling force on a single nanofiber. A 51-strand bundle of nanofibers was tested and the procedure for accomplishing this is outlined, accompanied by an illustration. The nanofiber clamping mechanism [114] is novel in that it uses differential forces to measure the tensile characteristics of nanofibers or bio-tissue materials to 20 nano-Newtons at extension control to 19 nano-meters. Graphs and tables provide comprehensive explanation of the apparatus. An experiment demonstrating simple calibration technique using fine gold (Au) wire is cited. Lastly, Chapter 8 discusses how

highly aligned PVDF nanofibers can be used to create a novel biocompatible sensor. The sensor develops three functions from one bundle of highly aligned multiple PVDF nanofibers. The bundle of nanofibers are formed into a spiral with a capacitance connected across its two ends forming a standalone electronic device able to produce its own voltage through some external applied force, sense that force through spiral strain, and transmit a signal describing the value of that deflection. Its practically was shown by attaching a spiral sensor to a small aluminum cantilever beam and deflecting the beam to measure a signal generated by the PVDF spiral sensor.

Chapter 2. Background in Electrospinning

The term electrospinning (ES) derives from origins based in electrostatic studies conducted centuries ago in the 1740s, when aerosol spheres were described that could be generated using high electric tension impressed on micro-sized fluid drops. In the 1880s, a sir Lord Rayleigh examined the level of charges essential to overcome surface liquid tension on an electrostatically charged drop [5]. Since the early 1900s, various researchers [6,8] have been re-evaluating the old electrostatic process presently known as electrospinning with the first apparatus that could spray electrically charged drops of liquid. It is in review at the US Patent Office under patent numbers 692631,705691, and 745276. Interestingly, only about 50 patents for electrospinning polymer melts and solutions have been filed over the past 60 years, with a recent filing by the Zhang group at University of Washington [209]. At present, there are no known competing commercial processes using electrospinning [7].

In the 1970s, others [10] developed similar devices producing fibers of diameters less than 1μm [9], but this work was more of a curiosity than application. Even with those early electrical discoveries, the process was not very viable or interesting until nanofibers made by electrospinning were fashioned for filter applications. Soon after the view on electrospinning changed and many other applications soon followed. During the 1990s, with nanotechnology awareness occurring in many technological pursuits, academic researchers and industry began to recognize potential applications for using electro-spinning approaches in nanofiber fabrication. Based on electrostatic field configuration and chemical characteristics of polymer or other base solutions, factors such as molecular

weight, viscosity, surface tension, electrical conductivity, electrostatics, electric field gradient, pH, and polymer concentration would affect the formability and morphology of electrospun fibers [10], and applications began to expand. Electrospinning is an effective fabricating technique that could transform composite polymer–solvent solutions into nano-sized fibers [11] in four basic steps involving: (1) dissolution or melt of fiber-forming polymers (precursor) in a continuous phase; (2) high-voltage source to process (jet initiation–extension); (3) solidification of jet into fibers; and (4) surrendering of electrospun fibers from grounded electrode collector. A substantial advantage in using electrospinning for fiber fabrication is its ability to produce both natural and synthetic fibers in novel, various-shaped nanoscale cross-sections. They present respectable mechanical properties possessing desirable structural characteristics through fiber geometry control, fiber alignment, and fiber layering of sheets that can be structurally tailored through electrospinning. Standard electrospinning process uses high-voltage electrostatic force to distort a pendant droplet (Figure 1) of polymer solution into a fine filament for deposition on an electrically grounded electrode collector.

Figure 1. Taylor droplet voltage-geometry history when high voltage applied resulting in a nanofiber stream in far right plate. [32].

As high voltage is applied to the needle possessing polymer solution, the droplet at blunt needle tip begins to stretch. The droplet becomes cone shape on oozing from the blunt tube capillary needle, as was first described by Sir Geoffrey Ingram Taylor in 1964 [12]. The phenomenon is based on assumptions that the cone surface of solution is an equipotential surface and that it exists in a steady state of equilibrium. When the small volume of electrically conductive solution is exposed to an electric field at the tip of the spinneret needle, it deforms due to viscous surface tension alone. This deformation is further increased by the electric field gradient between spinneret and grounded collector electrode. Increasing the voltage level creates a stronger electric field gradient, which exerts a stronger force on the droplet similar to surface tension, but opposite in direction, and modifies the cone shape, forming convex sides with a rounded tip. With further voltage increase the cone's curve will invert, creating a point expelling an electrically charged fine liquid jet (Figure 1, panel 6), allowing attraction to a grounded electrode collector of opposite charge polarity. Nanofibers have been used in many applications including filtration [13], material fabrication [14-16], tissue engineering scaffold design [17-20], regeneration of blood vessels [21,22], extracellular collagen networks [23], smooth muscle cells [24], neurite tissue [25-26], and construction of bone tissue scaffolds [27] (Figure 2).

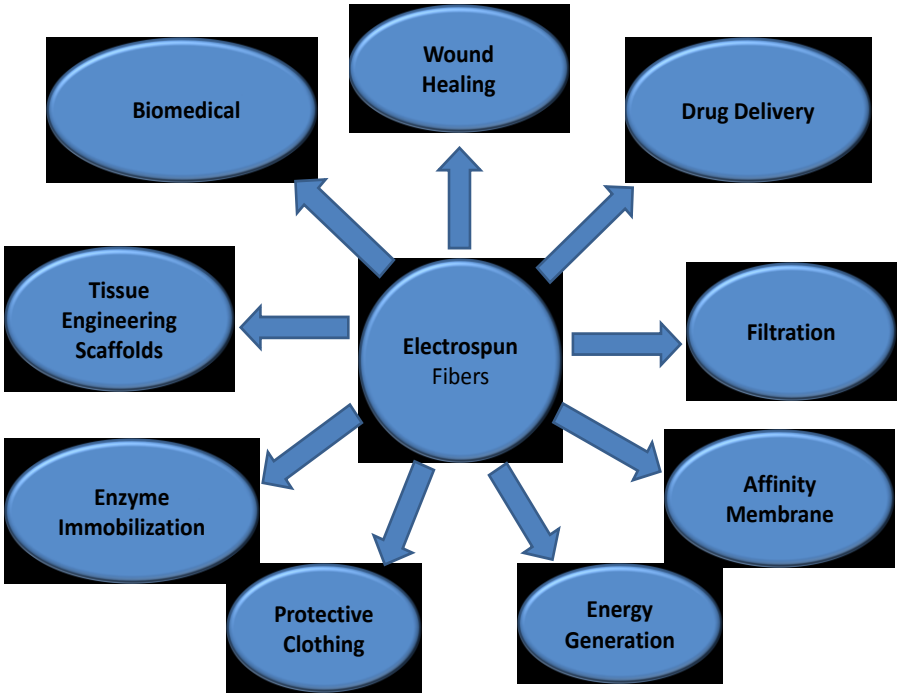

Figure 2. Nanofiber applications.

Other applications include batteries, separation membranes, wound dressing materials, artificial organs, bio-structural elements, scaffolds to organize cells for forming newly regenerated tissues, nano-composites, and protective clothing [28,29,30]. However, to realize these technologies effectively requires an ideal electrospinning system. The engineering challenge is to accommodate various materials or combinations more effectively for new types of chemistry compositions in fiber solution compound formulations. A significant step toward this goal will be presented in Chapter 5.

Materials such as polymers, composites, ceramics, and even metals have been fabricated into nanofibers by using electrospinning directly or through an additional post-spinning process(es). What makes electrospinning so diverse from other nanofiber fabrication processes is the flexibility to form various types of controlled fiber assemblages, such as rod, porous, cavernous, aligned, random, hatched, grid, ribbon, mesh, or 3D structure, from a multitude of materials.

Electrospinning is not the only method for fabricating nanofibers; others are templating, drawing, self-assembly, phase separation, polymer melt, and template synthesis [31-36], but none could match electrospinning in terms of ease of operation, versatility, flexibility and fiber fabrication [37,38,39]. Polymer melt-blown and multi-component processes are capable of matching electrospinning fiber diameter fabricating techniques [40] where it is possible to use thermoplastic polymers to produce nanofiber diameters less than 350 to 450nm [41]. The melt-blown procedure uses a high-pressure extrusion die concept to push hot polymer through multiple orifices or needles into a cooler environment for solidifying fibers, while the multi-component technique mixes different polymers and die-extrudes compound through tiny or concentric orifices to form a thin fiber. Both methods rely on a tiny orifice but can provide substantially increased productivity over that of electrospinner system by yielding just as fine of fibers from a polymer melt requiring significant pressure. Unfortunately, melt processes are limited by material variation, whereas electrospinning is not. Electrospinning also provides greater flexibility in attaining desired fiber diameters while using many different kinds of fiber processing materials, additives, and solvents, without being restricted to thermoplastics.

By and large, natural fibers are favored over synthetic polymers in tissue engineering due to their proven tissue biocompatibility and re-absorbable biodegradation characterization. Synthetic polymers are significantly stronger than organics but exhibit insufficient cell adhesion and create bio-shading [42] due to lack of biodegradation. Their surfaces tend to be hydrophobic, hindering cell attachment and growth within three-dimensional space [43]. When implanted *in vivo*, synthetic polymers can also release acidic degradation products that invoke chronic immune reactions that could be harmful to host tissues [44]. These studies have shown that electrospinning system configuration and operational conditions (environment) differ immensely depending on composition of the material components, i.e., polymer, solvent(s), and other precursors. For instance, solvent vapor pressure and the relative humidity in electrospinner surroundings can have a significant impact on fiber morphology. When energetically weak solvents are used to dissolve polymer involved in an endothermic process, the polymer molecules tend to squeeze solvent out increasing bonding attraction. Using a high-quality solvent allows for higher polymer concentrations and maintains stable solutions separating molecules and preventing gelation [45].

2.1 Electrospinning Basics for Tissue Engineering Nanofibers

Within the human body, natural cells and proteins form symbiotic living tissue interactions wherein what is called extracellular matrix (ECM) supports tissue and cellular genesis and performs this function at the micro-to-nano scale [46]. However, tissue engineering advances scaffolds to form a pre-designed imitation ECM fabricated from non-body originated organic (sometimes inorganic) materials to create fundamentally biocompatible and/or biodegradable scaffold environment supporting cell interaction and proliferation.

Organic materials that are both biocompatible and biodegradable are eligible in presenting natural body tissue development with artificial biodegradable scaffolds functioning as temporary substitutes. Fabricating an artificial scaffolding arrangement imitating ECM to invigorate and encourage cell proliferation requires biocompatible–biodegradable organic material alternatives to replace the body's natural three-dimensional ECM geometry. The scaffolding cavity formed by nanofibers and mat geometry required by cells is unambiguous. Cells explore poorly cavity volumes too large or too small, and surfaces with difficult obstacles also hinder cell proliferation. An effective electrospinning system should be able to provide optimum nanofiber sizes, orientation, pore sizes, and matting to provide cells with the environment required for proliferation.

2.2 Techniques of Electrospinning

Nanofiber scaffolds of membranes, intertwine mats (matrices), tubes, ribbons, and rods have been fabricated for tissue engineering to imitate the body's own ECM micro-to-nano surroundings. Fiber electrospinning is notably used in construction of micro-to-nano size fibrous materials to form a variety of natural, synthetic, and composite blended polymer structures [47,48]. Various nanofiber fabrication methods include drawing, template techniques, phase separation, self-assembly, melt, and electrospinning with the latter demonstrating greater promise and wider use for solution precursor–solvent alteration flexibility, ability to use different materials such as polymer, ceramic, metallic, and solvents, and device ease of use [49].

Successful electrospinning depends on a number of interrelated parameters [50] such as precursor molecular weight, solution viscosity, voltage, solution conductivity, dielectric effect of solution, pH, surface tension of solution, needle diameter, temperature, spinneret to collector distance, and ambient conditions such as pressure, vacuum, and humidity [51]; at low pressure, fibers will not form due to direct discharge of electrical charges. The electrospinning process depends significantly on these variables in general and as listed are mostly associated with the solution's composition properties. For example, a high molecular weight implies high viscosity, which implies larger surface tension requiring a higher voltage to create a Taylor cone resulting in fiber having greater electrical charge that leads to instabilities along fiber length due to unequal charge sites. During electrospinning a polymer–solvent solution is electrified through high-voltage contact, creating an elongated polymer fiber-jet when expelled through a needle toward a grounded collecting electrode. Standard electrospinning systems, i.e., static or dynamic collector electrodes, place a polymer–solvent solution within an insulated syringe-needle apparatus and attach a high-voltage wire from either a DC or AC high-voltage power source to the metallic needle [52]. When voltage is applied and slowly increased, a polymer droplet begins to form at needle tip, and increasing voltage further produces a cone-shaped drop called a Taylor cone [53], from which a micro-to-nano fiber emanates (Figure 3). This cone formed due to the increased voltage overcomes the viscosity of the surface tension of the polymer–solvent. The resulting charged fluid-like fiber-jet remains charged along its length [54] while moving through electric field gradient established between high-voltage needle tip and grounded collector. The charge on fiber is not uniform as intensity of electric

charges varies along the length and causes fiber-bending instability and fiber stretching, which occur due to electric charge repulsion along the length of the fibers [55,56].

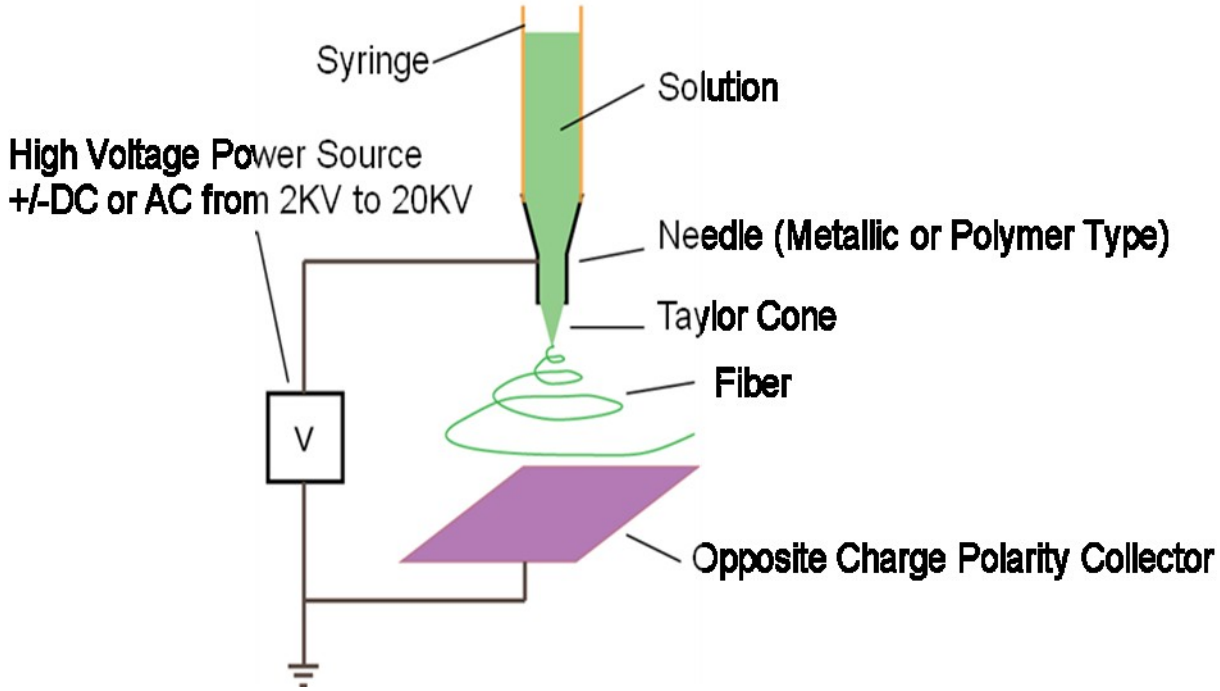

Figure 3. Basic electrospinner with spinneret and collector separated by pre-determined distance allows time for any particular solvent evaporation to occur before fiber touches down on collector.

With electrospinning, fiber strands or mats present high surface area to volume ratio and provide the ability, to a degree, to control pore size, and thus gaps in porous surface and spaces between fibers. The large surface area to volume ratio of nanofibers, πdl versus $\pi r^2 l$, is roughly three orders of magnitude greater than for a similar ratio of a human hair. At a fiber diameter of 3nm the surface area and volume of a nanofiber are not equal; $\pi dl \neq \pi r^2 l$. In fiber technology the unit of a denier (1 denier = 1gm/9000m; <1d => μ-fiber) [57] is for measuring fiber and specifies the mass of a fiber with a length of 9000m, and is often used as a measure of fiber fineness. Given a fiber of 10μm in diameter, the fineness is 1

denier, and for a fiber of 100nm in diameter, its fineness is 10^{-4} denier. The following example further illustrates significance of surface area over volume and is based on the "denier" equation, fiber diameter (cm) = $\{(4.444E\text{-}6[\text{denier}])/(\pi\ \rho_{gm/cc})\}^{1/2}$ where ρ is solution density. If a fiber has a 1-μm diameter and is fabricated from 0.1g of polyethylene oxide (PEO), it will be 1km in length. Now compare this to a fiber diameter of 10nm and same 0.1g and a length of 13,000km. So for that same 1-μm fiber, the specific surface area of the fiber will be 0.04m^2/gm, while the 10-nm fiber surface area is 4.0m^2/gm indicative of the advantage of nanofiber surface area sites allowing for different surface and core geometry and chemical reactions to occur on.

2.3 Significant Variables Affecting Electrospinning

Solution variables previously mentioned affect the electrospinning process in different ways; for instance, humidity above 76% [58] causes pores to form on and in nanofibers. Polymer viscosity and concentration [59] affect the voltage required to overcome surface tension, which affects fiber diameter and bending stability [60]. Electrospinning solution viscosity and solubility of polymer in a particular solvent is strongly related to polymer concentration and molecular weight [61], which influences fiber diameter and morphology [62]. For the electrospinning process, it is necessary to have sufficient polymer chain entanglement to produce a uniform fluid jet. If the concentration is too low, continuous fibers cannot be formed and polymer beads or beads-on-a-string result, but with higher conductivity beads disappear [63]. For cases in which the concentration and subsequent viscosity are too high, the solvent dries too quickly at the syringe tip, leading to non-continuous fibers and clogging of the polymer feed rate [64,51]. A high fiber-jet surface

tension results in bending instability [65] and formation of droplets or beads as opposed to continuous uniform fibers. However, the surface tension of most electro-spinning solutions is negligible when the viscoelastic properties of the solutions become the dominant force [66]. The conductivity of the solution is dictated by the conductivity of the polymer [67], solvent conductivity, and any additives that create ions. In general, an increase in electrical conductivity will decrease the fiber diameter when confronted with a high electric field, causing increased fiber jet instabilities, which thins the jet [68]. Low conductivities promote insufficient elongation of the fiber-jet, and beads may be produced [69].

2.4 Nanofiber Processing Variables using Electrospinning

Electrospinning nanofiber processing requires many variable interactions (Table 1) that affect the electrospinning process, including, but not limited to, atmospheric conditions such as humidity and pressure (high–low), applied voltage, polymer solution feed rate, spinneret needle tip to grounded collector electrode distance [70], and ground collector electrode configuration. For particular voltage levels, a given flow rate is required to maintain a Taylor cone [37,60]; if the flow rate of polymer solution is excessive, beads could form or fiber diameter could increase and result in insufficient drying. If a lower flow rate is used, then thinner fibers are generally achieved. The tip to collector distance is also important to ensure the formation of uniform, non-porous fibers in which a minimum distance is required to allow sufficient drying time for the fiber's travel to the grounded collector electrode.

Voltage is an indispensable variable in the electrospinning process [71], but other techniques can generate nanofibers by using only centrifugal force to push polymer from

spinneret needle [72]. A minimum voltage is essential to overcome surface tension and provide drop volume to encourage a Taylor cone pattern from a polymer droplet, from which a continuous fluid jet is ejected. As electrical tension increases, cone will begin to form at about a 30-degree angle [73]. The electrical charge originates on the drop surface rather than the smaller tip of the Taylor cone; as voltage increases a thin fiber forms at the now pointed end of the drop and is attracted to the grounded collector. Several things can occur at increased voltage; for example, beads of polymer can appear due to instability of fiber-jet as Taylor cone oscillates back-and-fort inside needle [69], but at even higher voltage levels beads can join, forming a thicker fiber diameter [74]. At high voltages solvent evaporation occurs faster than removal of the solvent from needle tip [51], causing internal needle clogging. At high voltages and reduced solution viscosity, secondary jets may form by overcoming solution viscosity and have the effect of reducing fiber diameter [75].

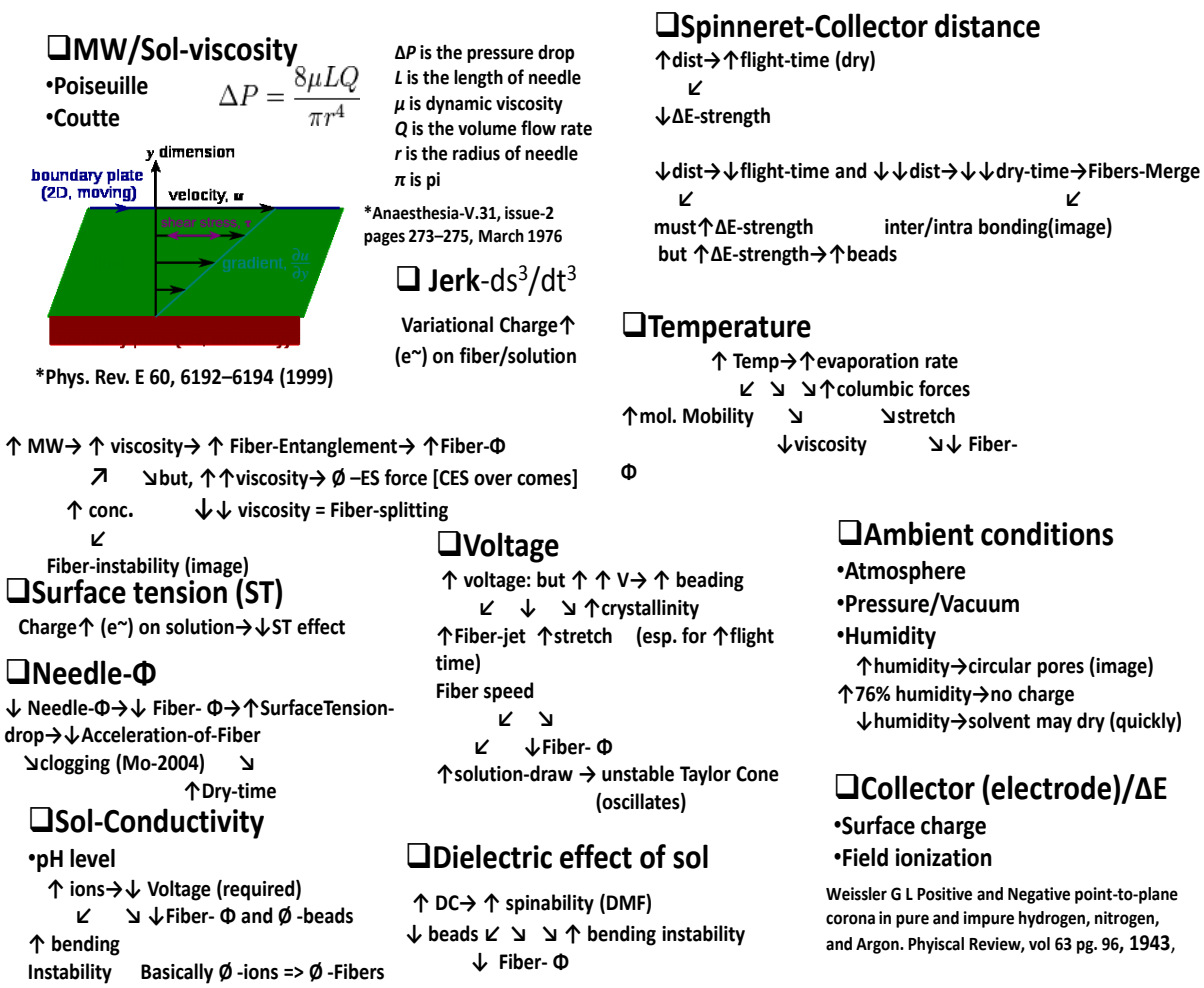

↑ = increases (↑↑ = much more); ↓= decreases (↓↓much less); ↗↖↘↙→ = implies; Φ = diameter; ΔE = electric field gradient; Ø = no, none.

Table 1. Various interaction parameters that affect electrospinning of nanofiber.

Obtaining useable fiber requires that, during fiber's flight to grounded collector electrode, solvent must be completely evaporated on arrival at grounded collector electrode to prevent inter- or intra-layer fiber blending [76]. It can be avoided if proper distances between spinneret–collector are maintained; too large a distance can increase fiber

diameter, in some instances due to electrostatic reduction allowing fiber to contract [77]. If separation distance is too great, no fibers will form [78]. The solvent type used also affects solution evaporation and depends on the solvent's vapor pressure, boiling point, specific heat, rate of heat supply, enthalpy, interaction of solvent(s) and solute molecules, surface tension, and air circulation above solution. The ambient atmospheric conditions, such as temperature and humidity, have opposite effects and can affect the evaporation rate of the solvent in the polymer system. For example, high atmospheric temperature can lead to lower solution viscosities and faster solvent evaporation followed by smaller fiber diameters due to Columbic stretching of fiber [79]. Increased humidity can result in charge dampening and opposite effect occurring with humidity reduction; water vapor present with humidity presents condensation causing pore formation on fibers, while decreased humidity can evaporate volatile solutions rapidly and cause needle clogging [59,80,81,82].

2.5 Fiber Alignment and Collector Types

A considerable number of collector configurations have been experimented with in attempts to fabricate totally aligned fibers. Conventional electrospinning systems consist of either a static or a rotating cylindrical collecting electrode gathering randomly oriented fiber mats. Other grounded collector designs incorporate wire meshing, wire rods, wire grid cylinder, parallel wire cylinder, stacked circular rings, liquid filled pans, and rotating disks to mention a few [48]. A few of these designs can fabricate a small area of aligned fiber but not sufficient for tissue engineering needs. Most designs fail to provide for applications requiring highly structured and aligned fiber assemblies that promote physical, mechanical, and chemical requisites for *in vivo* tissue engineering applications.

Another benefit of the electrospinning process is that the structure, porosity, and orientation of fibers can easily be controlled by simply modifying the grounded collector and/or spinneret configuration, polymer composition, and environment. Some static grounded collector electrode designs incorporate a two-piece parallel collector or a rectangular slot cut into collector, with either approach establishing an air gap between two edges. Within this gap an anisotropic electric field gradient is established that tends to align the fibers parallel to field lines perpendicularly to electrode edges. In an unmodified field, the electrostatic field gradient extends radially from the charged syringe tip toward the grounded collector. Introducing an air gap between two grounded collector electrodes, allows the electric field vectors to bend toward each grounded collector's facing electrode edge from the gap center. As a result, when charged fibers approach grounded collector the fibers align co-linear to the electric field vectors in gap and perpendicular to parallel electrode edges. This arrangement is heavily dependent on gap spacing between grounded collector electrodes. Aligned fibers created by this method have presented one of the better methods adding to fiber quality, i.e. increased fiber crystallinity, improved mechanical strength, better pore size control, and aligned mats created. More will be discussed on aligned nanofibers in chapter-6.

CHAPTER 3: Fabricating Organic Polymer Scaffolds

The following sections describe the procedures of electrospinning nanofiber for the purpose of cell deposition. Alginate was used for the very first time by us by creating nanofibers from it to use its desirable biocompatibility with cells. The fabrication and use of nanofiber chitosan is also presented from nanofiber fabrication to cell applications.

3.1 Fiber Background Work in Electrospinning and Purpose

Electrospinning processes manufacture nano-sized fibers from various types of biocompatible synthetic materials, but in some cases synthetic polymers present biological problems. For instance, use of absorbable orthopedic implants made of poly-L-lactide (PLLA) [84] has increased substantially during the last decade, and although PLLA is an electrospinable biocompatible material, it does not promote tissue growth well. At present, most of orthopedic implants are fabricated from PLLA or its co-polymers, or mixtures containing other constituents. *In vivo*, PLLA persists for years after its surgical role has ended, which is confirmed by a long-term histological study [84] of PLLA implanted in sheep either as functional interference screws or nonfunctional rods. The first tissue reaction is the sequestration of the implant within new bone during the initial three months. After a nonreactive period, a second tissue reaction is associated with early signs of structural disintegration of the PLLA at around one year. Subsequently, as the polymer mass reduces, it is replaced by a relatively avascular fibrous tissue containing macrophage cells arising from monocytics and having an occasional multinucleated giant cell on the implant surface. After three years much of the polymer is still present, although as isolated

fragments. The tissue reactions can be explained in terms of the physical chemistry of PLLA degradation. The excessive longevity of PLLA and the absence of its replacement by bone, indicates that despite being satisfactory clinically, it is not an ideal implant material, and that improved absorbable materials need to be developed.

While standard electrospinning techniques [83] have proven to be a useful and generally accepted means for fabricating polymer micro- and nano-fibers, its applicability to a new material system is not straightforward. Other different electrospinning techniques and materials could assist even as presently used electrospinning systems are providing polymeric nanofibers applicable to a broad spectrum of biological and medical applications [85,86]. Of particular interest in regenerative medicine and tissue engineering are fibers that could potentially be tailored to imitate natural extracellular matrix (ECM) in terms of structure, chemical composition, and mechanical properties. The natural ECM in human tissues is mainly composed of proteoglycans (GAG), and fibrous proteins possess nanoscale structural dimensions [87]. In this context, nanofibers present scaffolds directing cellular behavior and dissipate as host cells repopulate and re-synthesize a new natural ECM. The ECM molecules surrounding cells provide mechanical support and regulate cellular activities [88]. Studies have demonstrated that scaffolds comprised of nanoscale structure favor cell adhesion, proliferation, and function, and nanofibrous scaffolds, regardless of composition, promote biocompatibility better than do either meso-scale or micro-scale counterparts [89,90]. Some synthetic polymers have been assessed in tissue engineering as providing useful biological interaction if formed into nanofiber diameters varying from a few tens to a few hundred nanometers. Typically these include biologically

useful synthetic polymers like polyglycolide (PGA), poly (L-lactic acid) PLA, and their copolymers poly (glycolide-*co*-lactide) (PLGA) and poly (*ε*-caprolactone) (PCL) [91]. Studies have demonstrated favorable biological responses for seeded cells such as enhanced cell attachment and *in vitro* proliferation. More recently interest has focused on synthesis of the natural polymer-based nano-fibers alginate and chitosan because of their proven biocompatibility and resorbable biodegradation products [92].

The beneficial attributes of natural polymers include hydrophilic capabilities, non-toxic and immunogenic properties, and enhanced cell adhesion and proliferation [93]. Collagen, gelatin, hyaluronan, alginate, and chitosan are the most commonly used natural polymers for tissue engineering [94], although collagen is very expensive so others are more often more used. In recent studies, collagen and chitosan were successfully fabricated into nanofibers showing respectable tissue compatibility [84,95,96]. The capacity to generate nanofibrous matrices from natural polymers, especially those derived from plants and crustaceans, may provide virtually unlimited resources for development of tissue-compatible scaffolds for functional restoration of damaged or dysfunctional tissues. At present, these problems rely mainly on autograft and allograft (Table 2), and surgical procedures face challenges of limited resources, risk of infection, and viral transmission [97,98].

Table 2: Pros and Cons for Autograft and Allograft Applications

AUTOGRAFT (patient's own tissue)	**ALLOGRAFT (other patients' tissue)**
PROS: No immunosuppression	CONS: 2-month immunosuppression
CONS: Cell culture takes 1-month	PROS: Good cells readily available
Graft delay and scarring	Grafting within 12 hours no-scar
Elderly cells less regenerative	Young cells rejuvenate
High QA/QC costs for each individual graft	Low QA/QC cost for 50 grafts at time
Host limitation	Unlimited supply
Infected/mutated host tissues may contaminate system	Patients with infections and genetic diseases can be treated

3.2 Procedure Producing Alginate Fibers

Alginate is a biodegradable polymer derived from seaweed that bears structural resemblance to glycosaminoglycan (GAG), an important component of ECMs found in tissue [99]. Alginate is a linear polysaccharide copolymer consisting of two sterically different repeating units, (1→4)-α-L-guluronate (G unit) and (1→4)-*β*-D-mannuronate (M unit) in varying proportions [100]. Alginate has been studied extensively due to its unique tissue compatibility and intriguing applications in tissue engineering incorporating regeneration of skin [101], cartilage [102], bone [103], liver [104], and cardiac tissue [105]. Using standard electrospinning techniques, our lab was the first to fabricate alginate-based nanofibers [96] and study the resulting structural, mechanical, and biological properties.

Although electrospinning has proved to be an effective way to generate nanofibrous structures for many materials [86,90,91,106] fabrication of alginate nanofibers by

electrospinning still presents challenges. Alginate solution gels at a very low polymer concentration of around 2wt%, and at this concentration contains insufficient material to generate stable fibrous structure. One method of attacking this problem is compositing by adding a fraction of a co-polymer and applying surfactants and/or co-solvents to the alginate solution. The underlying principle is to control sol-to-gel transition by interacting additives with alginate solution to reduce viscosity such that gelation onset occurs at a higher polymer concentration. An alternative would be to use an ultrasonic transducer placed within the gelated solution material to relax bonding and lower viscosity of highly concentrated solutions to provide compatibility for high-voltage electro-spinning [107].

In our first attempts we used PEO to control sol-to-gel conditions and gained insight into the molecular chemistry creating a composite mixture of alginate and non-ionic polymer PEO co-polymer having solubility in water, biocompatibility, and biodegradable. PEO interacts with alginate through molecular hydrogen bonding, reducing the viscosity of alginate solution [108]. PEO-alginate solutions were prepared by mixing PEO and alginate at fixed concentration of 4wt% each, and mixed compositions ranging from 40/60wt% to 90/10wt% were investigated. For electrospinning, the spinneret needle tip and fiber collector were positioned at 20cm apart, and a DC voltage of 15 kV was applied between these electrodes. Experimental results indicated that solutions having higher PEO-to-alginate ratios exhibited better electrospinnability and stability, allowing completely “bead-free” nano-fibers (Figure 2) to form at ratios above 50/50wt%. To obtain alginate nanofibers at a higher alginate/PEO ratio, a small amount of Triton X-100™ and DMSO, serving as a surfactant and co-solvent, respectively, were introduced into the polymer

solution. Uniform, continuous nanofibers with alginate-to-PEO ratios ranging from 70/30wt% to 90/10wt% were formulated at typical concentrations of 0.5wt% Triton X-100™ and 5wt% DMSO.

Figure 4 presents SEM images of nanofibers spun from solutions of three different alginate-to-PEO ratios, and insets display corresponding fiber size distributions. For alginate/PEO ratios in the range of 70/30wt% to 80/20wt%, cylindrical nanofibers with a mean diameter of ~75nm and a relatively narrow size distribution were obtained. The nanofibers spun from the solution at an alginate/PEO ratio of 90/10wt% resulted in a relatively poor fiber size distribution. The X-ray diffraction (XRD) pattern of as-spun alginate-based nanofibers is shown in Figure-3A along with XRD pattern of as-received alginate powder for comparison. The alginate powder showed no distinct peaks, indicating its amorphous structure [114]. The alginate nanofiber exhibited a strong band at around 16 degrees, indicating a certain amount of crystallinity. This likely occurred due to realignment of alginate chains during electrospinning process to form a higher degree of molecular order in the material structure.

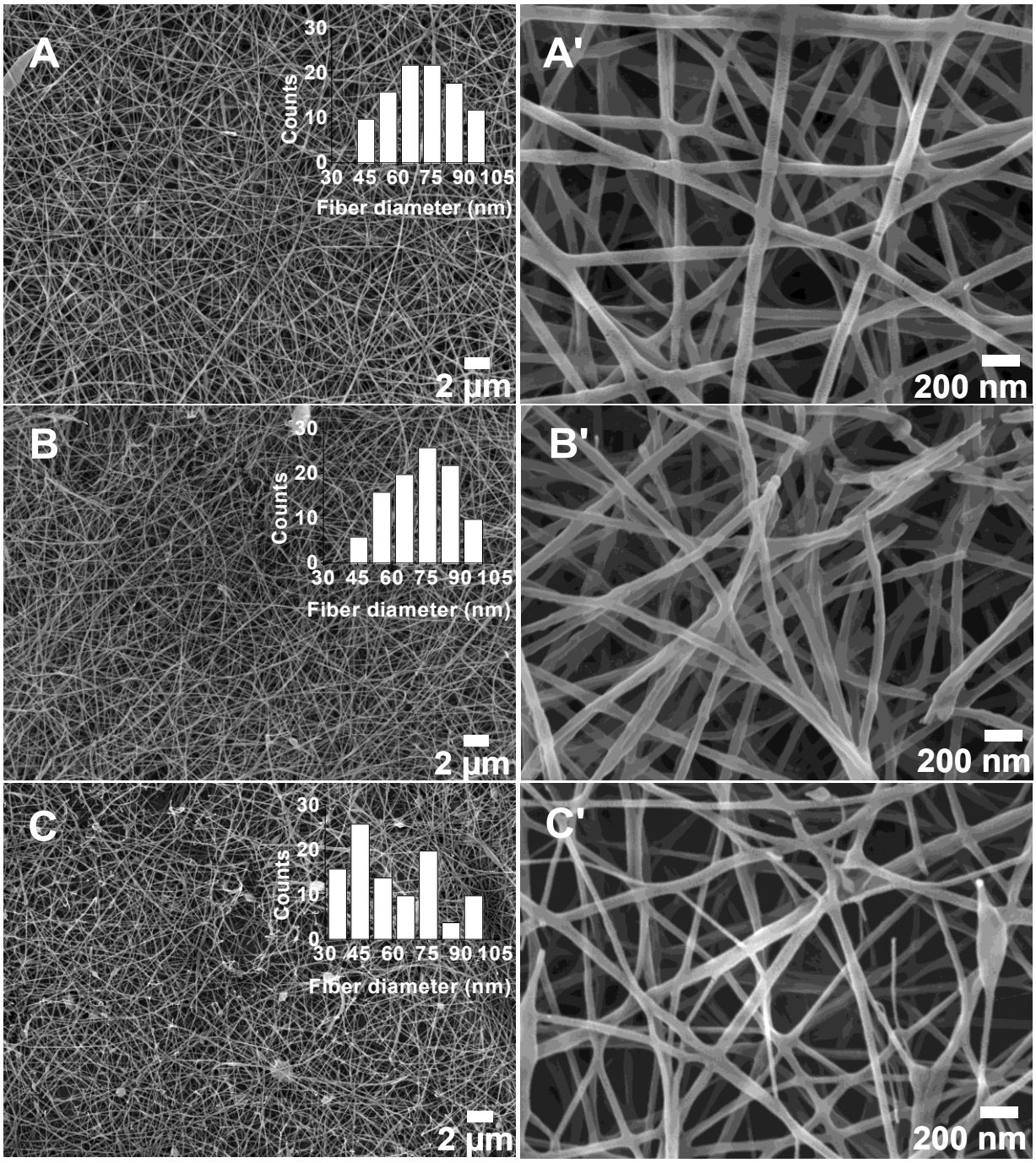

Figure 4. SEM images of alginate-PEO nanofibers: (A), (B) and (C) are survey images of the nanofibers spun from solutions with alginate/PEO ratios of 70/30, 80/20, and 90/10, respectively. (A'), (B') and (C') are corresponding high magnification images of (A), (B) and (C). The insets are the fiber size distributions. All polymer solutions were prepared with addition of 0.5 wt% Triton X-100™ surfactant and 5 wt% DMSO cosolvent.

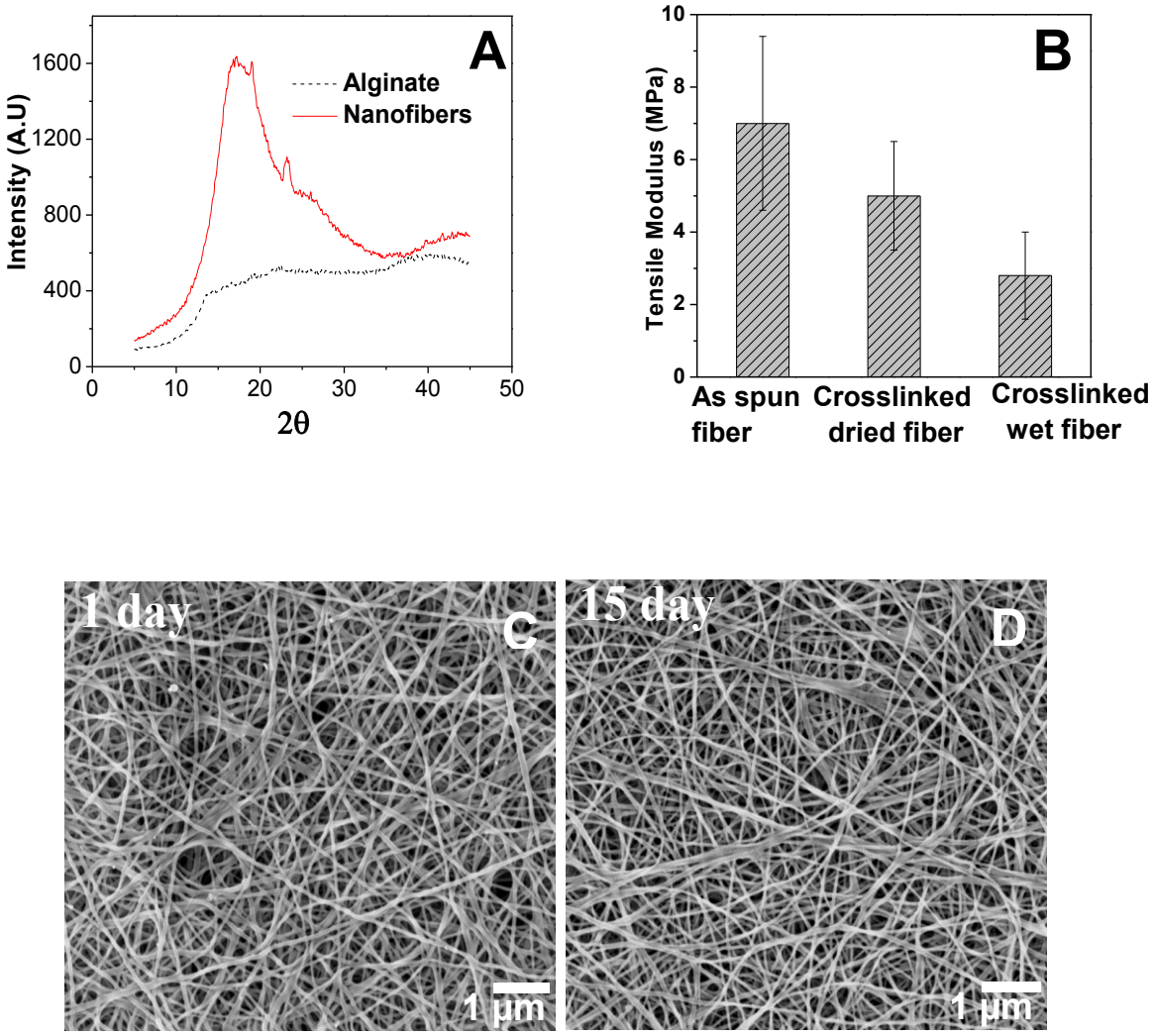

Figure 5. (A) and (B) are XRD patterns and mechanical tensile modulus of alginate-based nanofibers, respectively. (C) and (D) are the SEM images of nanofibers after immersion in DI water for 1 and 15 days, respectively. The ratio of alginate/PEO is 80/20.

3.3 Procedure Producing Chitosan Fibers

An even more interesting natural polymer than alginate or synthetics is chitosan and the ability to fabricate nanofibers of controllable size and anisotropy to form non-woven mats or 3-D porous structures, especially in aligned fashion. Chitosan would provide an unlimited material source for the development of natural polymer-based ECMs due to the abundance of arthropoda. Chitin occurs as the main organic component of crustaceans, shellfish-like shrimp, crabs, and squid. Chitosan is a biopolymer derived from chitin, the most abundant polysaccharide after cellulose. Chitosan is composed of glucosamine and N-acetylglucosamine units linked by 1-4 glycosidic bonds, and molecular weights can vary from 300kD to 1000kD. Chitosan is commercially available in preparations with varying degrees of deacetylation (extra NH_2) ranging from 50% to 90% concentration. This crystalline polysaccharide is soluble in solution with pH < 6 through protonation of the free amino groups. Chitosan is highly charged in solution and can form insoluble ionic complexes with a wide variety of water-soluble polyanionic species, including heparin and alginic acid [117,118,119].

As with alginate, a number of factors also affect the desired success of electrospinning chitosan nanofibers, with the major issue being current electro-spinners and solution viscosity influencing solution spinability and morphology of as-spun fibers [35,39,85,109]. Attempts [110,111] to prepare chitosan-based nanofibrous structures by electrospinning have met with varying degrees of success due to chemistry complications associated with chitosan's poor solubility and high viscosity in aqueous solution. At low polymer

concentrations chitosan solution is insufficient in material content for producing stable solid nanofibers. Increasing chitosan polymer concentrations increases the number of direct inter-chain associations of chitosan molecules that rapidly reach a critical value allowing 3-D network structure to form, but at a highly viscous gel that renders the solution non-spinable using standard static or dynamic electrospinner techniques. As in alginate nanofiber fabrication, introducing PEO reduces chitosan solution viscosity by interacting with chitosan chains through hydrogen bonding and thus rendering the solution spinable at higher chitosan concentrations. For applications such as controlled drug release where only the biocompatibility and degradability of the material are of major concern, a high PEO content in fibers is acceptable and in some cases a desirable configuration. It is desirable to have as high concentration of chitosan as possible in organized (aligned) nanofibers in view of its ability to elicit new tissue formation for applications in tissue repair or remodeling. For these purposes chitosan serves as a scaffold supporting cell attachment, differentiation, and growth; however, where mechanical integrity is critical, chitosan nanofibers are lacking at low concentrations.

Chitosan/poly (vinyl alcohol) nanofibers sized from 220nm to 650nm and chitosan nanofibers with a mean diameter of 330nm have been reported [110], and in a more recent report, polyethylene oxide (PEO) was introduced into chitosan for fabricating ultrathin hybrid nanofibers [111]. That study indicated that the spinability of chitosan solutions depends strongly on the mass ratio of chitosan to PEO and that a nanofibrous structure with diameters from 80nm to 180nm was achievable using a solution of PEO to chitosan weight ratio in equal amounts. To study how chitosan/PEO ratio content in our system affected viscosity and spinability, we measured shear viscosity as a function of shear rate

for solutions by varying composition ratios. We began with a 2% chitosan solution and 3% PEO solution prepared by separately dissolving chitosan and PEO in 0.5M acetic acid, followed by centrifugation to remove air bubbles from both. The two solutions were combined to achieve the final weight percent ratio of chitosan to PEO in mixtures of 60/40wt%, 70/30wt%, 80/20wt%, and 90/10wt%, with each mixture being stirred for 5 hours. Solutions containing 0 to 0.5wt% of Triton X-100^{TM} and 0 to 10wt% of dimethylformamide (DMF) were then mixed with chitosan/PEO solutions, stirred overnight, and then centrifuged to remove gas bubbles. The shear viscosities of the solutions of different chitosan/PEO ratios were measured using a shear rate ring of 5 to 500 s^{-1} on a Haake Viscometer (VT550) equipped with double concentric cylinder-type SP2P sensors. The results are shown in Figure 6 and the corresponding images of the as-spun products

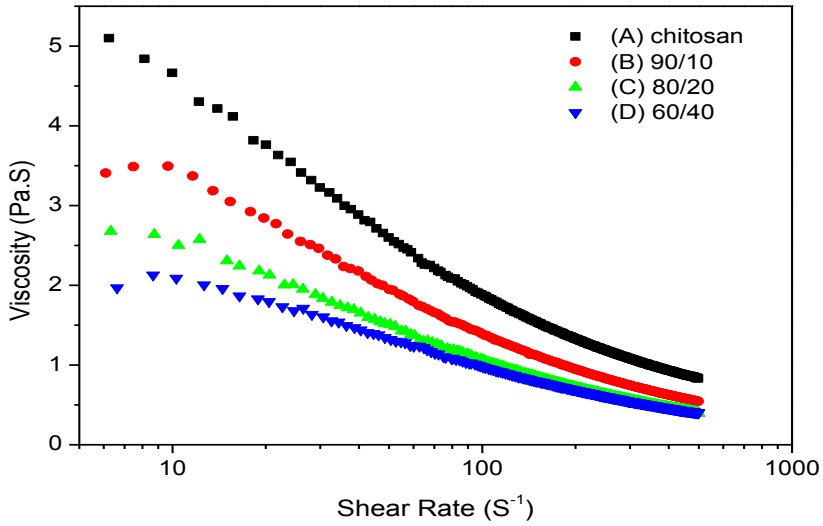

Figure 6. Polymer solution shear viscosity as a function of shear rate, prepared from 0.5M acetic acid solution with different polymer concentrations and chitosan to PEO ratios (A) 2%, chitosan/PEO = 100/0; (B) 2.05%, chitosan/PEO = 90/10; (C) 2.1%, chitosan/PEO = 80/20; and (D) 2.2%, chitosan/PEO = 60/40.

are shown in Figure 7. Figure 6 illustrates that the viscosity of the polymer solution decreases monotonically with increasing PEO content.

As displayed in Figure 7A, pure chitosan solutions with polymer concentrations equal to or less than 2% are materially insufficient to yield fibrous structure and only sprayed droplets were obtained. Solutions with polymer concentrations above 2% are too viscous for current electrospinner concepts. These effects are due to the high viscosity of chitosan polymer, which impedes continuous flow of the polymer solution through the charged spinneret capillary tip, demonstrating that a pure chitosan solution, by itself, could not be directly electrospun to create fibers.

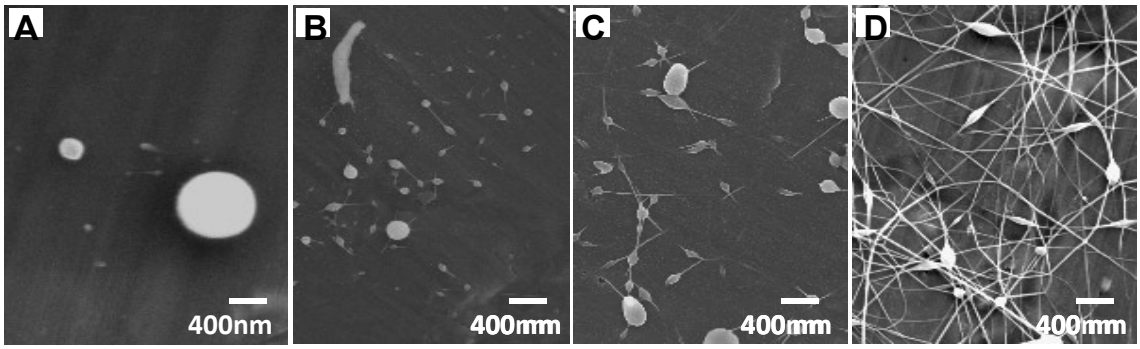

Figure 7. SEM images of the products electrospun from solutions of different chtiosan/PEO weight ratios and polymer concentrations:
(A) 100/0 and 2%; (B) 90/10 and 2.05%; (C) 80/20 and 2.1%; and
(D) 60/40 and 2.2%. The corresponding viscosity of these solutions is shown in Figure 6.

The morphological change of the as-spun fibers, as shown in Figures 7B, 7C, and 7D, corresponds well to a decreasing trend in viscosity, transforming progressively from a beadlike structure into a fibrous structure as PEO-to-chitosan ratio increases.

The viscosity of a polymer solution is in the characteristics of intermolecular interactions between the polymer chains, and the high viscosity of chitosan solution is due to strong hydrogen bonding between NH_2 and OH groups in chitosan polymer chains. The decrease in viscosity with addition of PEO can be attributed to the change in inter- and intra-molecular interactions of these chains. PEO molecules bond onto chitosan backbone chain, disrupting the self-association of chitosan chains by forming new hydrogen bonding between its OH groups and water molecules. Physically, this modulation in associative forces by PEO is manifested as an increase in chitosan solubility and a decrease in its solution viscosity.

As displayed in Figure 7B, the maximum chitosan/PEO ratio producing a spinable solution is 90/10wt%, above which the spun product exhibits a non-uniform structure or droplets (Figure 5A). At this chitosan/PEO ratio the electrospinning does not produce a desirable fibrous structure, but instead short fibers and a considerable amount of beads. To improve the spinability of the chitosan/PEO ratio of 90/10wt%, a 0.3% of Triton X-100^{TM} was introduced into the stock solution as a surfactant. Figure 8A shows the SEM image of the electrospun structure with an adjusted polymer concentration of 2.05wt% and a chitosan/PEO ratio of 90/10wt%.

Compared to the same solution but without the surfactant (Figure 7B), the addition of Triton X-100^{TM} substantially improved the electrospun structure, but beadlike structures were still embedded within the fibers (Figure 7B). Further improvement in structural uniformity was achieved by introducing DMSO as a cosolvent in the polymer solution. Similar approaches have been reported using polar or non-polar cosolvents to improve the

electrospinnability of polymer solutions [112]. In Figures 8B and 8C, SEM images illustrate chitosan nanofibers obtained after introduction of DMSO as a cosolvent. The nanofibers shown in Figure 8B were collected from a stationary collector whereas those shown in Figure 8C were collected from a cylindrical drum collector rotating at a speed of 2000 rpm. Figures 8D and 8E show the images of the nanofibers presented in 8B and 8C, respectively, at higher magnification. The average fiber diameters estimated from the images were 42 ± 8 nm and 69.5 ± 12 nm, respectively. The rotating drum collector technique is capable of producing nanofiber diameters adjustable from a few microns to approximately 40 nm by modulating polymer and surfactant concentrations.

As illustrated in Figures-8A to 8E, the fibrous structure is substantially improved having introduced a cosolvent, as fibers collected on both stationary and rotating drum collectors were virtually bead free. An apparent degree of fiber alignment is also observed on the rotating collector, Figure 8C, due to stretching of nanofibers as they attach to the rotating drum, forcing them into aligning.

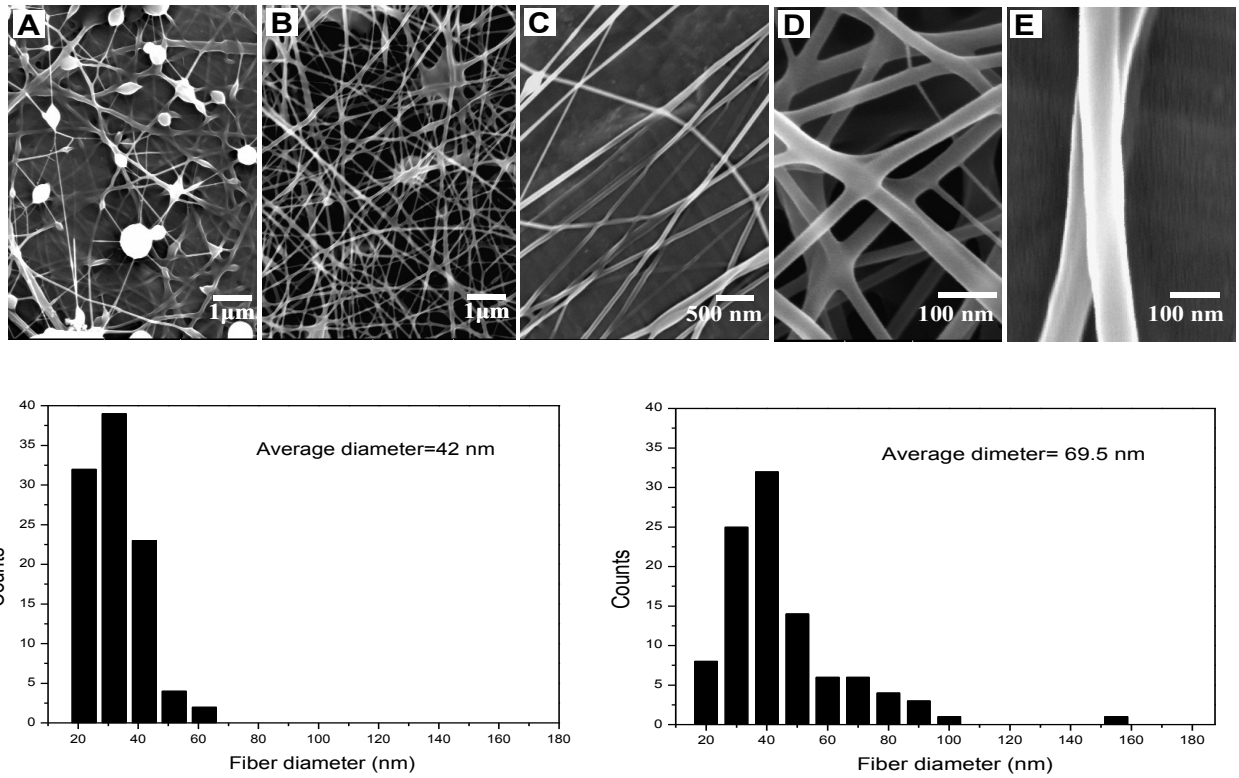

Figures 8A – 8E. SEM images of electrospun structures (chitosan/PEO ratio = 90/10) prepared from 0.5M acetic acid solutions containing: (A) 0.3 % Triton X-100™, (B) and (C) 0.3% Triton X-100™ and 10% DMSO. Fibers in image B (average fiber diameter = 43 ± 8 nm) were collected on a stationary collector, whereas fibers in image C (average fiber diameter = 65 ± 11 nm) were collected on a cylindrical collector with a rotating speed of 2000 rpm. Images D and E are the high-magnification images of B and C, respectively. The average diameter of electrospun nano-fibers was determined by measuring the diameters of the nanofibers in 100 different points of a 645 × 484 SEM image using Microsoft photo shop program (Photoshop 7.0). Fiber size distribution of the electrospun fibers of the images C and D of Figure 8.

3.4 Aligning Fibers

The ability to align electrospun fibers would be significant and have many interesting applications in tissue engineering, particularly in the development and remodeling of native tissue, of which the majority are anisotropic [112]. A rotating collector can be used to produce fibrous structures possessing a certain degree of alignment dependent on drum

collector rotational speed [113]. An even higher degree of alignment can be achieved by either modulating the electric field configuration [114] through spinneret-collector polarity switching or depositing fibers in small, confined parallel collector areas. One particular study [160] achieved a high degree of fiber alignment by attaching a small, single, flat, bare copper plate conductor onto an insulated disk perimeter acting as the grounded collector electrode. The resulting specimen size was less than desired, although it demonstrated that fibers tend to align collinearly with electrical current direction. This particular electrode configuration illustrated the advantages of geometrical confinement and electric field configuration that provide better control over directional fiber alignment using a simple setup, varying fiber arrays using rotatable copper plates on disk edge, and creating bundle fibers. The disadvantages were inability to retain high fiber alignment at a constant rotating speed as fiber deposits thicken and increase disk radius. This modifies fiber size due to diminishing distance between spinneret and collector, and a small area collector plate is all that is provided for alignment of fibers on disk edge [160].

This same effect was observed in our lab experiments using a single, bare, round copper wire wound completely around a spinning cylindrical drum collector. The syringe tip and the surface of copper wire were separated by approximately 20cm, but maintaining this distance was a problem as previously found [160], and monitoring and controlling fiber thickness presented great difficulty. The rotation speed of the collector was varied between 100 rpm to 5000 rpm, with all other experimental conditions remaining the same as those under which fibers shown in Figure 6 were produced. After 15 minutes of fiber deposition, a filament structure consisting of aligned nanofiber aggregates had formed along the

surface of copper wire and was manually detached for examination. The degree of the fiber alignment improved substantially as the rotating speed of drum collector increased, attaining highest degree of alignment at approximately 2000 rpm with further speed increase presenting no apparent improvement. Figures 9A and 9B illustrate an exemplary image of a fiber bundle prepared on a wire collector of 200μm in diameter. The bundle has a diameter at approximately 50μm and contains fibers having an average diameter of 115 ± 10 nm.

The chitosan/PEO solution for electrospinning was gravity fed into a 3mL disposable syringe having needle with an inner diameter of 0.5 mm (25-gauge). The solution feed rate is driven by the tilt angle of syringe, with electrospinning similar to that reported previously [112].

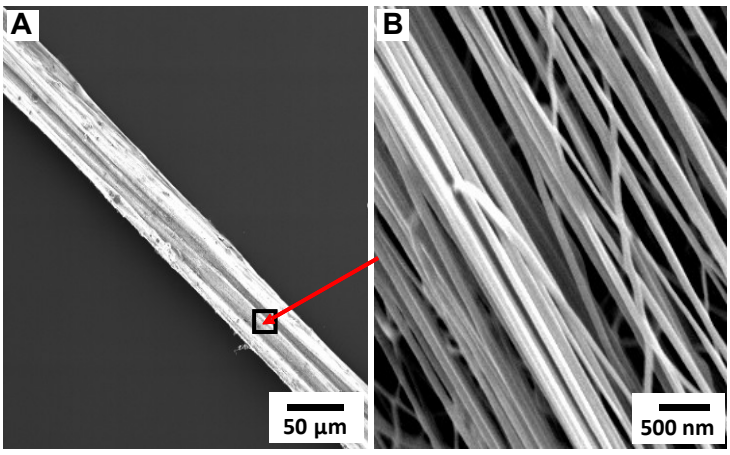

Figure 9. (A) A fiber bundle collected on the surface of a thin copper wire mounted on a rotating drum; (B) high-resolution SEM image of aligned nanofibers in the bundle. The chitosan/PEO ratio was 90/10 with 0.3% surfactant and 10% DMSO.

An electric field gradient, provided by a DC voltage of 20–25 kV (Del Electronics Corp.), was applied between the syringe tip and a 7.5-cm (3 inches) diameter cylindrical drum collector electrode wrapped with an aluminum foil ban as the grounding electrode attached to power supply ground and driven by a variable speed DC electric motor. The typical distance between the spinneret syringe needle tip and the grounded collector electrode drum was 17 to 20 cm, which provided useable fibers. The resulting electrospun nanofiber mat was then sputter-coated with Au/Pd and morphology of nanofibers was examined using a scanning electron microscope (SEM) (JEOL JSM-840A) at an accelerating voltage of 10 kV. The nanofiber diameters were determined using product SEM images imported into Adobe Photoshop.

PEO is widely accepted as a biocompatible material, but it readily dissolves in water, which is not always desirable for tissue engineering applications. Our chitosan/PEO nanofibers with high PEO content dissolved quickly in water, completely losing their fibrous structures in a few days. These efforts to fabricate natural polymer-based fibrous structures are still encouraging, but much work remains to be explored and improved upon, particularly in respect to *in vivo* applications. Even with current electrospinning processes [113], more studies are required to understand fiber fabrication and orientation by enhancing the control of mechanics in the formation of fibrous assemblies through various polymer solutions and electrostatic field configurations.

It is vital to gain a better understanding of the various parameters and processes that allow for fabricating desired fiber assemblies for specific tissue engineering applications.

CHAPTER 4: Cell Culture Procedure with Chondrocytes and Osteoblasts Cells on Alginate Nanofibers

Cell viability tests were conducted on alginate nanofibers using chondrocyte (HTB-94) and osteoblast (MG-63) cells plated separately in tissue culture flasks and grown in culture medium containing 10% fetal bovine serum (FBS) in 1mL of Dulbecco's Modified Eagle Medium (DMEM). The media was replaced every three days and cells were maintained in a humidified incubator at 37°C and 5% CO_2 gas content. Once cells reached 80 to 90% confluence, they were trypsinized and counted with a hemocytometer. Nanofibrous membranes of approximately 50μm in thickness were deposited on glass cover-slides measuring 25mm^2 and washed several times with 75% ethanol and deionized water at a neutral pH to remove residual solvent and surfactants introduced during electrospinning process.

The membranes were then air-dried and washed four times with PBS 10^5 MG-63 or HTB-

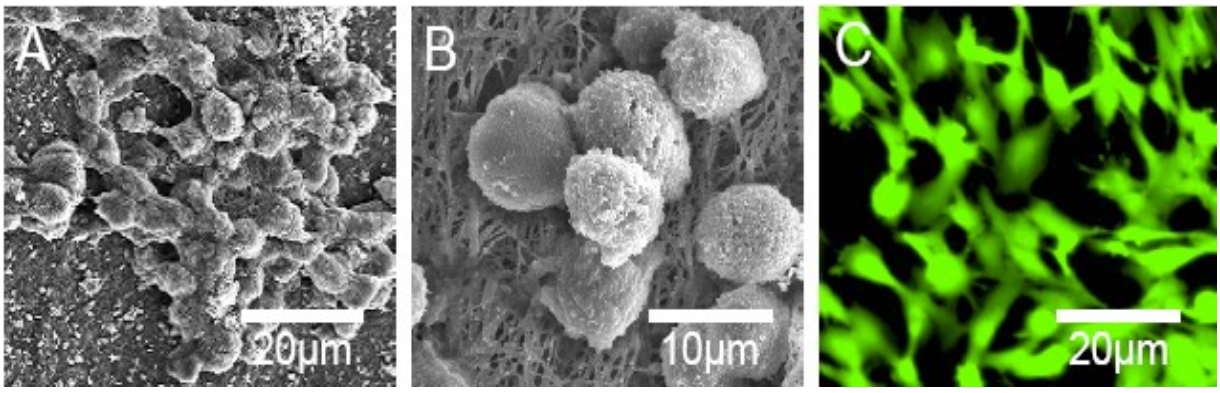

Figure 10. Evaluation of Cellular compatibility of alginate-based nanofibers (alginate/PEO is 80/20) *in vitro*. SEM images of chondrocytes grown on alginate nanofibers: (A) survey image, (B) high-magnification image, and (C) fluorescence image of cells on nanofibers with the live/dead cell stain.

94 cells in 1ml D-MEM cell culture medium containing 10% fetal bovine serum (FBS), 50IU.ml^{-1} penicillin, and 50μg.ml^{-1}streptomycin and then seeded onto nanofibrous membranes in 24-well culture plates. The cellular constructs were harvested after three days, washed with 1xPBS, and fixed with Karnovsky's fixative overnight at room temperature. All samples were gradually dehydrated with 50%, 75%, 95%, and 100% ethanol, respectively over two hours each. The samples were dried using critical point dryer and coated with Au/Pd for SEM imaging. Cells formed clusters on the nanofibrous structure that were round in shape maintained their characteristic phenotypes. Round cellular morphology is indicative of characteristic function of chondrocytes resulting from organization of sparse active filaments [119]. Figures 1A and 1B show SEM images of chondrocyte cells cultured on the alginate-based nanofibers for 72 hrs as shown in Figure 1C.

4.1 Cell Viability and Morphology Determination on Chitosan Nanofiber

Cell viability on seeded chitosan was then examined by using fluorescence microscopy and the live-dead assay technique (colors; green live, red dead). Chitosan nanofibrous membranes and chitosan cast films for comparison were deposited on glass substrates, sterilized, and seeded with cells. After incubation in culture medium for 48 hrs the substrates were washed twice with 2ml of Tyrode's Hepes buffer (140mmol/l NaCl, 0.34mmol/l Na_2HPO4, 2.9mmol/l KCl, 10mmol/l Hepes, 12mmol/l NaHCO3, 5mmol/l glucose, pH 7.4). Cells are stained for a period of 5 min with 2ml of Tyrode's Hepes buffer containing 2 mmol/l calcein-AM and 2mmol/L ethidium homodimer-1 (Molecular Probes, Eugene, OR). Calcein-AM is a nonfluorescent cell-permeant fluorescein derivative that can

be converted by cellular enzymes into cell-impermeant, a highly fluorescent calcein. Calcein accumulates inside live cells with intact membranes and causes cells to fluoresce green. Ethidium-homodimer-1 enters dead cells with damaged membranes and undergoes a 40-fold enhancement of fluorescence upon binding to their DNA, causing the nuclei of the dead cells to fluoresce red. This double-staining allows for simultaneous examination of both live and dead cells on fiber mat material surface. Cells can also be seeded on membranes, incubated for different time periods, and fixed with Karnovsky's fixative overnight at room temperature. After fixation, the membranes are rinsed three times with PBS and once using de-ionized water, and then dehydrated in 50%, 75%, 95%, 100% ethanol, respectively, for 2 hrs. Lastly, the samples were dried using a critical point dryer and then coated with Au/Pd. Cell morphology was examined using scanning electron microscopy (SEM).

4.2 Integrity of Nanofibrous Structure in Water

Polyethylene oxide has high solubility in water, and electrospun pure PEO fibrous membranes dissolve quickly in water at 37°C. Thus, it is of practical interest to study the effect of the amount of PEO in chitosan/PEO nanofibers on the integrity of the nanofibrous structure in water. As shown in Figure 2 (lower panel), the membrane made of nanofibers containing 40/60wt% PEO completely lost its initial fibrous structure after immersion in water for 7 days, and substantial swelling was observed. For membrane made of nanofibers with 10wt% PEO (top panel), no significant change in morphology was observed for the same time period and the integrity of the fibrous structure in water was

retained. A prolonged immersion of the membrane in water up to four weeks (data not shown) led to slight swelling of fibers but virtually unchanged fibrous morphology.

4.3 Cell Adhesion, Spreading, and Viability

The nanofibrous membrane containing 90wt% chitosan and 10wt% PEO, identified above to have structural integrity in water, was studied for cellular compatibility. This was accomplished by culturing osteoblasts (bone cells) and chondrocyte (cartilage) cells on nanofibrous membranes in cell culture medium. Figure 12 shows fluorescence images of chondrocyte cells cultured on fibrous membrane (left) and on chitosan/PEO cast film of chitosan/PEO ratio (90/10). Live cells that stained green appear to adhere well, exhibiting a normal morphology on fibrous mat surfaces. Live cells on the nanofibrous membrane appeared to be substantially more abundant than those on the cast film, and exhibited a distribution of higher uniformity. Dead cells, stained red, were barely found on both types of surfaces. Good cell adherence on the electrospun nanofibers might be due to the large surface area available for cell attachment on chitosan nanofibers after 5 days of cell culturing. Cells were attached to the fiber surfaces by discrete filopodia and exhibited long and numerous microvilli on their surfaces. Cell adhesion, spreading, and interaction with nanofibrous membrane were studied using SEM images. Figures 13A and 13B show SEM images of osteoblasts (MG-63). It is interesting to note that microvilli of cells tend to attach and grow along the polymer nanofibers having similar diameters.

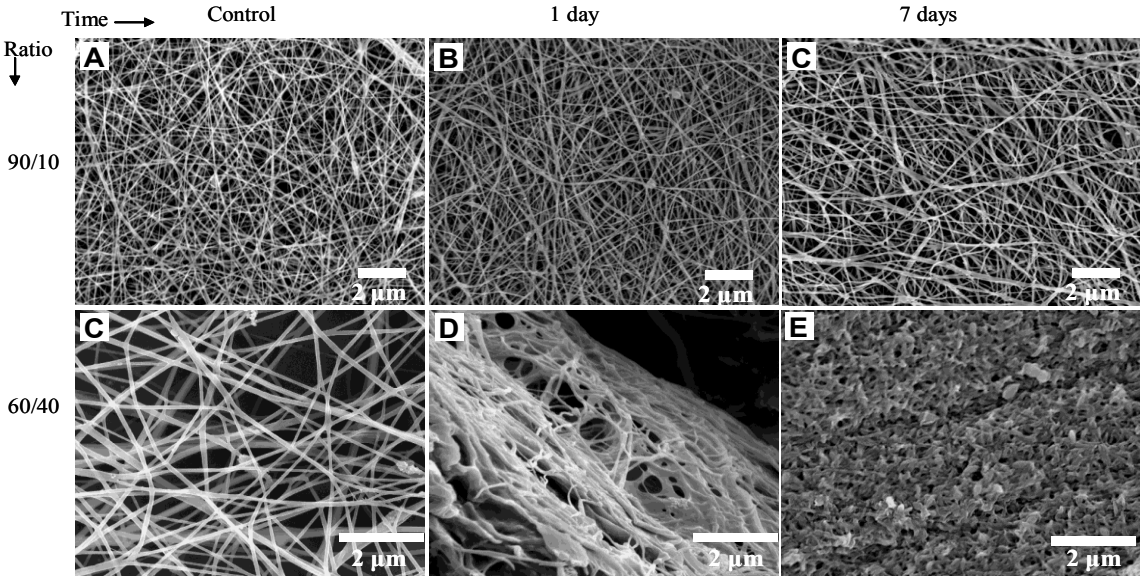

Figure 11. SEM images of the chitosan/PEO fibers with ratio of 90/10 and 50/50 showing the morphology of fiber structure after immersing in water (pH 7.5 at room temperature) for different times. All the conditions for the fiber preparations were same as in Figure 12 (C).

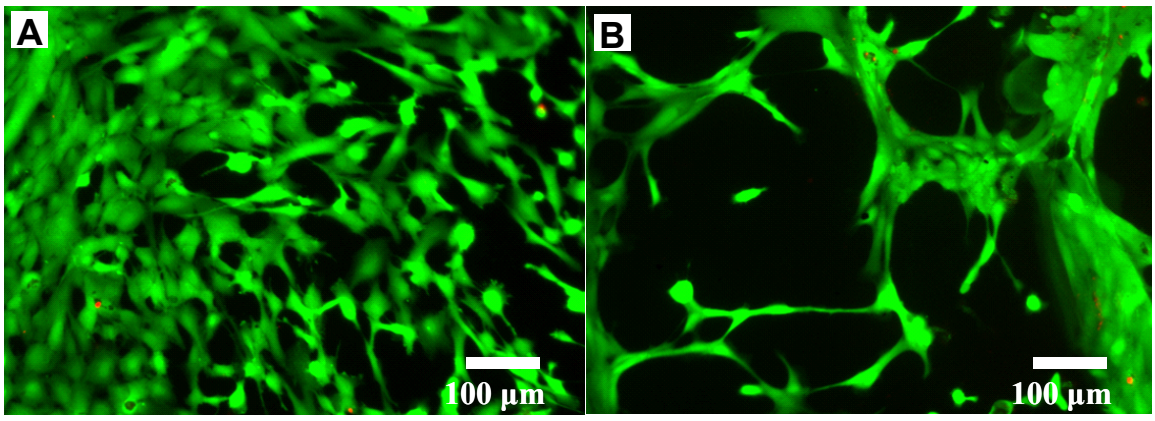

Figure 12. Live (stained green) and dead (stained red) staining of the chondrocytes cultured for 1 day; (A) nanofibrous membrane of chitosan/PEO (90/10), and (B) solvent cast film of the same chitosan/PEO (90/10).

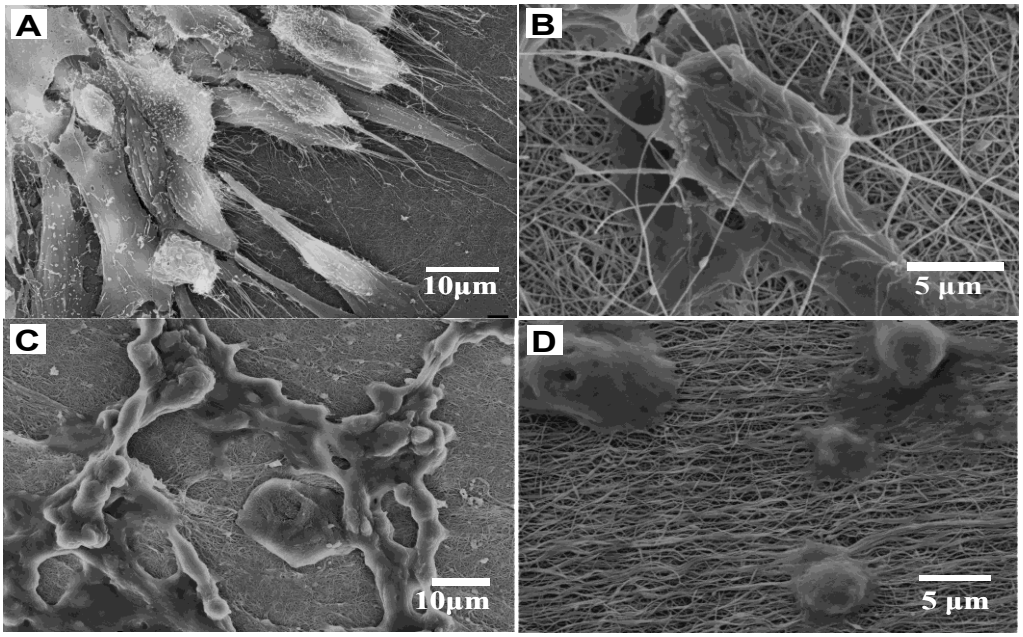

Figure 13. SEM micrographs of osteoblasts (MG-63) (A and B) and chondrocytes (HTB-94) (C and D) seeded on nanofibrous membrane of chitosan/PEO (90/10) after 5 days and 3 days culture, respectively; (A) 800 × original magnification, (B) 3500 × original magnification, (C) 800 × original magnification, and (D) 2500 × original magnification. Magnified images show the attachment of both cell types with two fibrous structure of the electrospun membrane.

Figures 13C and 13D show SEM images of chondrocyte (HTB-94) cells grown on chitosan nanofibers after 5-day culture at different magnifications. Cells adhered and proliferated well and exhibited the characteristic round shape of chondrocytes, indicating that chitosan nanofibers maintain the phonotype of chondrocytes promoting cell–matrix and cell–cell interactions. Cytoplasmic processes and extensions that are attached to the surface of nanofibrous membrane are clearly observed on SEM images of osteoblasts, Figure 13.

CHAPTER 5:
Polymer Nerve Guide Example of Using Electrospun Nanofibers

Nano- and micro-fibers are expressly important in tissue engineering as they emulate natural cellular environment dimensions [119]. Aligned nanofibers are of specific interest to nerve tissue engineering as diameters of axons and myelinated nerve fibers are on the order of a few to tens of microns [120-122]. Consequently, aligned nano- and micro-fibers can be used as sacrificial scaffolds of tubular fabricated nerve tissue engineered as aligned micro-channels. These micro-channels are anticipated to provide micron-scale contact guidance for regenerating axons and nerve fibers. Nerve tissue engineering scaffolds with channels have been reported; however, the number of channels is relatively low and the diameters large at roughly 200μm [123].

This chapter, in addition to the materials stability test, demonstrates that the developed electrospun nanofibrous matrix has high mechanical and chemical stabilities in aqueous environments when using proper polymer solution and electrospinning techniques.

5.1 Nanofiber Synthesis Procedure

The following discusses the experimental procedures employed to synthesize nanofibers using standard electrospinning drum technique. Development of polymeric nanofibers is of great scientific and technological interest because of their wide-ranging applications in biomedicine and biotechnology [124-126]. Particularly, composite nanofibers, capitalizing on the favorable biological properties of the natural polymer and mechanical strength of the synthetic polymer, represent a major advancement in tissue engineering and

regenerative medicine. However, the development of well-blended natural–synthetic composite polymers remains a great challenge due to the poor miscibility of the component polymers, where natural polymers are generally soluble in aqueous and polar solvents, but most synthetic polymers are not. Poorly blended polymeric nanofibers exhibit weak mechanical strength and uncontrollable material properties as a result of inhomogeneity.

5.1.1 Synthesis of Chitosan-PCL Nanofibers by Electrospinning

The following demonstrates the development and characterization of a natural–synthetic polymeric nanofiber comprised of well-blended chitosan and poly-caprolactone (PCL). The design combines the technological advances in biocompatible polymers and nanotechnology to produce nanofibrous matrices with significantly improved mechanical and biological properties. Five (5) wt% chitosan solution was prepared at elevated temperature, which weakens intermolecular forces between polymer chains and increases the solution solubility. The chitosan was fully dissolved by refluxing the chitosan/TFA mixture for 3 hrs at 80°C, and the 10wt% PCL solutions were prepared by dissolving PCL in TFE (Sigma). The two solutions were mixed at varying weight ratios of chitosan: PCL and vortexed (vibration mixed) for 2 min. Acidic hydrolysis of the PCL by TFA limits the lifespan of the mixture for electrospinnability to about 1 hr after both components mix, requiring component mixing immediately prior to the electrospinning process, or continued mixing of the two solutions during the electrospinning in the production settings [127,128].

The electrospinning instrumentation used in this study was reported previously [129, 130]. Briefly, a DC voltage of 17–20 kV with low output current was applied between a syringe tip and a collector at a distance of 17–20 cm. Solution for electrospinning was fed into a 3-ml disposable syringe fitted with a pipette tip of 0.5 mm in diameter. The solution feed was driven by the gravity and the feed speed was controlled by the tilt angle of the syringe. For all experiments, solution flow rate was maintained at 0.95 ml h-1. The nanofibrous conduits were fabricated by depositing the fibers on a stainless steel rod collector. The tubular constructs were removed from the rod and dried for 24 hrs prior to testing. Alternatively, fibrous mats were collected on larger-diameter spindles.

5.2 Synthesis of Chitosan-PCL Cast Conduits

The solvent-cast conduits were prepared by dip coating. A 16-g needle was dipped into the chitosan-PCL mixture, allowed to dry at room temperature (5 min), and then heated to 60°C (15 min). This coating process was repeated several times depending on the thickness of the conduit to be made. The samples were heated to 60°C for 2 hrs, cooled to −20°C for 30 min, and then warmed to room temperature. The tube was then removed from the needle and stored under ambient conditions prior to use.

5.3 Fabrication of Other Nanofibers and Films

PLGA and PCL nanofibers and chitosan-PCL films were prepared for comparison to chitosan-PCL nanofibers. A 7wt% PLGA and 10% PCL were dissolved in DMF and TFE, respectively. Prior to spinning, the PLGA solution was diluted by 40wt% DMSO. For

chitosan-PCL film, 2wt% PCL and chitosan solutions were prepared in TFE and TFA, respectively. A 40:60 chitosan-PCL solution was prepared and vortexed for 2 min. A 200μL solution was deposited on 12-mm round cover slips and spin-coated at 500 rpm for 30 s. After coating, the spinning was continued at 1000 rpm for 1 min to remove excess solution and expedite solvent evaporation. After drying, the film was neutralized with 14% ammonium hydroxide for 15 min and rinsed with copious amounts of DI water to remove residual base.

5.4 Microscopic Imaging of Nanofibrous Structures

Electrospun structures were soaked in 14wt% ammonium hydroxide solution for 5 min and rinsed with DI water three times. The samples were dried under reduced pressure at room temperature. Nanofibrous morphology was examined by SEM at an accelerating voltage of 10kV after sputter-coated with Au/Pd. TEM was used to observe internal features of the nanofibers. A thin nanofibrous membrane was sandwiched in a PELCO® folding grid and examined at the membrane edge.

5.5 Degradation of Nanofibrous Matrix

Dried chitosan-PCL nanofibrous membranes were cut into squares (15 × 15 mm2), neutralized in 1N-NaOH, washed with deionized water, sterilized in absolute alcohol (10 min incubation), and washed thoroughly with PBS. Membrane integrity was then tested by incubating samples in 15mL PBS (pH = 7.5, 37°C) with 1 mg/ml lysozyme from chicken egg white (Sigma). The buffer was replaced every 3 days. The samples were taken out from the solution at specified intervals and examined for morphological changes.

5.6 Nanofibrous Matrix Characterization

WAXS [146], wide-angle X-ray scattering patterns were acquired over a diffraction angle of 2θ = 5–45° at room temperature with a wide-angle X-Ray diffractometer with CuKα radiation, operated at 40 kV and 20 mA. Polarized FTIR spectra of 200 scans at $4cm^{-1}$ resolution were obtained using a Nicolet 5DX spectrometer. Dried nanofibrous samples were mounted and the system purged with nitrogen before testing. Thermal properties of chitosan-PCL nanofiber constructs were studied by differential scanning calorimetry under a nitrogen atmosphere at a heating rate of 10°C/min. All the samples were quenched under liquid nitrogen before the heating scans.

5.7 Cell Transfection

Schwann cells (ATCC CRL 2766 SW10, a mouse cell line) were transfected with the GFP plasmid (p-EGFP-N1, 94**%** efficiency) using the effectene transfection reagent kit (Qiagen). Schwann cells were plated on a 10-cm Petri dish (BD Labware; 1.5×10^6 cells/dish) in DMEM media 18 hrs before transfection (all DMEM enriched with 10**%** FBS; Invitrogen). A mixture of DNA condensation buffer (300 µl), plasmid DNA (2 µg), and enhancer (16 µl) was prepared immediately prior to transfection. Cells were incubated in the mixture for 5 min at room temperature, treated with the effectene reagent (100µl added to mixture), allowed to stand for 5 min, and then given DMEM media (7000 µl DMEM added to mixture). Twenty-four hours after transfection the cells were given fresh DMEM media. For rapid selection of cells that stably and uniformly expressed GFP, a two-tiered selection process was used. Two days after transfection, GFP+ cells were initially selected by fluorescence-activated cell sorting (FACS; Vantage SE) and then isolated after

treating the cell population with G418-rich media (1 mg/ml) for 2 weeks. After the selection process flow cytometry showed that > 90% of all cells expressed GFP activity (BD Canto).

5.8 Cell Culture, Attachment, and Proliferation

Fiber samples were wrapped over 12-mm round cover slips and secured with 3.5wt% poly-L-lactic acid in hexafluoroisopropanol. Prior to cell culture, the samples were sterilized overnight with ethanol and equilibrated with DMEM (10v/v% FBS, 100 units penicillin–streptomycin antibiotics) for 24 hrs. PC12 cells were obtained from the American Type collection and maintained in RPMI 1640 medium supplemented with 10% FBS. PC 12 cells were trypsinized for 10 min to dissociate cell clusters, and resuspended in F12K media (1**%** horse serum, 100 units of penicillinstreptomycin, 200 ng/mL NGF). GFP-Schwann cells were resuspended in DMEM (10v/v**%**) FBS, 100 units penicillin–streptomycin, 1 mg/mL G418 sulfate). Then, 25,000 PC12 cells and 12,500 cells of GFP-Schwann cells were separately seeded on PCL, chitosan-PCL, and PLGA nanofibers, chitosan-PCL films, and glass cover slips in 24-well plates. All the samples were prepared in triplicate for each measurement. After 1, 3, and 5 days of culture, the number of Schwann and PC12 cells adhered on the materials were measured with an alamar Blue assay (Biosource International, Inc., USA 542 Flynn Road, Camarillo, CA). The Samples were washed with warm, phenol-free DMEM and incubated with 10 v/v alamar Blue in phenol-free DMEM for 1.5 hrs, and 250μL of culture medium was removed and placed in a 96-well plate. The absorbance was measured at 570 and 600 nm using a spectrophotometer and the **%** reduction of the alamar-Blue solution was calculated. Known cell quantities of both cell lines were also tested to correlate percentage reduction to cell

number. Nanofibrous conduits were sterilized in 75% ethanol for 24 hrs and rinsed with PBS four times. Schwann cells were seeded on the internal surface of the conduit at 1 × 10^6 cells/mL and cultured for 7 days followed by co-culturing PC12 at a concentration of 1 × 10^6 cells/mL (culture media supplemented with 200 ng/mL NGF solution). After 7 days of co-culturing Schwann and PC 12 cells, three samples were harvested for SEM imaging, and 4 days later, the remaining samples were collected for immunochemistry study.

5.9 SEM Analysis of Cell Morphology

Scanning electron microscopy was performed to examine Schwann and PC12 cell attachment. Samples were removed from culture media, rinsed with PBS, and fixed with Karnovsky's fixative overnight. After fixing, samples were briefly rinsed with DI water and dehydrated with sequential rinses of 50%, 75**%,** and 100**%** ethanol for 15 min each. Samples were sputter-coated with Au/Gd for 30 s at 18 mA and imaged with a JSM 7000F.

5.10 Immunocytochemistry

Samples cultured with PC12 cells were removed from cell culture medium and fixed in paraformaldehyde overnight at 4°C. The samples were rinsed with ice-cold PBS three times for 5 min each and blocked with 3% bovine serum albumin (BSA) in PBS for 30 min. The samples were then incubated with a LANGF receptor antibody (200 µg/ml; Abcam) in PBST for 1 hr at 20°C room temperature. Following incubation, the samples were immersed in PBS for 30 min prior to incubation in the presence of FITC-labeled rabbit polyclonal anti-mouse antibody (1:500 dilution in PBS; Abcam) for 1 hr. Finally, the

samples were counterstained with a 1:500 solution of DAPI in PBS for 10 min, and rinsed with PBS prior to microscopy with a Zeiss 510 Zeta Microscope (Carl Zeiss).

5.11 Mechanical Testing

Both wet and dry nanofibrous conduits were evaluated for stress–strain response using a micro-tensile testing machine designed for small samples. For tensile strength tests, conduits were cut and opened to form a rectangular sheet. Wet samples were prepared by incubating the samples in PBS for 24 hrs at 37°C. The tensile modulus was calculated from the stress versus strain curve. Compression study was conducted using a load-strain profile on a dynamic mechanical analyzer. Tubular samples (~15 mm length, 1.5-mm inner diameter and 0.2-mm wall thickness) were set lengthwise in the testing apparatus. Compressive strength was measured as a force applied perpendicular to the axis of the sample and loads were recorded at strains of 10% to 50%. A preload force of 60 mN was applied to each sample with a force ramp rate of 500mN/min and an upper force limit of 6110 mN. Three samples for each condition were tested at 25°C and are presented with error values representing standard error of measurement (SEM) for each sample.

5.12 Statistical Analysis

Statistical analysis of the PC12 proliferation was performed using one-way analysis of variance (ANOVA). P values less than 0.05 were considered statistically significant, and differences between samples within the groups were evaluated using a Student's t-test ($p < 0.05$). Differences in mechanical strength were determined by Student's test analysis ($p < 0.05$).

5.13 Electrospun Chitosan-PCL

Chitosan, a biodegradable, non-antigenic, and biocompatible natural polymer, bears the proxy structure of glycosaminoglycan (GAG), a major component of body native extracellular matrix (ECM). GAGs of the ECM are known to support enhanced cell attachment and proliferation and improve the material's cellular and tissue biocompatibilities [124,127-131]. However, chitosan is mechanically weak, and alone it is unable to retain its structural integrity with swelling in aqueous environments [132]. The complementary polymer employed in this study, PCL, is commonly found in tissue engineering applications due to its structural and mechanical stability [131,133]. PCL has limited cell affinity due primarily to its hydrophobicity and lack of surface cell recognition sites. The well-blended chitosan–PCL nanofibrous matrix, which integrates the favorable biological properties of chitosan and mechanical properties of PCL, is expected to significantly improve material properties, while providing a stable, nurturing environment for a broad array of biomedical applications.

As a model biomedical engineering application, we constructed a conduit from the nanofiber for potential nerve regeneration and studied mechanical and biological properties *in vitro*. We studied this particular application because it not only represents a significant clinical challenge, but also poses rigorous requirements in material's mechanical and biological properties among tissue engineering applications. Large-gap nerve damage that cannot be directly repaired with sutures has typically been treated using nerve autografts (Table 2), but this technique suffers from donor site morbidity inadequate return of function, aberrant regeneration, and shortage of donor tissue

[134,135]. An alternative approach is to use a nerve guide conduit serving both to promote nerve regeneration and to provide a pathway for nerve outgrowth. A number of polymeric nanofibers, including poly(caprolactone) (PCL), poly(lactic acid) (PLLA), poly(lactic-coglycolic acid) (PLGA), collagen and chitosan, are merging as promising candidates for nerve repair [136,137,138].

While the advances in nerve regeneration are encouraging, few of current nerve guide materials succeed in showing structural stability and pliability in physiological environments. Common problems confronted in application of artificial nerve guides as a result of unsatisfactory mechanical or biological properties of nerve conduits include structural collapse, material swelling, early resorption, and release of cytotoxic degradation products [139,140]. Nanofibrous structures generated by electrospinning can exhibit diverse fiber sizes, uniformity, integrity, and miscibility, depending on processing conditions, component ratios, and solvents used. We found that mixtures of chitosan in trifluoroacetic acid (TFA, 5wt**%**) and PCL in trifluoroethanol (TFE, 10wt**%**) at a component ratio range between 40:60 and 80:20 (chitosan:PCL) yielded solid, bead-free, uniform chitosan-PCL nanofibers, Figure 14. Changing these parameters and processing conditions provides flexibility to fine tune structural, mechanical, and biological properties suitable for specific applications.

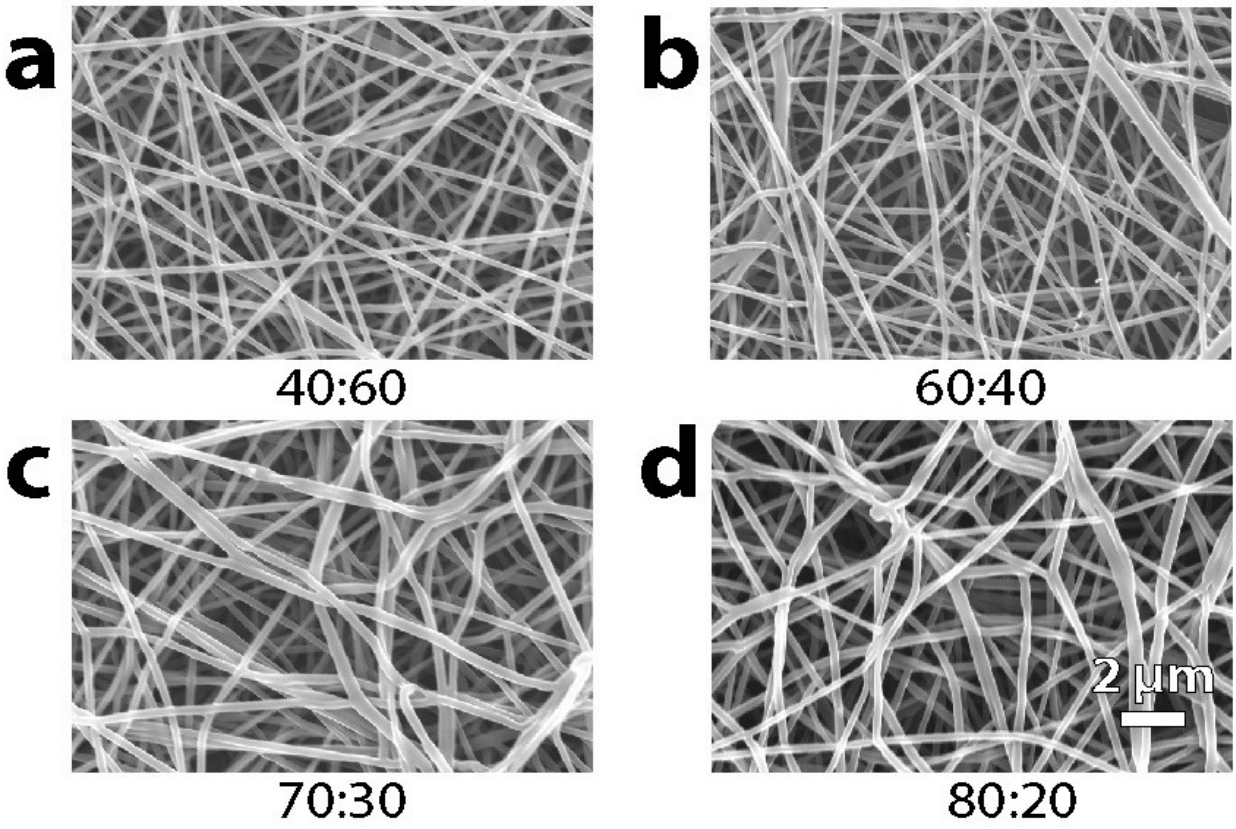

Figure 14. SEM micrographs of chitosan-PCL nanofibers prepared with different ratios of chitosan to PCL, showing the spinability of the solution in a wide range of chitosan-to-PCL ratios to produce bead-free nanofibers.

For the current nerve guide conduit focus, a blend solution ratio of 40:60 (chitosan:PCL; Fig. 15a) resulted in optimized fibrous structural and mechanical properties, and was used in subsequent experimentation. It should be noted that upon mixing chitosan/TFA solution with PCL/TFE solution, the PCL in the resulting chitosan-PCL solution is subjected to the acidic hydrolysis of PCL by TFA over time, requiring component mixing shortly prior to the electrospinning process.

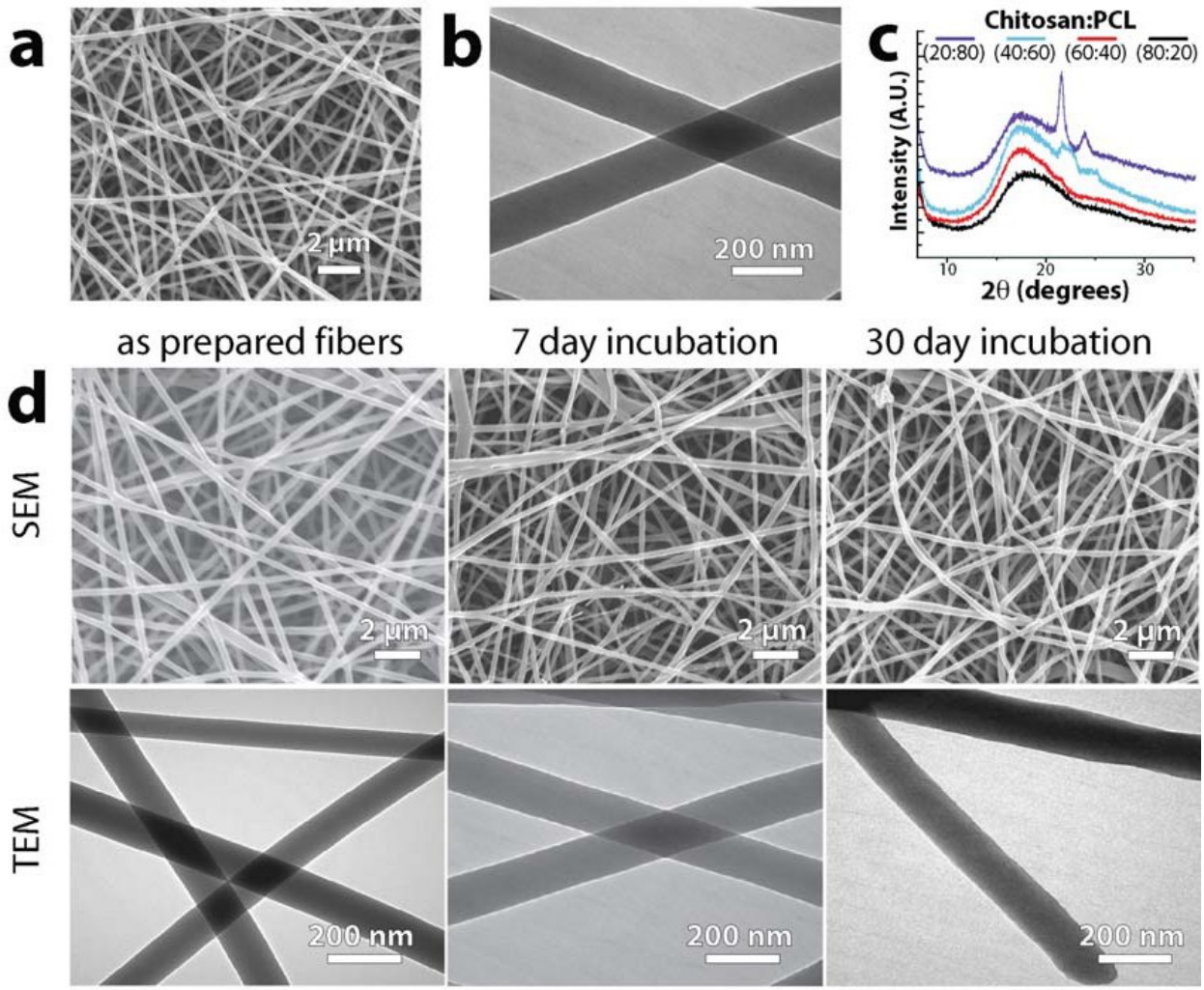

Figure 15. Structural properties and chemical stability of chitosan-PCL nanofibrous matrices. (a) SEM image of as-synthesized chitosan-PCL nanofibers (chitosan:PCL = 40:60) showing bead-free fiber morphology. (b) TEM micrograph of chitosan-PCL nanofibers showing no visible phase segregation or porosity. (c) WAXD patterns of blend nanofibers with varying component ratios of chitosan to PCL; the blend with a ratio of 40/60 or above showed significantly reduced crystallinity signifying increased miscibility. (d) SEM (upper row) and TEM (bottom row) images of bulk nanofiber materials after incubation with lysozyme-PBS solution for various durations revealing no apparent morphological change, phase segregation, or decomposition of the fiber constructs, demonstrating structural and chemical stability.

This is illustrated by the shear viscosity of chitosan-PCL solution (40:60) as a function of storage time after mixing chitosan/TFA solution with PCL/TFE solution at room

temperature (Figure 16a), and the morphology of electrospun products generated at different time points (Figure 16b). The grey box (Figure 16a) marks the time window in which the solution is spinnable producing bead-free, uniform nanofibrous structures.

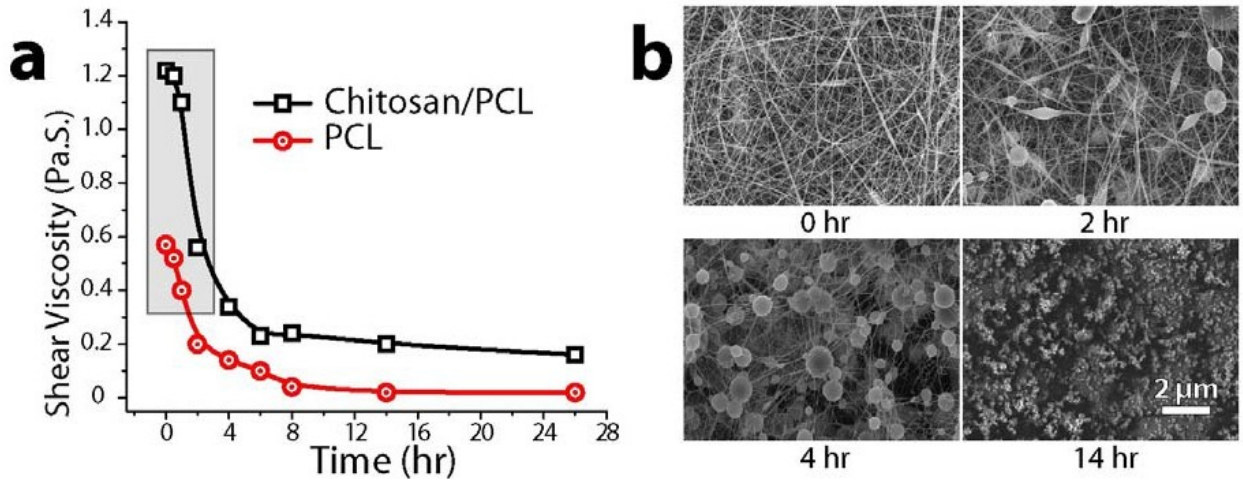

Figure 16. Spinability of chitosan-PCL solution over storage time. (a) Shear viscosity of chitosan-PCL solution (chitosan: PCL = 40:60) as a function of solution storage time at room temperature, showing that the solution viscosity decreases over time after solution preparation and there is a time window beyond which no fibrous structure can be obtained. (b) SEM images of chitosan-PCL nanofibers prepared with chitosan-PCL solutions at different storage times, showing that the viscosity and thus the storage time of the solution directly influence the spinability, and only solutions with short storage times yielded bead-free structures. Fiber morphology obtained from the solution with a storage time less than 5 min was marked as 0 hr.

Thus, in our experiments (flow rate = 0.95 ml h−1) the chitosan-PCL solution supply for electrospinning was replenished every half hour with freshly prepared chitosan-PCL solution. In industrial settings, the procedure can be easily automated by continuously mixing two solutions.

5.14 Physical Properties

The physical properties and biodegradation rate of polymer blends are strongly dependent upon their crystallinity, where phase inhomogeneities generally weaken the mechanical strengths of materials [133,141]. This is particularly true when the material's size dimension is reduced to the nanoscale. Miscible polymer blends can produce new materials with designated properties superseding those of their constituents. However, well-established miscible polymer blends are rare, and immiscible blend components are frequently identified by porous or phase-segregated structures.

Here, TEM, X-ray diffraction, and differential scanning calorimetry (DSC) thermograms were employed to assess the phase miscibility of chitosan-PCL nanofibers produced by electrospinning [142]. No component partitioning or porous structures were observed by TEM in chitosan-PCL nanofibers (Figure 4b), indicating good phase miscibility of the blend polymer. The diffraction pattern (Figure 4c) of the chitosan-PCL nanofibers acquired with wide-angle X-ray scattering (WAXS) shows that characteristic diffraction peaks of PCL (21.5° and 23.6°) were significantly weakened when the chitosan content in the nanofiber was increased to above 20wt%, suggesting decreased crystallinity of PCL with addition of chitosan and strong miscibility of chitosan and PCL with the lower crystallinity of a component material, indicating better miscibility of blended nanofibers [143]. Differential scanning calorimetry (DSC) thermograms of the prepared chitosan-PCL samples show shifts in glass transition (T_g) and endothermic temperatures but no additional peaks compared to the thermogram of a chitosan and PCL powder mixture (Figure 17a). This

indicates the formation of a new material phase (chitosan-PCL) and absence of additional phases, which further confirms the good miscibility of the chitosan and PCL.

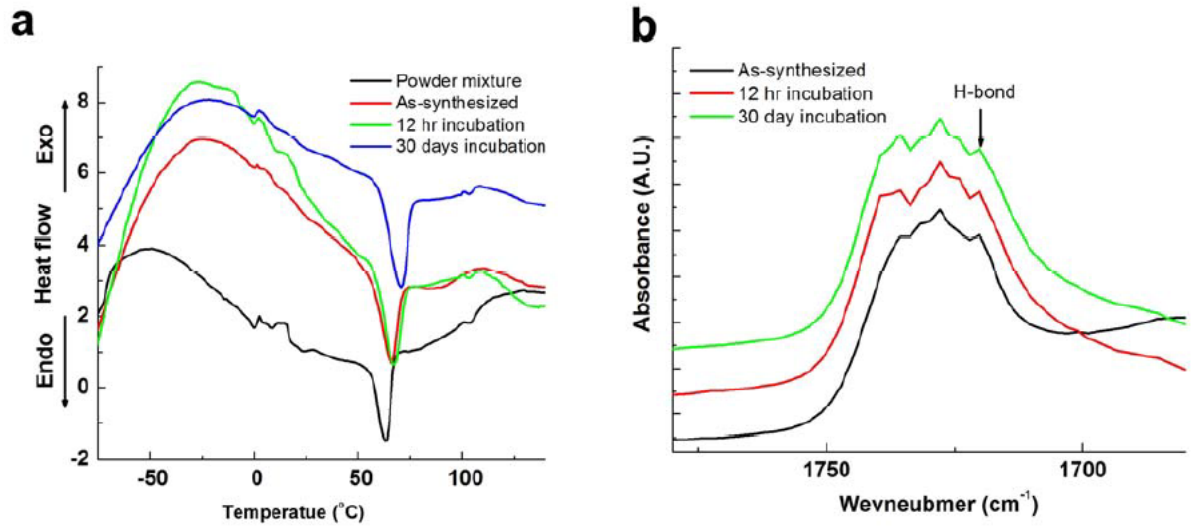

Figure 17. (a) DSC thermograms of blend nanofibers (chitosan:PCL = 40:60) acquired before nanofibers were incubated in a lysozyme-PBS mixture and at different time points after the incubation. A physical mixture of chitosan and PCL at the same ratio was shown as a reference. (b) FTIR spectra of as-synthesized chitosan-PCL nanofibers and the nanofibers incubated PBS/lysozme solutions for different times.

The preceding demonstration of good miscibility between chitosan and PCL in the electrospun nanofibers, which is otherwise difficult to achieve by alternative techniques such as film casting, freeze-drying, or melt blending, may be attributed to intermolecular hydrogen bonding between PCL carbonyl groups and chitosan amine groups (Figure 17b) and rapid solidification of the mixture solution of chitosan and PCL achieved by electrospinning preventing PCL aggregation.

Nanofibrous constructs are required to maintain their structural and mechanical integrity for biomedical applications such as tissue regeneration and regenerative medicine. As the body's aqueous environment and high lysozyme content are considered to be the primary sources of polymer degradation [144], chitosan-PCL fibrous matrices were tested *in vitro* at 37°C in a lysozyme-rich PBS solution for up to 1 month. No discernable changes to the structural integrity and chemistry of the nanofiber were identified by SEM/TEM (Figure 17d), DSC, and Fourier transform infrared spectroscopy (FTIR) analyses (Figure 17), indicating that the PCL-chitosan nanofiber has a slow degradation rate and is capable of retaining its integrity for prolonged time.

The cellular compatibility of chitosan-PCL nanofibers with neuronal cells for the model application (nerve regeneration) presented in this study was assessed by incubation with Schwann cells and PC12 cells. Schwann and PC12 cells are used in nerve regeneration to support and direct neurite processes, respectively. The cells were also cultured on PCL nanofibers and chitosan-PCL films for comparison. Schwann cells exhibited the most significant spreading on the chitosan-PCL fibers as indicated by the large, polar cell body, while the Schwann cells on the PCL nanofibers and chitosan-PCL film had smaller, spherical cell morphologies (Figure 18a, top panel).

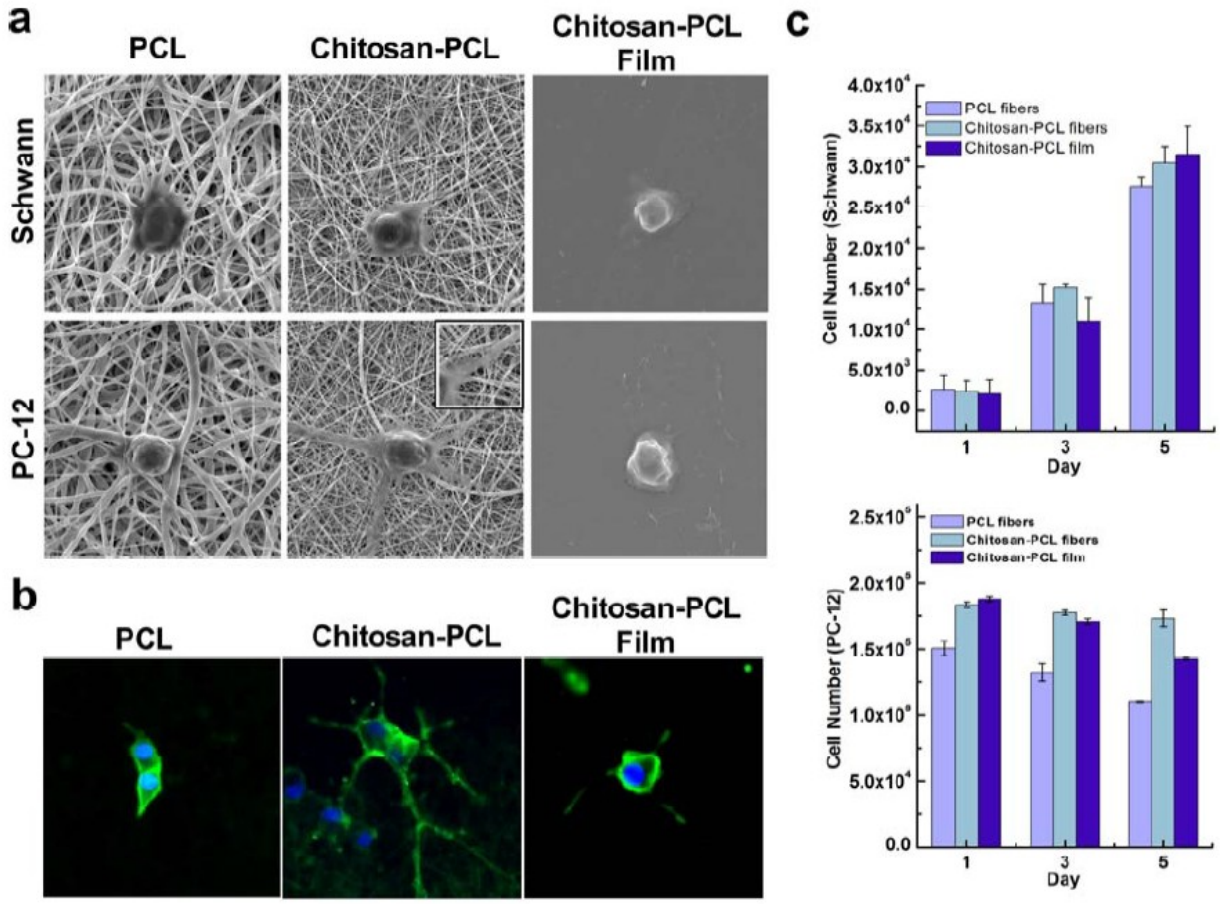

Figure 18. Adherence and proliferation of Schwann and PC12 cells on various materials. (a) SEM images of Schwann cells (top row) grown on various materials for 1 day and PC12 (bottom row) on various materials for 7 days. (b) Confocal images of PC12 cells on PCL nanofibers, chitosan-PCL nanofibers, and chitosan-PCL films, stained with an NGF receptor (green) antibody and DAPI (blue). (c) The number of Schwann cells (top) and PC12 cells (bottom) on various materials as a function of culture time, assessed by the alamar Blue assay. Values are means of three independent experiments; error bars correspond to standard error of mean.

The number of Schwann cells on all the materials increased similarly with time (Figure 18c, top), with no significant difference in Schwann cell attachment and proliferation among the tested materials. Similarly, PC12 cells exhibited the most significant spreading on chitosan-PCL nanofibers with more extended neuritis compared to those on the control

materials, which exhibited smaller and spherical cell bodies (Figure 18a, bottom panel). The neurite extension was better observed by immune-staining PC12 cells with antibody against nerve growth factor (NGF) receptor. Confocal fluorescence images showed a significantly higher degree of neurite expansion of PC12 cells on the chitosan-PCL nanofibers than on the control materials (Figure 18b), consistent with the SEM observation (Figure 18a). No apparent increase in PC12 cell number was observed on any substrate over time (Figure 18c, bottom), as expected, because PC12 cells in the presence of NGF are subjected to differentiation and do not proliferate. More PC12 cells were attached on chitosan-PCL nanofiber and film substrates than on PCL nanofibers at day one (1), indicating good cell adherence to chitosan-PCL materials, supporting the hypothesis that more active cell binding sites presented by chitosan would facilitate cell attachment. After continued incubation and replacement of the cell media through a period of 5 days, the number of PC12 cells on the chitosan-PCL nanofibers remained approximately the same, while the numbers of the cells on chitosan-PCL films decreased, indicating that the cells were more strongly adhered on nanofibrous structures. Overall, the chitosan-PCL nanofibers maintained the highest cell number throughout the 5-day study, exhibiting the best initial cell attachment and the strongest cell–material interaction. Nerve conduits were constructed by electrospinning the solution of chitosan and PCL onto a stainless steel rod collector of set diameter. Variations in length and diameter of the collector produced nanofibrous conduits with thicknesses ranging from 0.2–1.0 mm, with inner diameters of 1–5 mm, and lengths from 5–15 cm.

5.15 Mechanical Strength

Nerve conduits are required to be structurally stable while retaining sufficient mechanical strength and pliability for nerve regeneration. Conduits that are too rigid can break and induce scarring of neighboring tissue, while weak materials can be easily compressed, occluding the nerve growth pathway [145]. Mechanical properties of the conduit were assessed by tensile and compressive tests. The modulus for the chitosan-PCL conduit was found to be 110 ± 10 MPa and 103 ± 1.2 MPa at dry and wet states, respectively, and breaking strengths were 5.3 ± 0.5 (dry) and 2.9 ± 1.3 MPa (wet) (figure-19a). For comparison, two control nerve guides were also tested: a widely studied biomaterial for nerve guides, PLGA, prepared by the same electrospinning process, and a commercially available collagen conduit (Integra Life Sciences Corporation, Plainsboro, NJ). Both the PLGA and collagen conduits were much more susceptible to wetting than the chitosan-PCL conduit, and exhibited significant modulus decreases (9.3× and 5.2×, respectively) when wet, as compared to the chitosan-PCL conduit. All tested materials retained relatively similar breaking strengths. Pliability of the nanofibrous conduit was assessed with compressive load applied perpendicularly to the length of the tube. All tested materials retained relatively similar breaking strengths. Pliability of the nanofibrous conduit was assessed with compressive load applied perpendicularly to the length of the tube. Here, compressive strength of the wet chitosan-PCL conduit was 0.5 and 3.5 N at 10**%** and 50**%** compression, respectively (Figure 19b). Wet PLGA and collagen nanofibrous conduits showed much lower compressive strength with increasing deformation. Chitosan-PCL cast tubes of the same thickness as chitosan-PCL nanofibrous conduits

were tested to illustrate the difference in applicability between bulk and nanofibrous preparations.

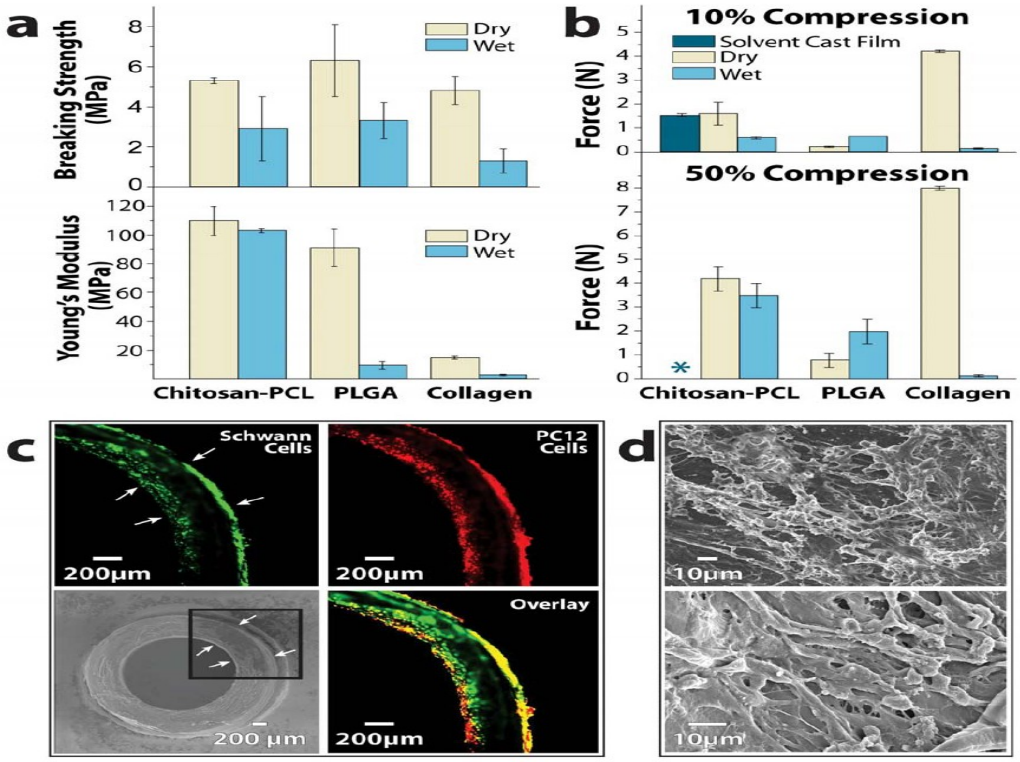

Figure 19. Mechanical properties and cellular compatibility of chitosan-PCL nanofibrous conduits. Tensile (a) and compressive (b) test results for tubular constructs at both dry and wet states for various nanofibrous conduits where PLGA and collagen nanofibrous conduits served for comparison. The solvent casting chitosan-PCL conduit in b was used to counter illustrate the superior mechanical properties of the nanofibrous structure. *Compressive testing of the solvent cast tube at 50% compression resulted in premature sample fracture. (c) Confocal microscopic images of Schwann cells (green) and PC12 cells (red) co-cultured on chitosan-PCL nanofibrous conduits, showing adherence of GFP-transfected Schwann (indicated by white arrows) and PC12 cells on the inner and outer surfaces of the conduit. (d) SEM micrographs of Schwann and PC12 co-cultured surface of the conduit at lower (top) and higher (bottom) magnifications showing neurite-like outgrowth of PC12 cells.

The cast tubes fractured after being mechanical compressed over 10% while nanofibrous conduits exhibited elastic deformation at elevated compression. In assessing mechanical

properties of nerve conduits, we believe that the data obtained with wet conduits more closely reflect *in vitro* and *in vivo* conditions compared to mechanical performance of dry materials. These differences can be substantial as we demonstrated here (Figures 19a and 19b). It is not surprising that a nerve guide that had been previously identified to be mechanically competent in dry state failed in service due to materials swelling, early resorption, or degradation. The interaction of chitosan-PCL conduits with neuronal cells and cell–cell interaction were assessed *in vitro* by co-culturing Schwann cells with PC12 cells. Green fluorescence protein (GFP) transfected Schwann cells seeded onto the conduit were allowed to attach and spread for 1 week prior to co-cultured with PC12 cells. After 11 days of co-culture in NGF-rich media, all cells were fixed and PC12 cells were immunochemically stained. Confocal microscopy identified two cell layers stained in green (Schwann cells) and red (PC12 cells) covering the inner and outer surfaces of the nerve conduits (Figure 6c), signifying that both Schwann and PC12 cells attached and proliferated well on the conduit. Samples recovered, fixed, and imaged by SEM showed extended neurite growth of the seeded cells, demonstrating that PC12 cells were functional and Schwann cells promoted the axon growth of PC12 cells (Figure-6d). Cells on the chitosan-PCL nanofiber mat were densely populated and the cell interactions with underlying nanofibers cannot be readily observed. To better reveal the cell–material interactions, Schwann and PC-12 cells were seeded on chitosan-PCL nanofibers at a lower concentration and co-cultured for a shorter period of time (7 days) for unobstructed observation at high SEM magnification (Figure 20). Schwann and PC cells were seen to adhere well on the chitosan-PCL nanofibers and exhibit their characteristic spindle and

round morphologies. These findings indicate that the bi-component nanofibers retained sufficient cellular compatibility for the preservation of neural functionality and growth.

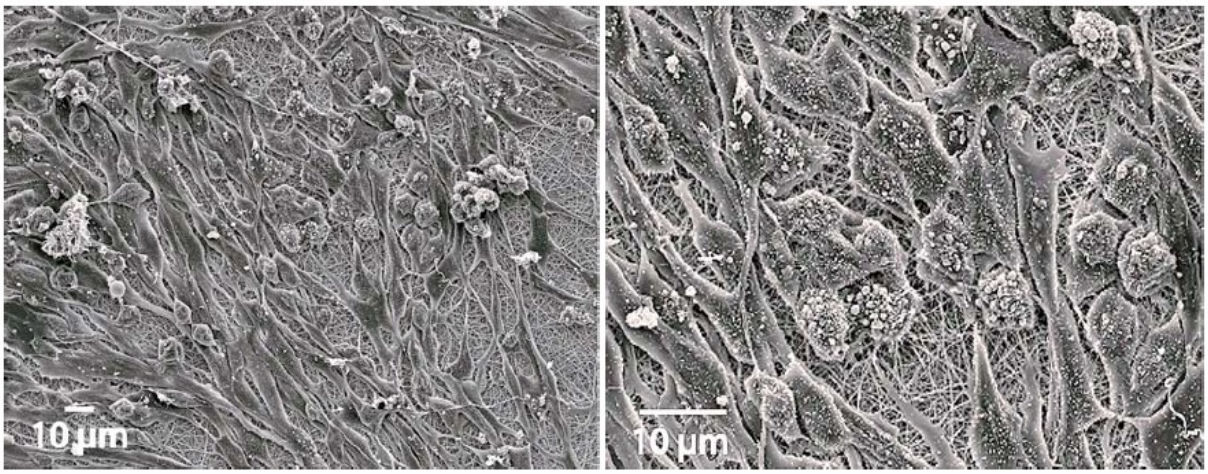

Figure 20. SEM micrographs of Schwann and PC12 cells co-cultured on chitosan-PCL nanofibers for 7 days at lower (left) and higher (right) magnifications.

5.16 Nerve Conduit Pilot Study

As a pilot study of *in vivo* application of chitosan-PCL nerve conduits, we implanted the nerve conduits in a critical-size sciatic nerve defect in rats for one month. The histological analyses of the explants showed regeneration of nerve fibers (Figure 21).

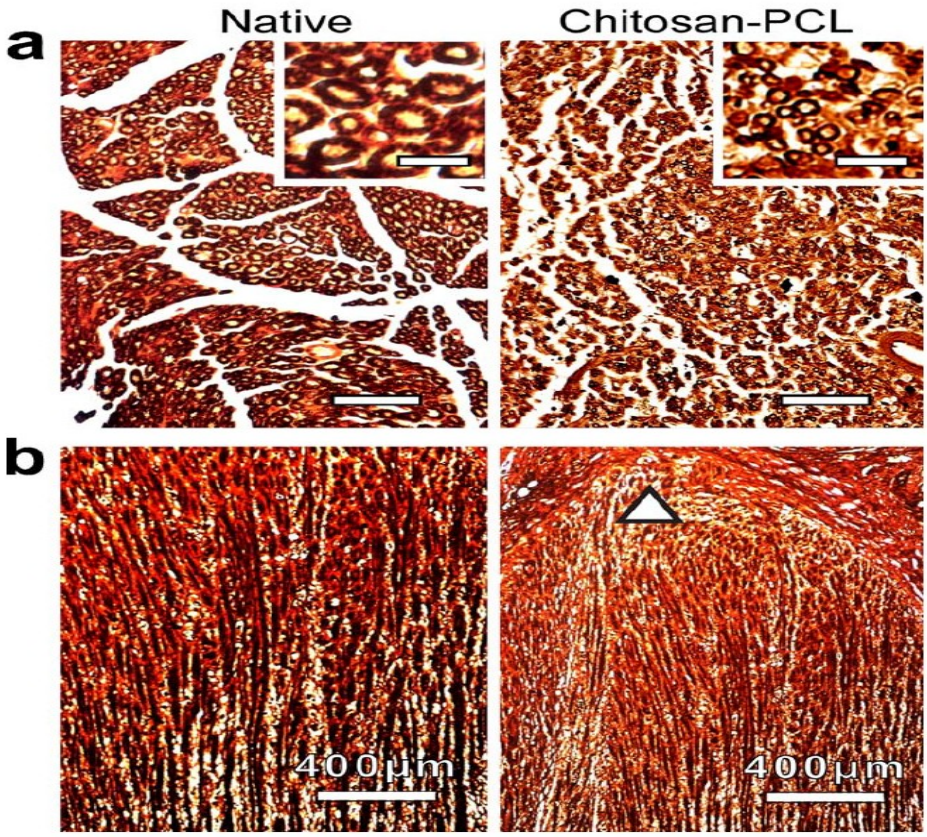

Figure 21. *In vivo* study of chitosan-PCL nanofibrous conduits for nerve regeneration in a rat sciatic defect model.

For comparison, the native nerves of rats were also analyzed. In Figure 22a, silver-stained cross-sections of native nerves (left) and new nerves formed in chitosan-PCL conduits (right). Scale bars are 100 μm for both panels, and 20 μm for the insets. Native nerve tissue was comprised of axon bundles separated by connective tissue (white regions). The lateral axon cross-section of the native nerve exhibited large, thick, dark brown circular staining due to the presence of myelinated sheaths around the axon extensions. In Figure 21b, silver-stained longitudinal sections of native nerve (left) and newly formed nerves in chitosan-PCL (right), displays axonal elongation at the nerve tip

(indicated by the white triangle) and the tip of its growing nerve inside the conduit. Comparatively then, normal distributions of axons are seen in the chitosan-PCL conduit, and sizes of the lateral axon cross-section of the extending axons within the chitosan-PCL conduits were smaller and stained brown, indicating the presence of young unmyelinated processes.

Chapter 6: Introduction to CES and Alignment of Fibers

Electrospinning solutions like polyvinylidene fluoride tetrafluoroethylene (PVDF-TeFE), and polyvinylidene fluoride (PVDF) at 70/30 weight ratio (Arkema Corporation) were dissolved in a mixture of di-methyl formamide (DMF or DMAc) and acetone at a weight ratio of 60/40, respectively. A range of concentrations (15–30wt**%**) were used to test the electrospinning setup. Also computer simulated was a CES model characterization determining field distribution. The analysis performed using a 2D version of ANSOFT® (ANSOFT, Philadelphia, PA) finite element analysis (FEA) high-voltage electrostatic software that determined electrostatic field distribution demonstrating that fiber could be collected in the gap between collector electrodes. The finite element model was analyzed with a point source high-voltage charge of $15kV_{dc}$ to $20kV_{dc}$ designed to point towards grounded collectors. The quality of nanofiber alignment was analyzed through fiber characterization in which fibers were sputter-coated with Au/Gd for 30 s at 18 mA and imaged with a scanning electron microscope (Joel JSM 7000F). Triplicate images of each sample were taken. Fast Fourier transform (FFT) was performed using ImageJ on a representative image to determine the fiber alignment. An image was uploaded into ImageJ (NIH, Bethesda, Maryland, USA, http://rsb.info.nih.gov/ij/) and an FFT analysis produced a pixel intensity image based on the frequency and direction of the fibers. The FFT images were normalized to a vertical access and radial pixels were counted using the oval prolife plug-in (authored by Bill O'Connell. http://rsbweb.nih.gov/ij/plugins/oval-profile.html).

Micron and nanoscale fibers are widely produced in the textile industry, and in energy, environmental, and biomaterial applications. Several methods such as phase separation, electrospinning, and textile technologies are used to fabricate fibers made of polymers, ceramics, and composite materials [147-153]. In textile technologies, the polymer solution or melt is commonly extruded through a spinneret that draws filaments with diameters ranging from a few microns to several hundred microns upon solidification [147,150,151]. However, it is difficult to form nanoscale fibers with this method. A nanofibrous network can be obtained from a polymer solution by using phase separation with several steps: gelation of the solution, exchange of the solvent with water, and then freeze-drying. Fibers can also be fabricated by methods of synthesis, drawing, template, and self-assembly [154-157]; however, these extensive processes inhibit large-scale production of fibers.

6.1 Centrifugal Electrospinning for the Production of Highly Aligned Long Nano- and Micron-Scale Fibers

Cell biology studies demonstrate that fiber orientation can induce cell guidance and pattering enabling targeting of the regeneration of specific complex tissues [175]. However, extensive manufacturing in a production environment of highly aligned long fibers has not been demonstrated by current laboratory and industry standard electrospinning techniques. Our Zhang lab developed a novel approach modifying traditional electrospinning method by using centrifugal polymer dispersion, hereafter called centrifugal electrospinning (CES). Grounded electrode bars or collector plates concentrically surround a regulated pressure-controlled rotating syringe-spinneret

connected to a high-voltage source via slip ring design. The inherent flexibility and robustness of our system allow control of important electrospinning parameters, including voltage, spinneret-collector separation distances feed-rate, and spinneret rotation speed — all for optimization of various polymer structures.

Electrospinning is a leading technology for the production of nanofibers in the laboratory environment due to its simplicity and versatility [158]. In the electrospinning process, a polymer solution is electrostatically charged within a needle or pipette tip. When an applied electric field gradient adequately overcomes surface tension of the polymer solution, a Taylor cone (Figure 1) forms. On further increase in the electrostatic charge the force created causes a polymer jet to form at the end of the Taylor cone and the jet undergoes an elongation process wherein the solvent begins to evaporate, thus producing a charged polymer fiber that is collected [175]. The advantages of electrospinning include easy processing conditions, application to various polymer systems, and ability to produce a wide range of polymer fiber diameters, including those in the nanoscale. However, due to bending and splitting instabilities [178] of the highly charged jet as observed by a whipping motion of the fiber, the fibers are deposited on a collector in the form of a nonwoven mat having random fiber orientations. Applications such as composite materials, electrochemical sensing, and scaffolds for tissue engineering often require highly ordered and well-aligned architectures that are impeded by the traditional electrospinning apparatus [159-163].

Several researchers have produced aligned polymeric nanofibers by using their unique methods [164-168]. Aligned fibers are typically produced by modification of the grounded

collectors. Fast-rotating cylindrical collectors and parallel gap electrodes are the most common electrospinning modifications for aligned fiber collection. In the cylindrical collector setup, the charged polymer jet is directed to a cylindrical collector, which is rotating at a fast speed, with a surface linear speed greater than 0.5 m/s [177]. Under optimized conditions, the polymer fiber attaches to the collector and is physically oriented circumferentially by chuck-type mandrel that rotates [169]. Unfortunately the fiber alignment is not perfect and is highly dependent on optimizing the collector electrode speeds while reducing deviations that cause misalignment or breaking of the fiber due to tension or necking of the fiber caused by the rotating collector. Improved rotating collectors have been produced by substituting the cylindrical collector with a tapered disk to concentrate the electrostatic field to disk edge; however, the result is a smaller, narrow aligned bundle [170].

Aligned fibers have also been obtained by introducing parallel electrode plates having air gap (space) between collector electrode halves. The collector-facing electrode edges in gap alter the electrostatic forces interacting with the incoming fibers [161]. The leading tip of a polymer fiber attaches to the first electrode plate edge due to electrostatic attraction, and the following portion of polymer fiber deposits on the other electrode edge. As a result, polymer fibers deposit perpendicularly to the electrode plate edges. The fiber alignment is innately dependent on the electrode air gap and accumulated electrostatic repulsion of deposited fibers ,which retain small residual charges. One method used a modified setup combining a rotating cylinder collector having parallel electrodes forming a rotating parallel wire drum. The group was able to produce long and wide nanofiber mats; however, they reported that the alignment diminished after 15 minutes when the mat

began to thicken, likely due to charge accumulation on mat [167]. Tests with another method demonstrated that due to non-perfect conductivity, nanofibers carried residual charge after deposition across the gap between two grounded electrodes and the residual charge affected incoming charged fiber, causing fiber misalignment [168]. Therefore, it is of interest to develop an electrospinning system in which the fiber alignment can be maintained to provide continuously aligned fiber in thick, long mats.

6.2 New CES (Centrifugal Electrospinning System)

To address electrospinning of aligned fiber issues we developed a centrifugal electrospinning system (CES) consisting of a variable speed rotating hub with attached syringe-spinneret, connected to high-voltage source via a slip ring design, and circumferentially surrounded by separate concentric electrodes (collectors) separated by gaps (Figure 23b). The hub was attached to a variable speed electric motor of 0–9000 rpm, and a wire from a high-voltage power supply (10–35KVdc) connected to spinneret needle. Electrically conductive aluminum panels were positioned concentric to the spinneret system and grounded to the power supply. The spinneret and collectors were housed in an electrically non-conductive large diameter cylindrical container made of high-density polyurethane. The housing has an adjustable diameter control for varying spinneret needle to collector distance and for radially adjusting the position of the electrodes (collectors) on their support to control solvent evaporation rate and deposition. This capability allowed for fiber production from a variety of polymer systems based on parameters such as solution viscosity, electric field strength, feed-rate, collector position, and rotating speed.

The new electrospinning system was designed to merge the effects of centrifugal force and parallel electrodes with electric field to enhance alignment. The developed CES uses centrifugal force and a Coriolis dragging effect on fiber to supplement the alignment and diminish the negative effect of surface charge and field strength. It offsets fiber mat repulsion by using centrifugal force on the ejected fibers simultaneously with an existing electrostatic gradient to produce fibers in aligned orientation. We developed a centrifugal electrospinning system (CES) to consist of a variable speed, rotating hub with a syringe-spinneret connected to a high-voltage source with spinneret circumferentially surrounded, at specified distances, by concentric electrodes each separated by gaps. The hub is attached to an electric motor of variable speed (0–9000 rpm), Figure 23. An insulated high-voltage electrical conductive wire from a high-voltage power supply (0–35 KV-dc) was connected to the needle on spinneret via an electrical slip ring mounted on hub. Electrically conductive aluminum panels or electrically conductive rods were positioned concentric to the spinneret system and grounded at power supply. The spinneret and collector were housed in a cylindrical container made of high-density poly-urethane that is electrically non-conductive. Furthermore, radial adjustment of electrode (collectors) position contributed to controlling solvent evaporation rate and deposition.

6.3 Electrostatic Field Analysis using ANSOFT®

A finite element software routine titled 2D-Maxwell by Ansoft® was used to determine the shape and field distribution of the electrostatic filed. The software modeler provides for structure emplacements and grid-size adjustment for higher calculation accuracy.

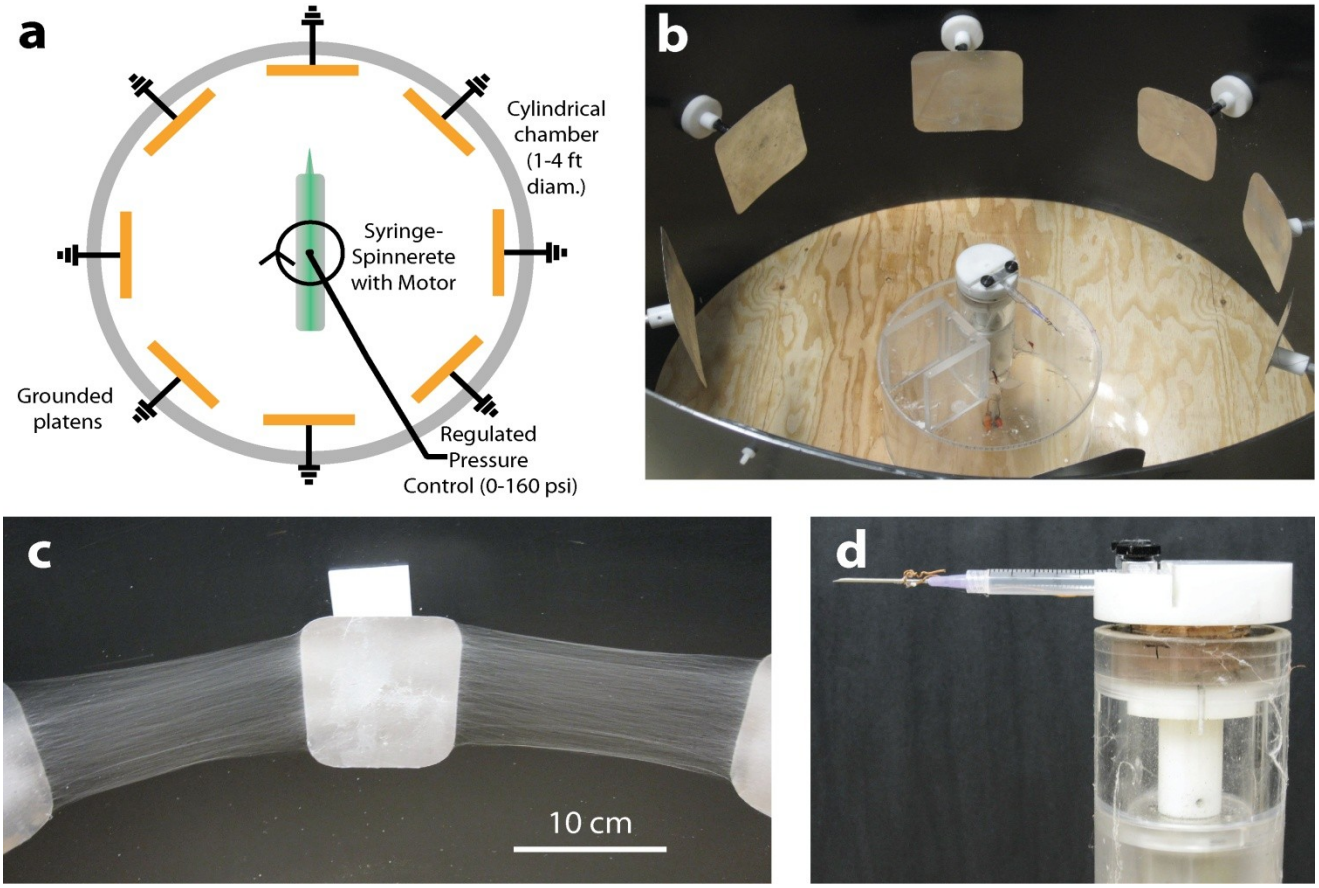

Figure 22. Centrifugal electrospinning setup; (a) schematic of the setup, (b) photograph of the setup, polyethylene oxide (PEO) fibers electrospun between grounded platens, and (d) photograph of the syringe-spinneret; note copper slip ring just below rotor top.

Its entire mathematical underpinning is based on Maxwell's equations to provide dependable information regarding field magnitudes, field orientations, and field potentials. The field distribution was performed on the model outlined in the Figure 23a schematic.

Although electric field strength is an important parameter to produce fibers from a Taylor cone, the field strength distribution is significant for fiber alignment. The arrangement of the high-voltage stainless steel needle spinneret rotating about its axis can be modeled as a charged disc at the center of a system. The electric field lines normal to the periphery of

disc will split in the vicinity of the collectors into two fractions pointing towards the opposite edges of the gap [171]. The equipotential lines form concentrically to the plane of a disc, and the lines in the vicinity of the collectors sink into the gap as observed in parallel plates with a gap arrangement (Figure 24). The electrostatic field orientation promotes fiber alignment parallel to collector front surface, allowing aligned fibers to bridge the gap between collector plates.

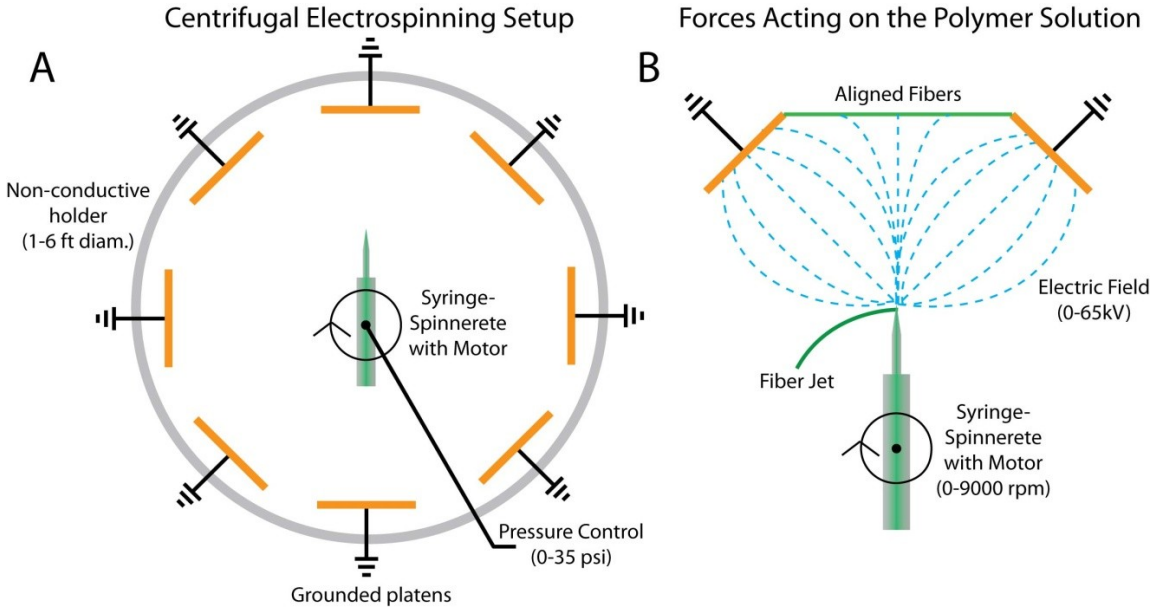

Figure 23. (a) Schematic illustration of centrifugal electrospinning setup; (b) electrical field distribution with large gap; (c) and electric field distribution.

The finite element analysis approach used a detailed point-to-point mathematical triangular grid technique, Figures 24 through 27, to determine field vector directions and gradient distribution, which allowed determination of an optimal gap width between collector bars where aligned fiber was deposited. As illustrated in Figure 23b, a wide collector gap lessens electrostatic field concentration and was not as strong as when the collector gap distance was reduced and compressed electric field lines that enhanced field strength.

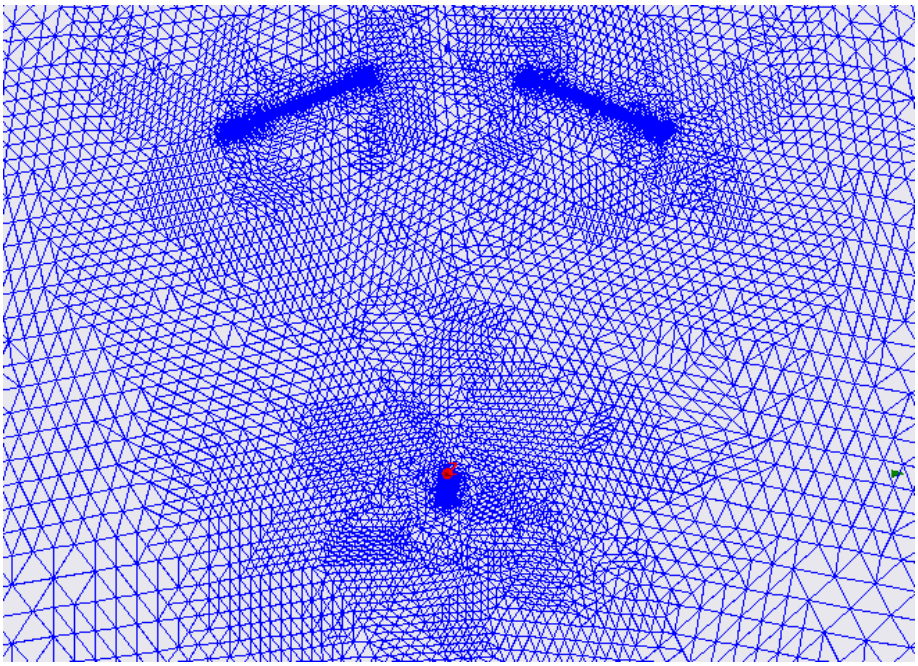

Figure 24. Triangular mesh automatically generated by Ansoft®.

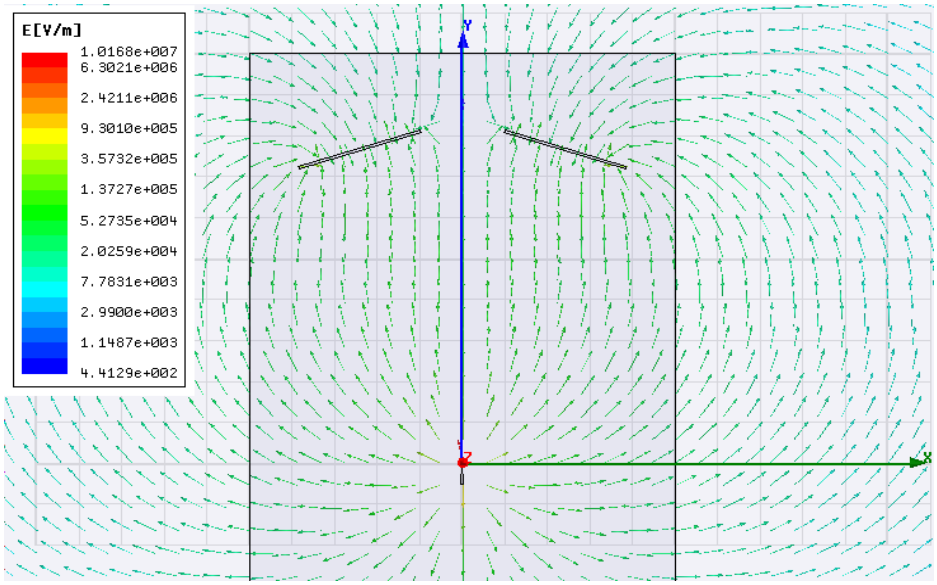

Figure 25. Electric vector distribution using 20kv source. Images illustrate field distribution between high-voltage source and grounded collector electrodes allowing aligned fiber accumulation in gap.

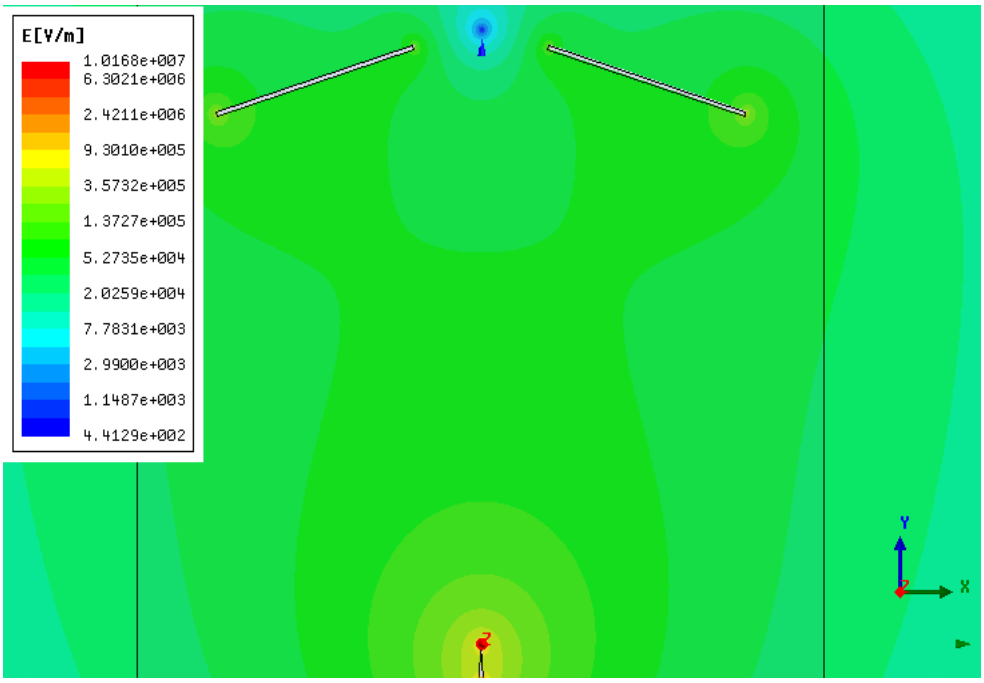

Figure 26. Electric–magnitude distribution of Figure 6 with 20kv source.

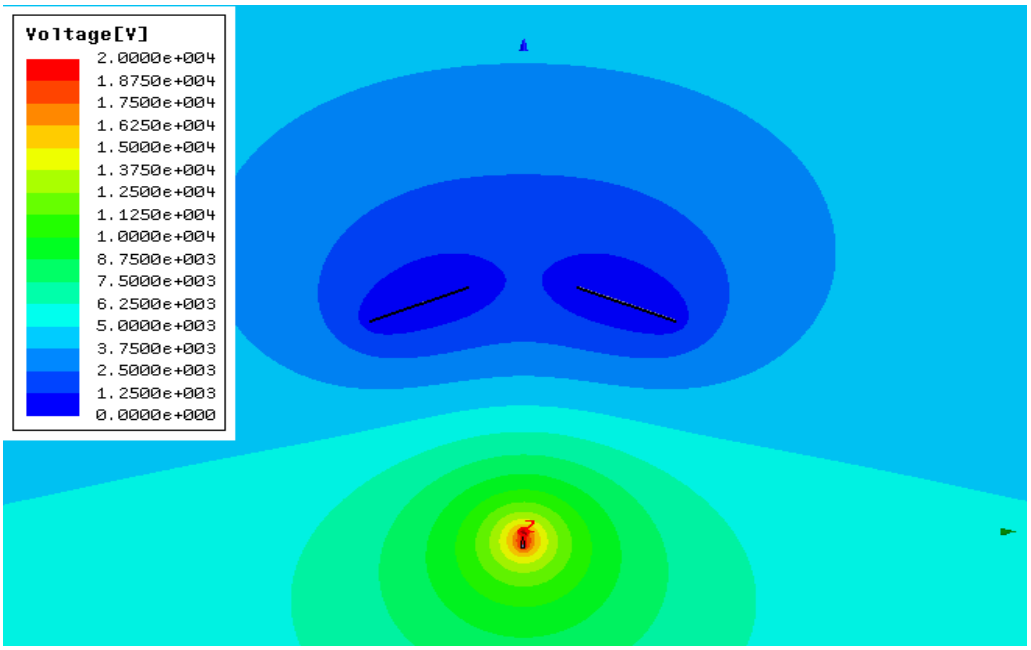

Figure 27. Voltage distribution with 20kv source.

In addition to the electrostatic field gradient providing forced solution ejection from spinneret and transporting nanofibers to collector bars, two additional effects created by a rotating spinneret are also simultaneously involved — centrifugal and Coriolis effect. These forces work in sequence with electrostatic field gradient to provide a tertiary force effect on each elemental segment of the fiber's length, from the creation at the spinneret needle tip to grounding between platens. A centrifugal force is provided by spinneret rotation where, $F_{Radial}=mr\omega^2$, where m is solution mass per time, r the radius from spinneret hub axis of rotation to needle tip, and angular rotational velocity ω^2, while the Coriolis force [A-de] is governed by $-2m\omega v$, where $v = rv_{radial} - r'v_{tangential}$, m mass of fiber jet and both added to an electrostatic force (ESF) potential. The ESF is governed by $F = k\ q_1\ q_2\ /r^2 = q_1\ q_2/4\ \pi\ \varepsilon_0\ r^2$, where ε_0 is $8.854187817 \times 10^{-12}$ F/m, and q represents respective charges in Coulombs [175], which is defined as charge transported by a steady current of one ampere in one second.

By characterizing the effects acting on polymer fibers we were able to control nanofiber alignment and size. The adjustability of the CES machine allowed for fiber formation based on controlling various parameters associated with effective electrospinning, such as solution parameters (solvent, polymer concentration, molecular weight, viscosity), spinneret rotating speed, applied voltage (electric field strength), polymer-feed rate, spinneret-collector distance, and collector gap widths.

In electrospinning, major parameters affecting fiber formation and diameter include polymer concentration, viscosity, and electric field strength. During the electrospinning process, significant forces acting on the electrified fluid jet stream including electrostatic

repulsion, collector distance, gravitational force, viscoelastic stress, solution surface tension, solution conductivity, and electric field strength, affect the ability to preferentially align the fibers [171]. A particular force that impedes alignment of fibers is residual charge on the deposited fibers making up a mat. This issue cannot be addressed by increasing electric field strength, which simply amplifies the amount of fiber residual charge [168]. It is known that a liquid jet, under electrostatic force, accelerates towards a grounded collector evaporating solvent while undergoing considerable stretching as liquid surface tension tends to hold liquid jet together, producing continuous, ultra-thin fibers of polymer [172,173]. In addition, the more time that liquid jet is pulled circumferentially around by hub rotation in the space between spinneret and collector, the more stretching occurs, further reducing fiber diameter.

6.4 Centrifugal Force Effects on Fiber

Another effect derived from the CES upon ejecting polymer solution from rotating spinneret hub is the Coriolis effect [183]. Rotating coordinate systems, also called non-inertial frame, can give rise to the Coriolis effect which is a pseudo force *(inertial force),* but its effect is still real and affects continuous fiber direction with time. A fixed inertial frame of reference, or inertial reference frames, all moving with constant velocity with respect to each other, are referred to as non-accelerated or non-rotated providing frames of reference. Physical Newtonian law takes the same form as it does in any other inertial reference frame, but the measured values of physical quantities may not be correct. By contrast, non-inertial reference frames, which are accelerating and/or rotating relative to inertia reference frames, respond only to laws of dynamics dependent upon the particular

inertial frame referenced, requiring that usual physical forces be supplemented by what is called pseudo forces even though these forces produce real effects. For example, when going around a sharp turn in a car, boat, airplane, one slides away from center of rotation. Due to the Coriolis effect, polymer nanofibers travel in a planar curvilinear path instead of straight path normal to circular periphery. Traveling towards the collector plate in a spiral (Figure 29c and 29d), the liquid jet in the form of nanofiber traverses a greater distance, providing additional time for solvent evaporation.

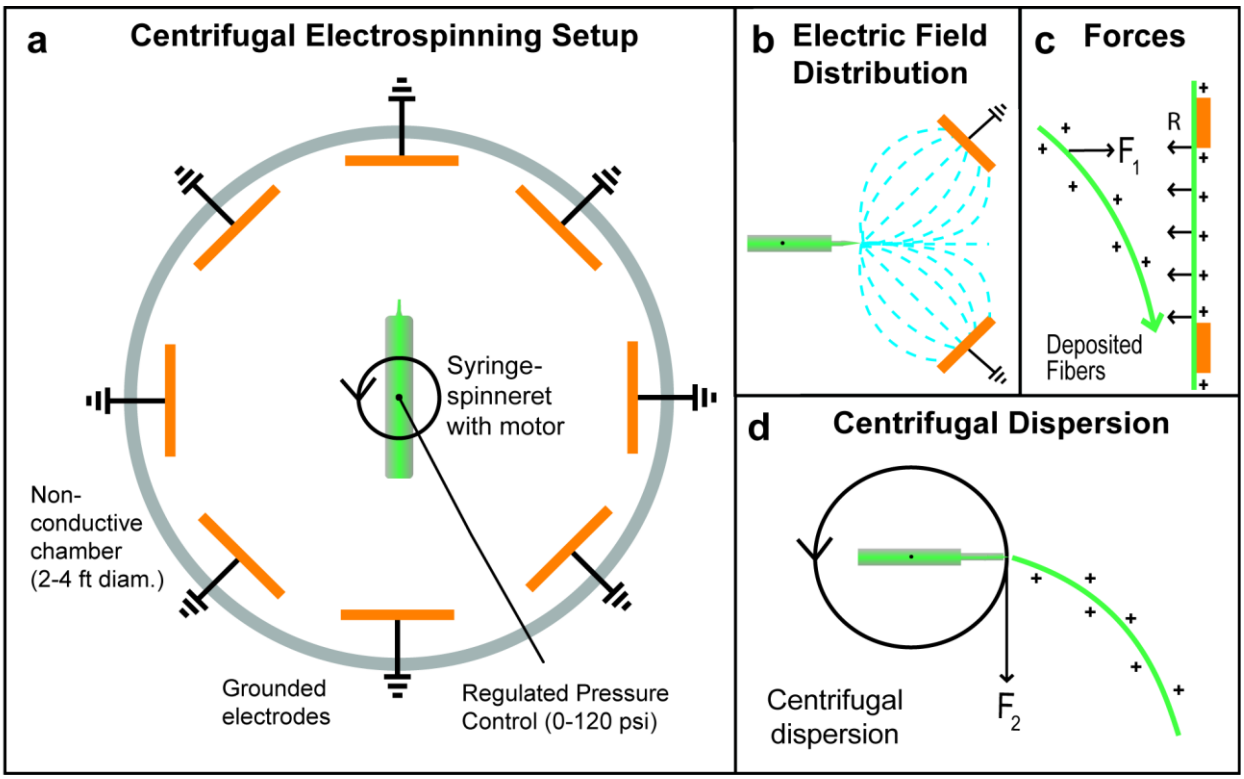

Figure 28. Schematic illustration of the (a) centrifugal electrospinning (CE) setup; (b) electric field distribution; (c) repulsive charge forces; (d) centrifugal and Coriolis effect.

Finer nanofibers require small-gauge needles and reduced distance between the spinneret and collector as solvent evaporates quickly due to higher surface area to volume ratio. Highly viscous solutions through smaller gauge syringe needles also produce nanofibers, but smaller gauge syringe needles used with high-viscosity polymers require greater forces to create a Taylor cone and sustain proper polymer feed rate. CES design is able to apply a controlled, forced feed rate using by polymer weight itself without plunger inserted in syringe or a lead bar weight inserted inside syringe pushing on plunger to create additional radial force as spinneret hub rotates. Fast spinneret rotation can be problematic, and to offset air turbulence a specially designed polymer swivel connector is attached atop spinneret hub, allowing an air hose attachment to remain stationary while hub spins. For solutions having higher polymer concentrations than typically used in electrospinning, inducing regulated air pressure up to 100 psi pushing on syringe plunger allows a Taylor cone to form in conjunction with electrostatic field at slow hub rotation. As a result we are able to electrospin a wide variety of polymer types and concentrations at low rotational speeds; force provided by air pressure offsets fast rotation centrifugal force normally required to effectively force high-viscous solution through spinneret needle.

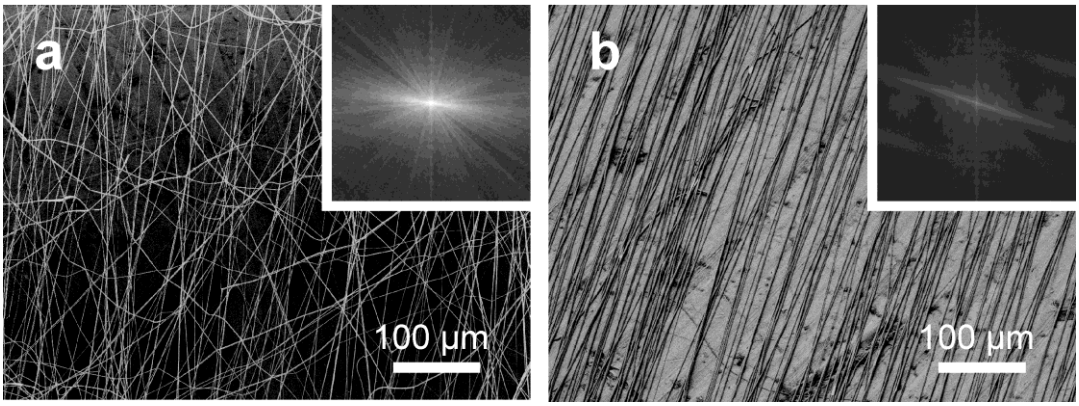

Figure 29. PVDF-Tetra-FE electrospun between a 4=cm gap with a (a) stationary or (b) rotating (150 rpm) spinneret. Insets are FFT analysis of the fiber alignment.

6.5 Experimental Setup

Solution parameters: The solvent type and polymer have a dramatic effect on the electrospinning process. The solvent volatility directly controls the fiber drying mechanism and the formation of fibers. In systems with highly volatile solvents or co-solvents, porous fiber or fibers with skins can form. Additionally, solution conductivity in that solution with a high conductivity will have a greater surface charge, which will cause greater electrostatic pull to the grounds, thus decreasing fiber diameter. However, with very high conductivities electrospinning is unstable leading to a broad range of fiber distributions [173].

The solution is highly dependent on the polymer type and molecular weight in that sufficient polymer chain entanglement is often necessary to produce continuous fibers [173]. Furthermore, the polymer concentration directly affects the surface tension, which effects the Taylor cone formation and the polymer flow rate.

6.5.1 Spinneret rotating speed: In the traditional rotating drum step for the production of aligned fibers, polymer is electrospun towards a fast rotating drum, whereby the fibers are physically aligned circumferentially when deposited. In this CES setup, a rotational polymer spinneret was used to increase alignment by physically directing fiber deposition. In addition to the electrostatic interactions induced by the electric field gradient, two additional forces created by a rotating spinneret are also simultaneously involved, centrifugal and Coriolis effect. These forces work simultaneously with the electric field gradient to provide a tertiary force effect increasing alignment between the separated collector plates by dragging fiber circumferentially in a logarithmic arc (Figure 29d).

6.5.2 Applied voltage: In electrospinning processes the electric field strength between spinneret and collector electrodes must exceed a certain threshold value associated with solution composition in order to form a polymer jet from spinneret.

6.5.3 Taylor cone: As a result, the voltage applied during electrospinning has the greatest impact on the formation of continuous uniform fibers, and in particular nanofibers. Insufficient voltage and electric field strength can prevent the formation of continuous fibers or produce beaded fibers. In addition, if the electric field strength is too great, beaded fibers may also form [166]. As a result, the applied voltage needs to be optimized for a particular polymer/solvent system to form uniform, continuous fibers. The proposed CES was supplied with a variable voltage supply of 6–30 kVdc, which allowed for control of optimizing the voltage range for fiber production.

6.5.4 Polymer-feed rate: To ensure continuous fiber formation, the polymer feed rate through the capillary (spinneret/needle) needs to be sufficient to maintain the Taylor cone formation. Generally, increasing the polymer feed rate has little effect on the fiber diameter. However, if the feed rate is too fast, beaded fibers or ribbons could form due to insufficient drying of the fiber before deposition. Most electrospinning systems employ gravity-feed or syringe-pump fed polymer solutions to control the feed rate. The proposed CES employed a pressure-induced (0–100 psi) feed rate, allowing for the flow of a wide variety of polymer solutions, including those with very high viscosity solutions.

6.5.5 Spinneret-ground distance: Generally with increasing spinneret to fiber collector distance, the fiber diameter decreases due to elongation of the fiber caused by electrostatic tensional pull to the ground. The distance needs to be optimized for individual polymer/solvent systems because a short distance could result in beaded fused fibers due to insufficient drying, or long distance could result in insufficient collection of the fibers [174]. For the CES system, the grounded collector electrode plates were radially positioned around the spinneret and the separation distance could be varied between 5 and 35 cm.

6.5.6 Gap distance: In this CES setup a parallel gap electrode was used to promote aligned fibers. As shown in Figures 2b and 4, the electrostatic field lines split between the two collectors, directing the electrostatic field lies to the nearest collector. As a result, the electrostatic field distribution between electrodes affects the resulting fiber alignment. As the highly positive fiber deposits on one electrode, the other positive trailing portion of the

fiber deposits across the electrode, thereby aligning the fibers. The gap width and its effect on electrostatic field distribution therefore directly correlate with electric field strength across collector air gap, with smaller gap widths producing stronger electrostatic forces, resulting in greater fiber alignment.

6.6 Effect of Polymer Concentration

Based on the optimized rotational speed for the 20wt% PVDF (200 rpm), the effect of the polymer concentration was examined in an effort to optimize the fiber diameter and uniformity. To this end, PVDF solutions with 20–27.5wt% PVDF in DMF/acetone were electrospun. As shown in Figure 31, the fiber diameter and non-uniformity increased as the polymer concentration increased. Specifically, the 20 in Figure 31a and 22.5wt% PVDF in Figure 31b solutions produced the smallest fibers with the narrowest fiber diameter distributions, as shown in Figure 9e. However, at high polymer concentrations of 25 and 27.5wt%, the average fiber diameter increased to 469 nm and 567 nm with extremely large fibers of 1230 nm and 1670 nm, respectively. The solution concentration and viscosity have a direct effect on the electrospinning process, which prevents sufficient solvent evaporation and jet thinning, and results in larger fiber diameters [161]. Particularly, higher solution viscosities cause a greater interaction among polymer molecules and the influence of charges stretching the solution tended to spread the solvent molecules over entangled polymer molecules, reducing fiber beading [164]. As a result, the optimal PVDF concentration range for the 200 rpm wt% polymer solution was 20–22.5wt% PVDF in DMF/acetone.

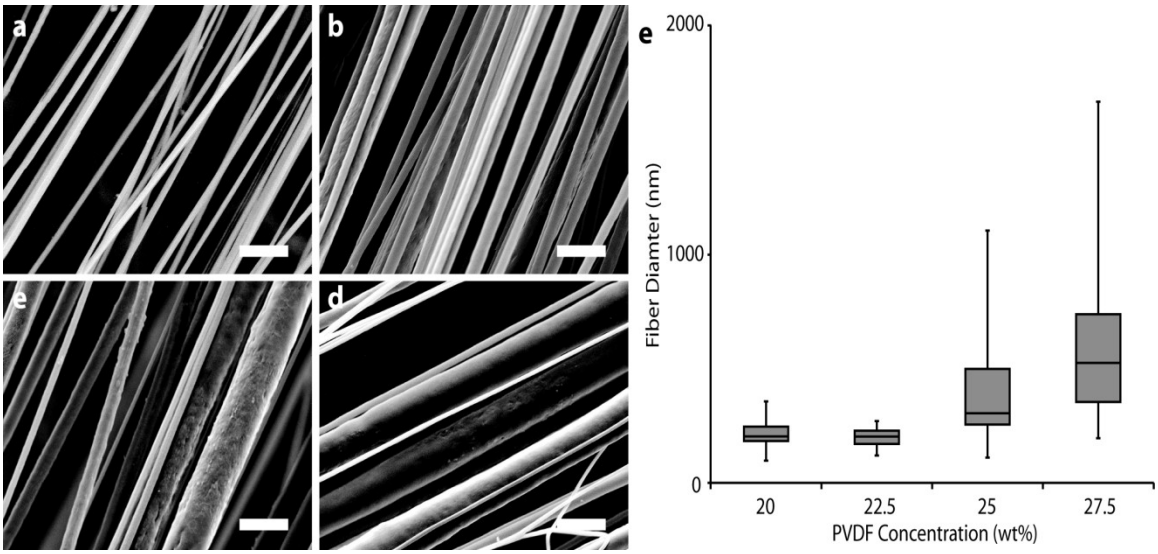

Figure 30. SEM images of fibers produced from (a) 20, (b) 22.5, (c) 25 and, (d) 27.5 wt% PVDF in DMF/acetone. The scale bars represent 2 μm. The PVDF solutions were electrospun at 12 kV and 200 rpm and the fibers were removed from between a one-inch collector–collector gap. The fiber diameter distribution (e) was plotted with the median diameter represented by the interior horizontal line. The upper and lower horizontals designate the upper and lower quartiles. The error bars indicate the largest and smallest fiber diameter measured within a dataset of 50 fibers.

Our CES system is inherently flexible and therefore each individual parameter can be altered to not only adjust fiber uniformity and diameter, but also dispense various types of solutions for electrospinning. These same trends will presumably exist for the same PVDF/solvent mixtures, to allow for optimal aligned nanofiber ranges, depending on different rotational speeds, gap distances, and polymer concentration. To further illustrate the ability to produce nanofibers, a 70/30wt% PVDF-Tetra-FE was electrospun at 225 RPM, 30-gauge needle, 15kV$_{dc}$, 20-cm spinneret-ground, 2-cm gap, 8 psi. As shown in Figure 32a and 32b, the PVDF-Tetra-FE fiber was highly aligned with fiber diameters of approximately 250 nm. Due to the inherent flexibility of the system, the fiber diameter

could be theoretically controlled by adjusting the solution viscosity, operating voltages, spinneret-ground distance, electrode gap distances, and spinneret rotating speed.

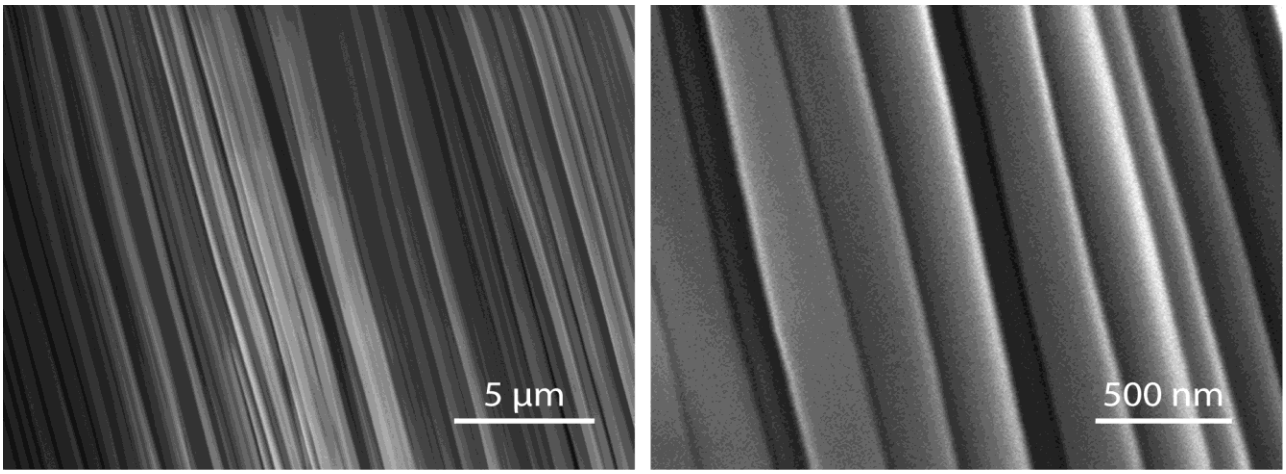

Figure 31a. Highly aligned PVDF fibers using the CE setup with a 20wt% solution at 15kV and 225 rpm.

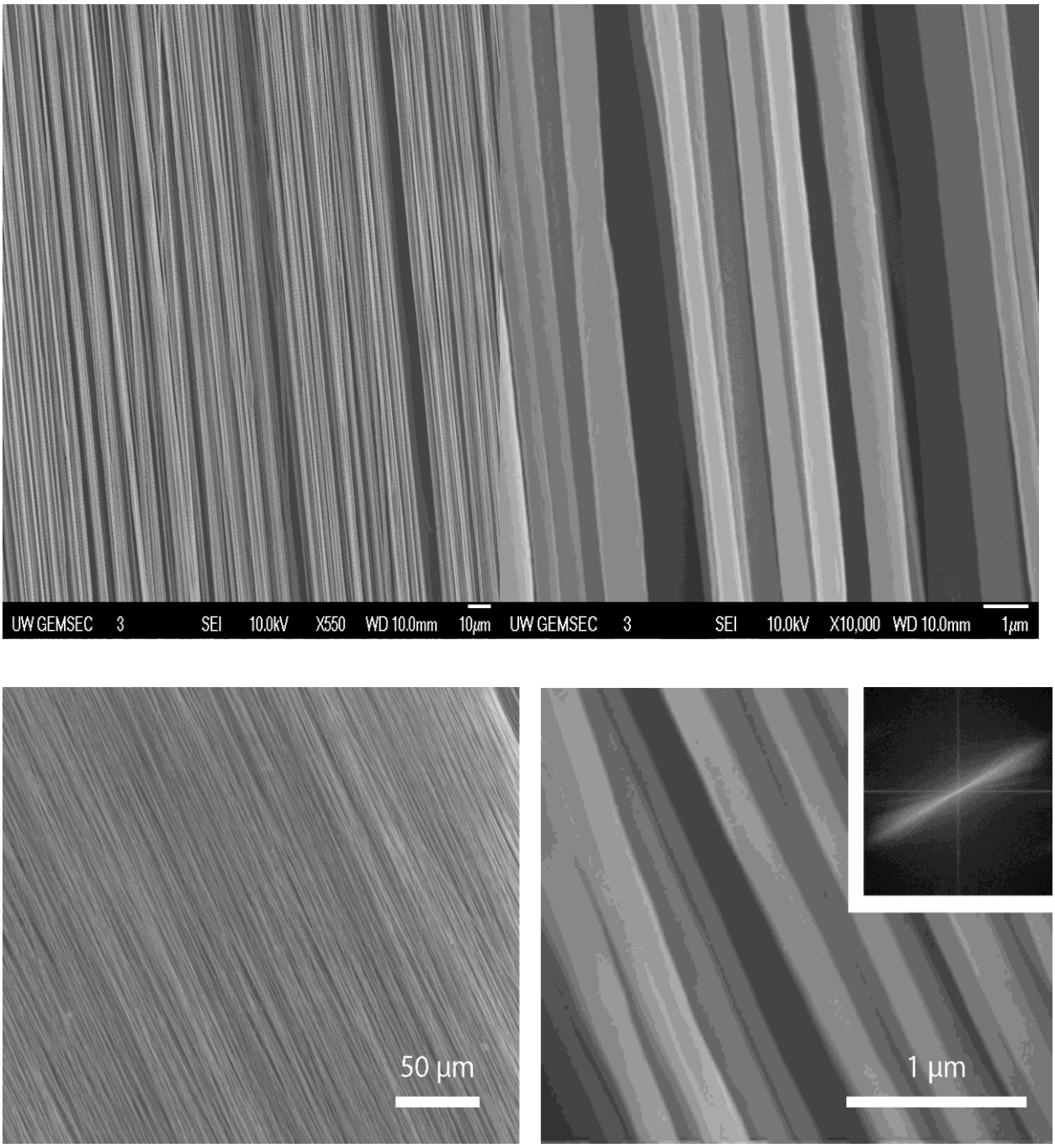

Figure 31b. PVDF nanofibers and FFT analysis of the fiber alignment. PVDF fibers were fabricated using 70wt% PVDF-30wt% TeFE with 60wt% DMF and 40wt% acetone. Second composition was 70wt% PVDF-30wt% TeFE with 60wt% DMAc and 40wt% Acetone. Both cases were electrospun at 12KVdc and 425 rpm.

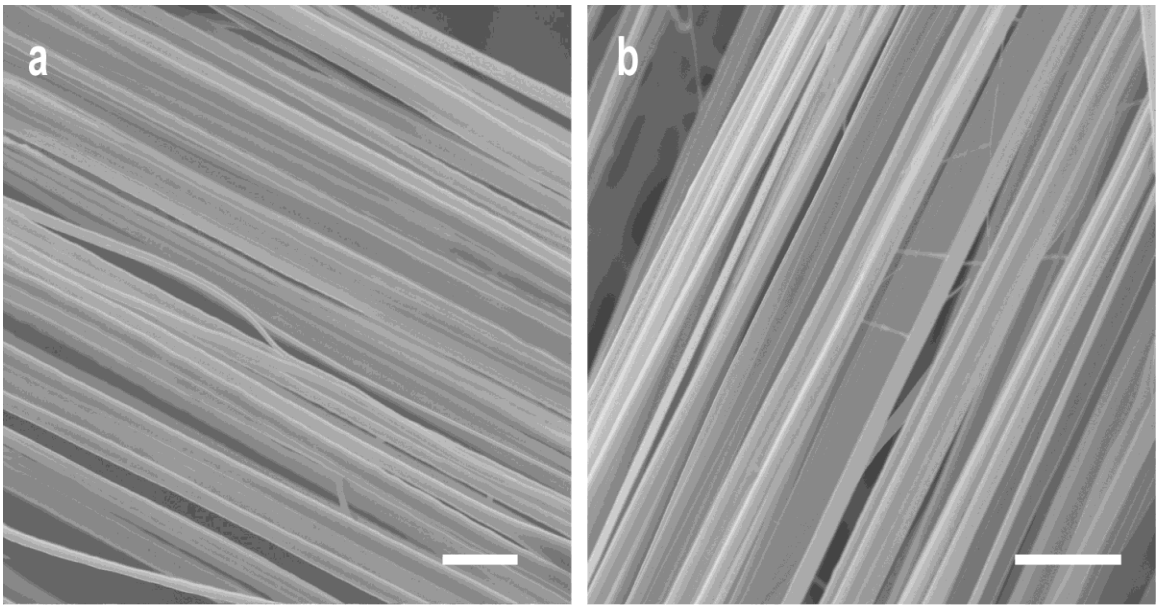

Figure 31c. Aligned (a) PEO and (b) chitosan-based fibers prepared on the CES. The scale bars represent 2 μm. PEO fibers were produced using 22KV$_{dc}$, 300 rpm, and a 20-cm spinneret-electrode distance. Chitosan-based fibers were produced from using 22KV$_{dc}$, 300 rpm, and a 20-cm spinneret-electrode distance.

As shown in Figure 32a, fibers were deposited across a 13-cm gap with macroscopic alignment, thereby demonstrating that we can produce highly aligned, long mats and FFT analyzed as shown in Figures 32b and 32c. The resulting samples were collected and analyzed with SEM. Figures 33a and 33b further demonstrate robustness of the novel CES aligned fiber spinner where different polymers used in bioengineering applications were also aligned spun.

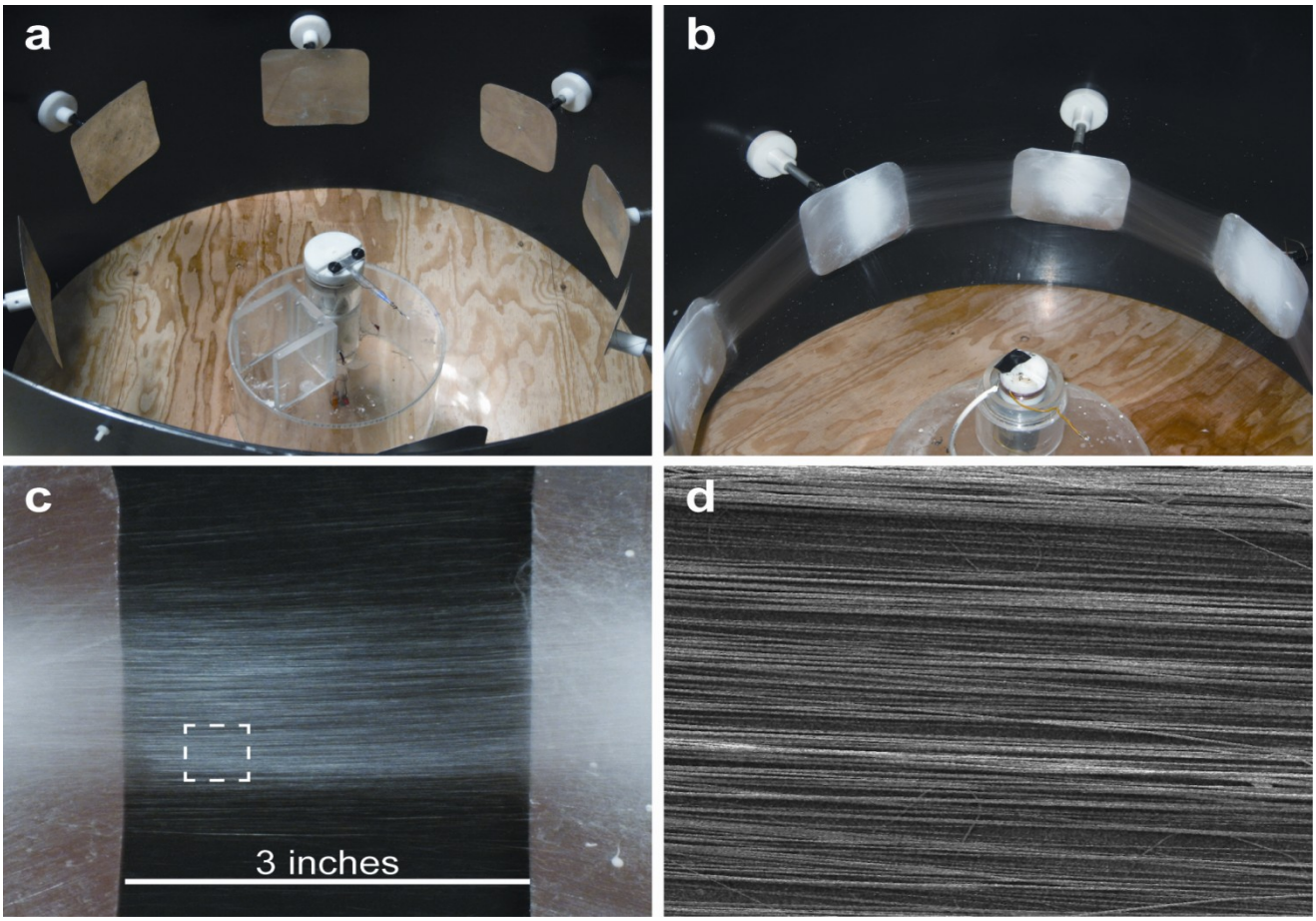

Figure 32. (a) and (b) CES electrospinner developed in Zhang lab. (c) Thin mat consisting of aligned PVDF nanofibers produced with a 70/30wt% PVDF-TeFE solution, 20-cm spinneret E-field to ground distance, $10KV_{dc}$ and 13-cm plate separation. (d) Enlarged image of (c).

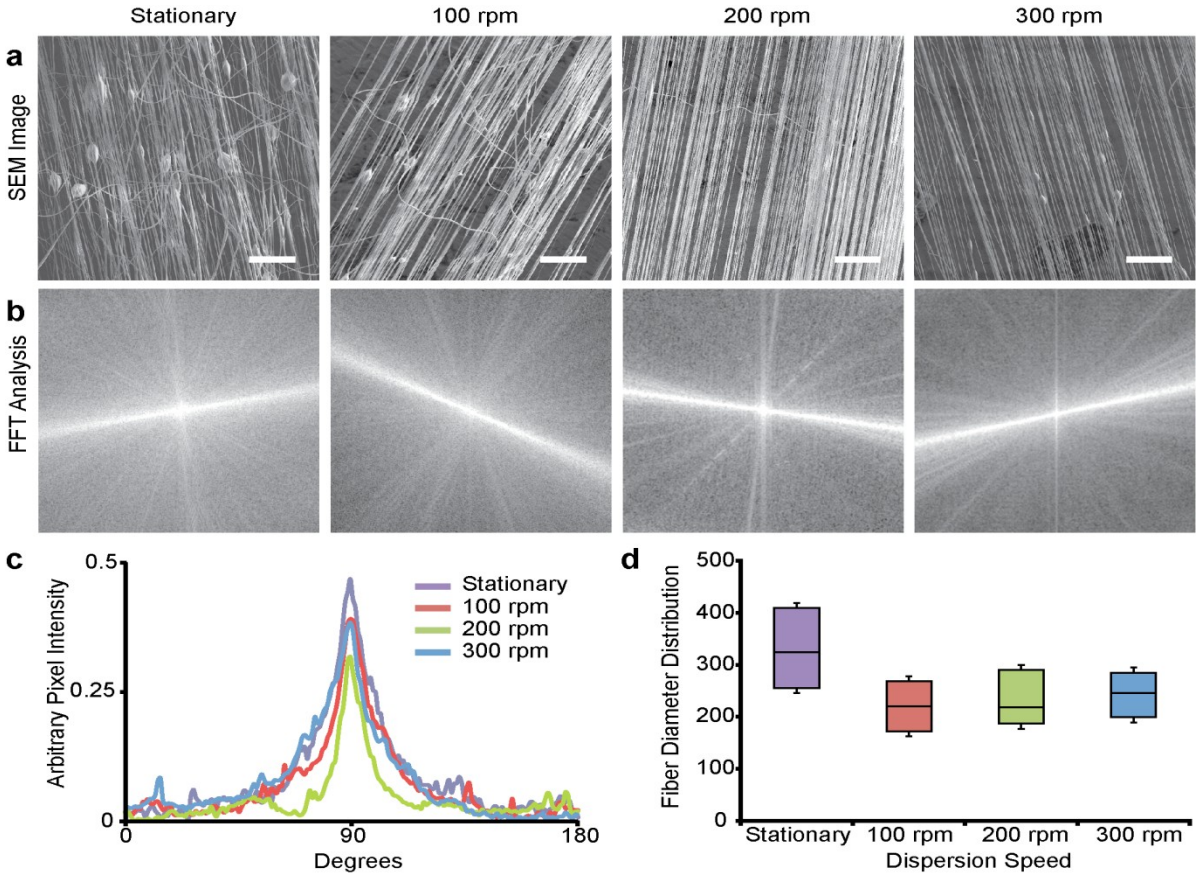

Figure 33. PVDF fibers produced at various spinneret rotational speeds. (a) SEM images of deposited PVDF nanofibers (scale bars = 20 μm). (b) FFT analysis illustrating the degree of alignment. (c) Arbitrary pixel intensity plotted from the radial summation of pixel intensity from the FFT analysis. (d) Fiber diameter distribution with the median diameter represented by the horizontal line shown in the middle of the bar. The error bars indicate the largest and smallest fiber diameters measured from a dataset of 50 fibers.

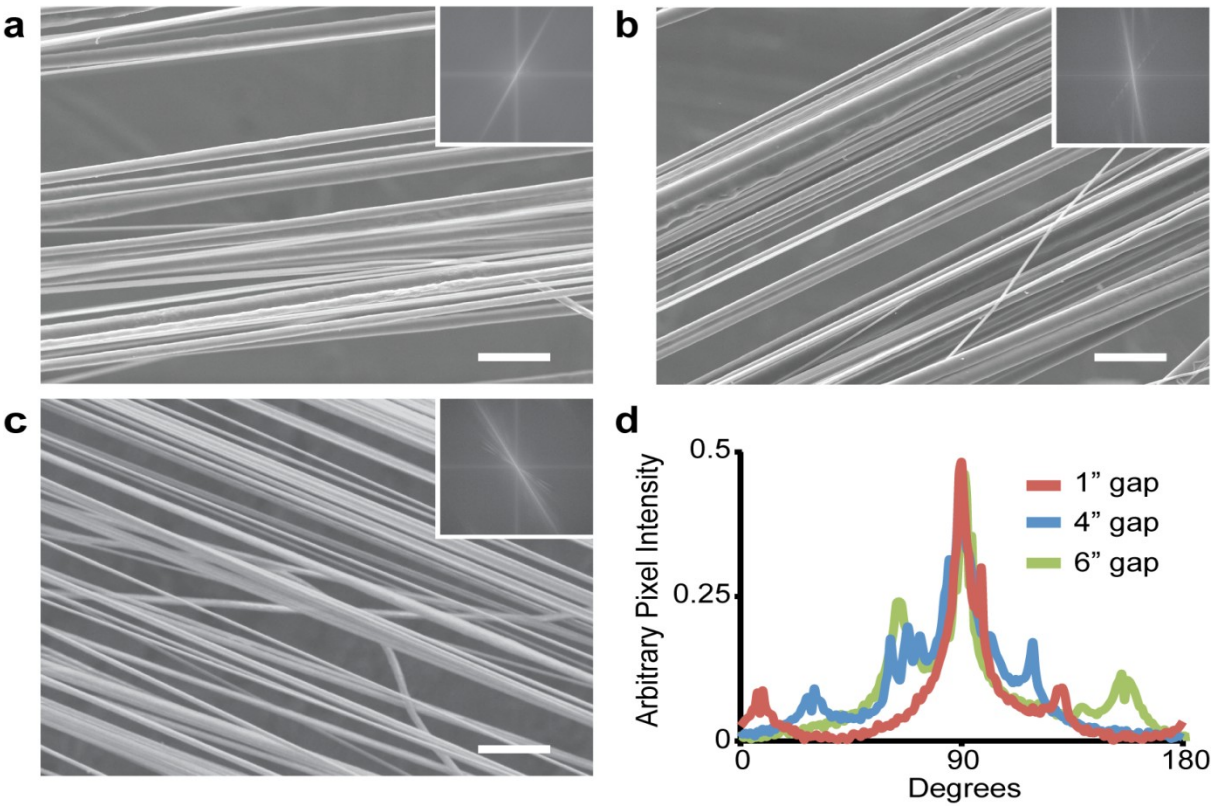

Figure 34. PVDF fiber morphology as a function of the electrode gap width. SEM images of the PVDF nanofibers deposited on (a) one-inch, (b) four-inch, and (c) six-inch electrode gaps. The scale bars represent 2 μm. Insets in (a), (b), and (c) are the FFT analysis illustrating the degree of alignment. (d) Arbitrary pixel intensity plotted from the radial summation of pixel intensity from the FFT analysis.

6.7 Production of Synthetic and Natural Polymer Fibers

The CE setup was used to produce alternative polymers to demonstrate the setup's versatility in producing aligned polymer nanofibers. Using a similar methodology described with the PVDF system, aligned PEO and chitosan-based nanofibers were produced. As shown in Figure 6a, aligned PEO fibers were produced with a diameter of average diameter of 270 nm from a 4wt% solution in water using 22KV$_{dc}$, 300 rpm, 20 cm spinneret-electrode distance. As shown in Figure 12b, aligned chitosan-based fibers were produced with a diameter of (number nm) from a 4wt% solution in water using the 22kVdc,

300-rpm, 20-cm spinneret-electrode distance. Both polymer systems were highly aligned; however, some “stray” fibers were attributed to the non-conductivity of the polymer [165]. Particularly, the “strayed” fibers were substantially thinner than the majority of fibers and were potentially more susceptible to repulsion by the previously deposited fibers.

6.8 Example of Significant Role Electrospinning Has in Tissue Engineering

Within the Zhang group one of the graduate students [225] used the aforementioned highly aligning nanofiber CES electrospinner to create a significant scaffold improvement for cell immobilization of Schwann cells as both fiber scaffold morphology and cell spreading capability contribute to the important role of tissue regeneration. For example, Schwann cell are particularly dependent on alignment as a precursor for nerve cell differentiation and modulation during the re-innervation process [166]. The influence of aligned chitosan-PCL nanofibers on regulating cell adhesion and spreading was investigated by incubating Schwann cells on aligned chitosan-PCL nanofibers and comparing with cells incubated on randomly oriented chitosan and examining them with both fluorescence microscopy and SEM. As shown in Figure 35, Schwann cells attach and spread on the chitosan-PCL film and random chitosan-PCL fiber mat, exhibiting a multi-polar morphology, as also observed on flat substrates in other studies [180,181]. Conversely, Schwann cells on the highly aligned chitosan-PCL nanofibers exhibited an extended, bipolar morphology aligned along the direction of the fiber orientation. Although the cell proliferation rates were comparable on all material surfaces studied here, the multi-polar and un-oriented morphology of the Schwann cells on the cast film and randomly oriented fiber mat would be less favorable for applications such as nerve regeneration compared to oriented cell growth. The increased

presence of elongated microvilli from the attached Schwann cells indicates actin-mediated adhesion that is necessary for Schwann cell differentiation and myelination for nerve regeneration [182]. SEM images in Figure 35 further detail the interactions of Schwann cells with three material surfaces and show the elongated microvilli extended from the attached Schwann cells on the aligned nanofibers.

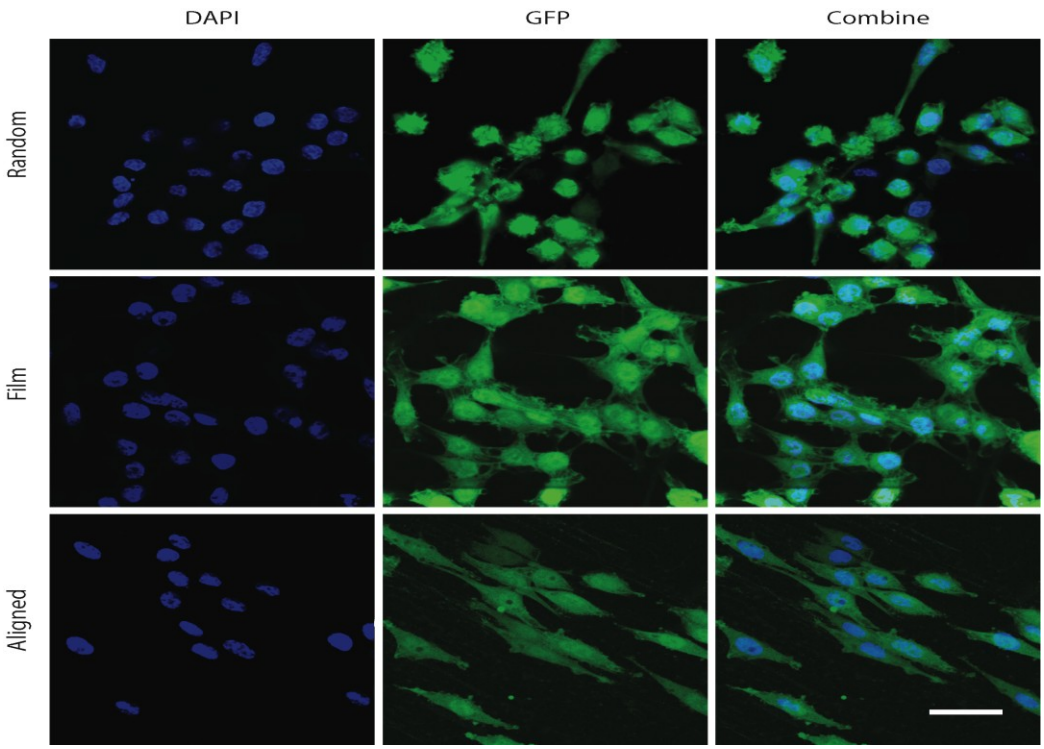

Figure 35. GFP+ Schwann cells with DAPI nuclei stain on chitosan-PCL film, random and aligned chitosan-PCL nanofiber mats after three days of cell culture. Scale bar is100μm. [225]

6.9 Characterization of CES Apparatus

6.9.1 Parameter optimization: The CES setup was characterized by optimizing the polymer concentration, applied voltage, spinneret-ground distance, the polymer feed-rate (needle gauge) by electrospinning poly-vinylidene fluoride tetrafluoroethylene (PVDF-TeFE), 80-20 molar ratio, Kynar 761). A solvent mixture of di-methyl formamide (DMF) and acetone at a weight ratio of 60/40 was used. A range of 15wt% to 30wt% polymer concentrations were initially tested to determine the concentration range for uniform fiber formation. To determine the effect of the centrifugal, rotating polymer jet on the alignment process, a 25wt% (PVDF-TeFE) solution was spun at 0, 30, 60, 120, and 150 rpm. The polymer feed rate was controlled at a pressure of 5 psi (25 g needle), the gap distance was 4 cm, the applied voltage was 15 kV, and the spinneret-ground distance was 20 cm. To determine the effect of a concentration on the fiber diameter, 18, 20, 22, and 25wt% (PVDF-TeFE) were electrospun at 150 rpm. The polymer feed rate was controlled at a pressure of 5 psi (25-gauge needle), the gap distance was 4 cm, the applied voltage was 15kV, and the spinneret-ground distance was 20 cm. To determine the effect of applied voltage on alignment and fiber diameter, 25wt % (PVDF-TeFE) was electrospun at 10, 15, 22, and 25kV. The polymer feed rate was controlled at a pressure of 5 psi (25-gauge needle), the gap distance was 4 cm, the rotational speed was set to 150 rpm, and the spinneret-ground distance was 20 cm.

To determine the effect of polymer feed rate on the fiber diameter, 20wt% (PVDF-Tetra-FE) was electrospun at a constant pressure (5 psi) with 20, 22, and 25-gauge needles (0.603, 0.413, and 0.260 mm inner diameter). Additionally, the gauge was held constant

(25 G) and the air pressure was varied from 5, 10, and 20 psi. The gap distance was 4 cm, the speed was 150 rpm, and the spinneret-ground distance was 20 cm. To determine the effect of the spinneret-ground distance, 25wt% (PVDF-Tetra-FE) was electrospun at 15kV, 150 rpm, 5 psi (25 g needle) and fibers were collected at 5, 10, and 20 cm. To determine the effect of gap distance, 25wt% (PVDF-Tetra-FE) was electrospun at 15kV, 150 rpm, 5 psi (25-gauge needle), spinneret-ground distance of 20 cm, and samples were retrieved from two gap distances — 4 cm and 8 cm.

6.9.2 Fabrication of chitosan: Chitosan is electrospun at very low concentrations (~4wt**%** or less) and spins very slowly due to its high viscosity. As a result, chitosan is often electrospun with copolymers or additives, thus limiting the production of pure chitosan fibers lessening biocompatibility. In this study, the pressure-induced feed rate allowed the flow of very high-viscosity chitosan solutions. Chitosan (practical grade, Sigma) 10wt% was dissolved in trifluoroacetic acid/methylene chloride (90/10vol %) and refluxed at 70°C for 3 hrs. The solution was CES electrospun with a spinneret rotor speed of 310 rpm, 15 psi, 22 kV, 4-cm gap and 20-cm spinneret-ground distance (Figure 36).

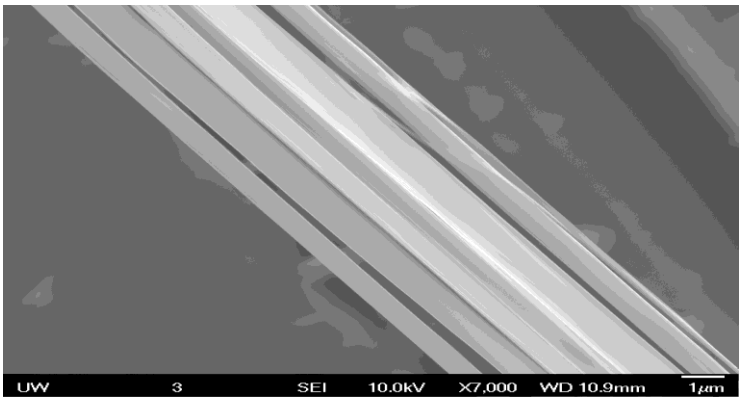

Figure 36. CES electrospun technique and pressure assistance.

6.9.3 Viscosity measurements: For calculation of the polymer feed rates, the viscosity of the polymer solutions were measured using a Haake-Viscotester VT550 Rheometer (HAAKE, Paramus, NJ) setup with a SV sensor system consisting of a SV cup with a SV2 rotor. The SV2 rotor has an inner cylinder radius of 10.1 mm and a height of 19.6 mm, outer cylinder cup radius of 11.55 mm, providing a radii ratio Ra/Ri of 1.14 with a gap width of 1.45 mm and a sample volume of 6.0 cm^3. The samples were run at 25°C with the temperature maintained by a circulating water bath (DC-10, HAAKE). Samples were measured for 1000s up to a shear rate of 100 s^{-1}.

6.9.4 Fiber characterization: Fiber samples were removed for each of the parameter conditions and were sputter-coated with Au/Gd for 30 s at 18 mA and imaged with a scanning electron microscope (Joel JSM 7000F). For fiber diameter analysis, triplicate images of each sample were taken and the diameter was averaged of at least 100 fibers. Fast Fourier transform (FFT) was performed using Image-J on a representative image to determine the fiber alignment. Briefly, an image was uploaded into Image (NIH, Bethesda, MD, USA, http://rsb.info.nih.gov/ij/) and FFT analysis produced a pixel intensity image based on the frequency of the original, which correlates to the direction of the fibers. The pixel intensities are then summed along a line from the center to the edge of the image to quantify the relative contributions of all parallel objects. A randomly oriented fiber image would result in diffuse, radial pixel intensities, whereas a perfectly aligned fiber would produce a horizontal line that was perpendicular to the original fiber orientation. The FFT images was normalized to a vertical access and radial pixel summing was performed using

the oval prolife plug-in authored by Bill O'Connell, http://rsbweb.nih.gov/ij/plugins/oval-profile.html.

6.10. Piezoelectric Characterization of Aligned Polyvinylidene Fluoride (PVDF) Nanofibers

Additional investigation beyond significant nanofiber alignment generation (Figure 33), was investigated to determine voltage out from a bundle of polyvinylidene fluoride and tetra-fluoride-ethylene-fluoride co-polymer with addition of tetrabutyl ammonium chloride nanofibers. Figures 37 and 38 illustrate the straight nanofiber bundle encased within PDMS in Figure 37a. Upon deflection by force F in Figure 39a results in a voltage shown in Figure 37b and Figure 40.

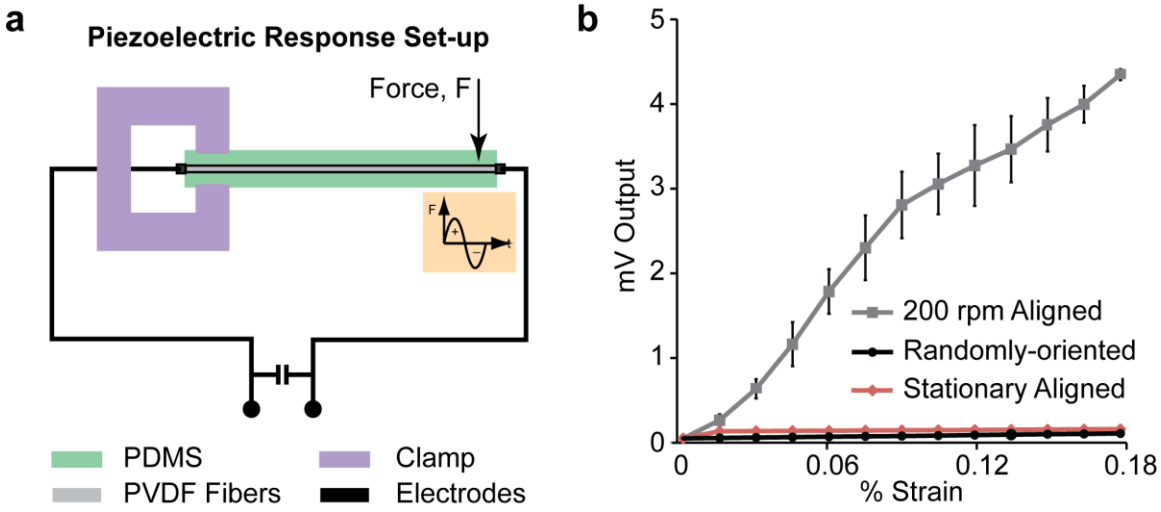

Figure 37. Piezoelectric characterization of PVDF fibers. (a) Schematic of the setup employed to test the piezoelectric behavior of aligned and randomly oriented PVDF-Tetra-FE and TBAC fibers. Fiber specimens were cast in PDMS, connected to electrodes, fixed via a clamp at one end, and deflected at the opposite cantilever end. The resulting (b) piezoelectric voltage output was measured (n=3).

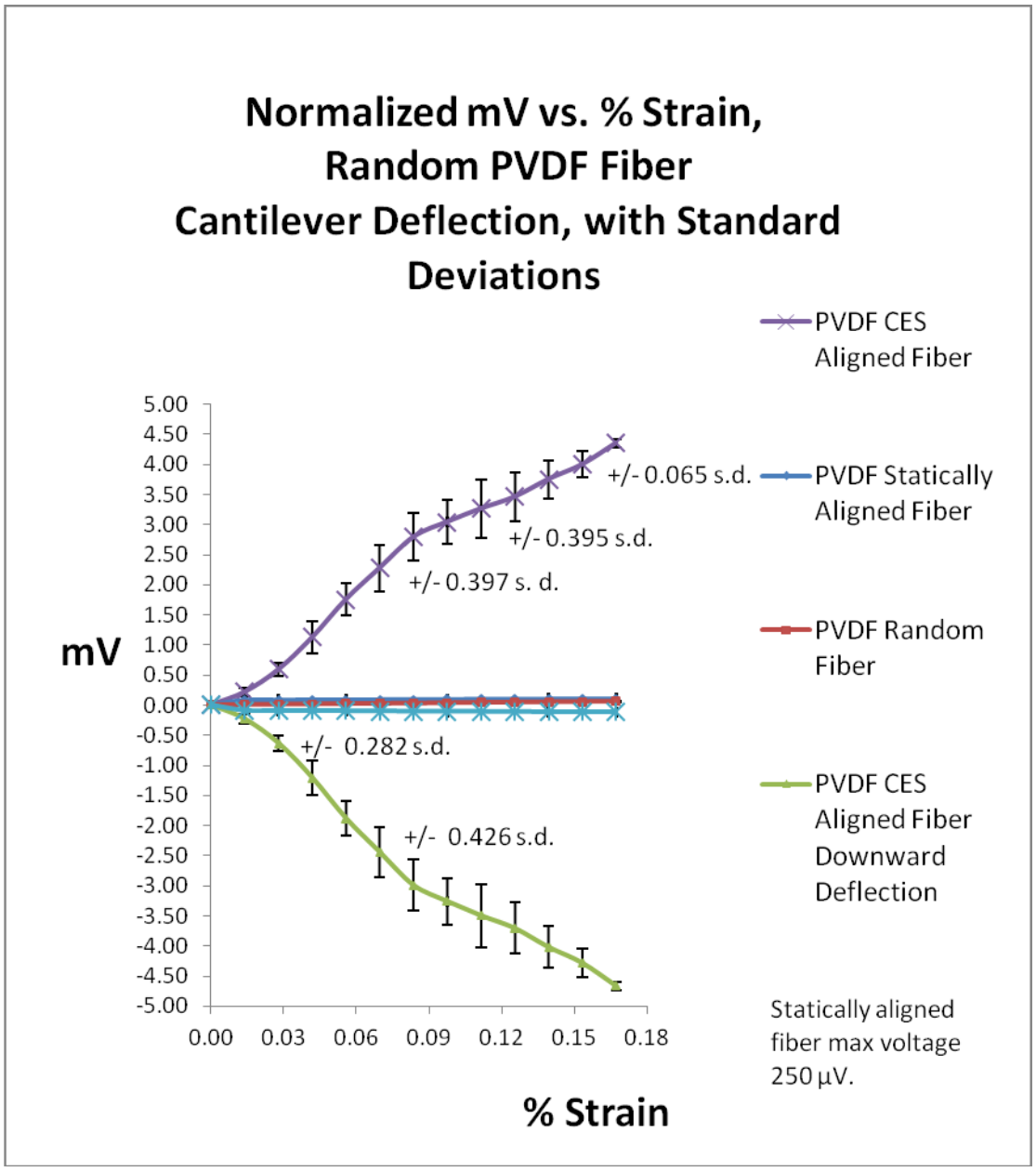

Figure 38. Piezoelectric characterization of PVDF nanofibers for states of centrifugally generated highly aligned fibers (Figure 32), and statically collected aligned and random generated nanofibers. Note uniformity of voltage in either direction of beam deflection.

As shown in Figures 37 and 38, piezoelectric PVDF DMF/Acetone solution electrospun into aligned nanofibers can become an organized bundle for generating electrical activity in either direction of deflection.

Chapter 7: Nano-Fiber Mechanical Characterization

Alginate, chitosan, PEO, PCL, and PCDF nanofibers have been successfully tested using the following tensile testing apparatus. The polysacorite and synthetic specimens tested with comparable results published elsewhere [115, 201] indicated effectiveness of tensile testing system in determining material mechanical properties. Tensile values for produced a Young's modulus, for dried alginate nanofibers with and without calcium chloride cross-linking, of 5 ± 1 (0.725E6 psi) and 7 ± 2MPa 1.015E6 psi) (respectively, and for wet nanofibers a value of 2.8± 1.2MPa (0.406E6 psi), Figure 3b. The material demonstrated elastomeric and crystalline characteristics with stress-strain curve beginning with a low slope to 50 microns and then increasing until the specimen breaks. The structural integrity of alginate-based nanofibers in an aqueous environment was determined by immersing alginate nanofibers into de-ionized (DI) water for up to 15 days with SEM images of the nanofibers taken at day 1 and day 15 and shown in Figures 3c and 3d, respectively. Examination of SEM images showed no apparent change in fiber morphology and that nanofibrous structure was retained. These values are comparable to those of human articular (skeleton joint) cartilage of 1-10 MPa as well as the equilibrium tensile modulus of bovine articular cartilage of 2-7MPa [203]. Nanofiber materials demonstrating structural viability would be used for cell viability testing as next described.

7.1 Nanotensile Tester to Characterize Fiber

A differential nanoscale tensile tester for nanofibers was developed using off the shelf components. The resolutions of displacement and load were achieved in nanometer and nano-Newton scales, respectively, which made this device unique. Tensile test on the model gold micro-wire proved the reliability on the data obtained from the device. The results on PEO nanofibers were also in the order of the published data. These studies indicate that our device, Figure 39, permits a highly efficient nanoscale tensile test on nanofibers.

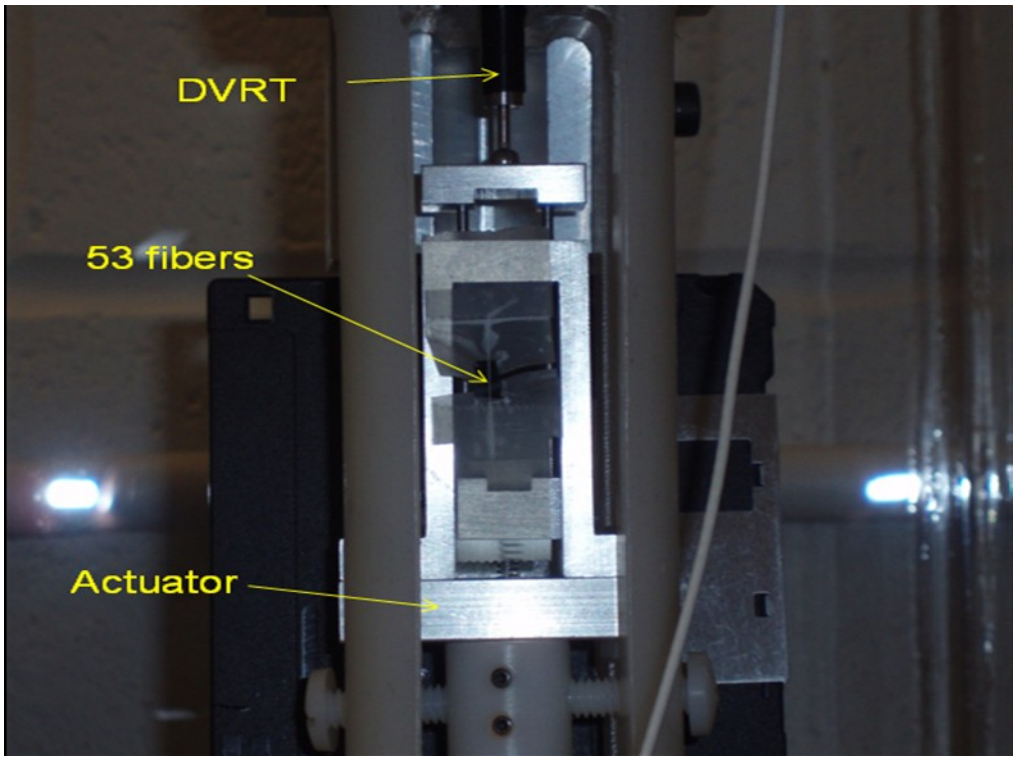

Figure 39. Nano-tensile/compression tester tension pulling 53 nanofibers.

Tensile strength characterization of fabricated nanofibers was performed using a novel 20nN to10N micro-tensile tester (Figure 41) developed in our laboratory [201] that uses differential motion as a method of loading. Polymeric and ceramic nanofibers have a wide range of applications in filtration devices, medical prosthesis, organ replacements, and tissue engineering [184-190]. In these materials and devices, individual fibers are the primary constituents, and their mechanical properties are of vital importance to their targeted functions. Several experimental methods including atomic force microscopy (AFM) indentation, three-point bending, lateral and axial fiber vibration measurement, and direct axial tension tests have been exploited in recent years to characterize the mechanical properties of nanofibers [191-194]. In AFM nano-indentation, the cylindrical contour of nanofibers will not quantify the correct contact stress and, therefore, it may offer intangible conditions in determining modulus [195]. Small off-axis angles of inclination formed between original and depressed location on the fiber in the AFM three-point loading technique could provide axial fiber force lower than the actual value [196, 197]. Transverse and axial fiber vibration measurement techniques are complex and could misinterpret the data, especially in axial vibration if a very tiny amount of load resistance contributed by the fiber is not taken into account [198-201].

For mechanical property characterization the tensile test is the most relevant among other methods since the major failure mode for nanofibers is tensile deformation as they support axial loads in many applications. Here we report the design and characterization of a simple and cost-effective tensile tester with resolution at nano-Newton and nanometer scales.

To test fibers a novel scaled-to-test specimen size tensile tester was mandatory [202]. The design required use of off the shelf components such as a differential variable reluctance transducer (DVRT) (MicroStrain, Inc., Williston, VT), the load transducer, a specimen holding differential fixture made of magnesium, and a stepper motor assembly. The DVRT utilizes dynamic core location detection through measuring internal coils' differential reluctance using a sine-wave excitation and synchronous demodulator circuit electronic signal conditioner. The transducer's coils and multi-stranded leads are sealed in by using vacuum-pumped epoxy within a stainless-steel case. This type of differential detection method provides a very sensitive measurement of core position while cancelling out temperature effects, which is important in extended usage. Both stress loading and data acquisition are performed by a computer acquiring information from a data-acquisition-system (DAQ) (National Instrument Inc., USA) connected to both DVRT and stepper motor assembly. An overall schematic diagram with DVRT mechanics is illustrated in Figure 40 along with simplified form of differential fixture without and with specimen spring contribution.

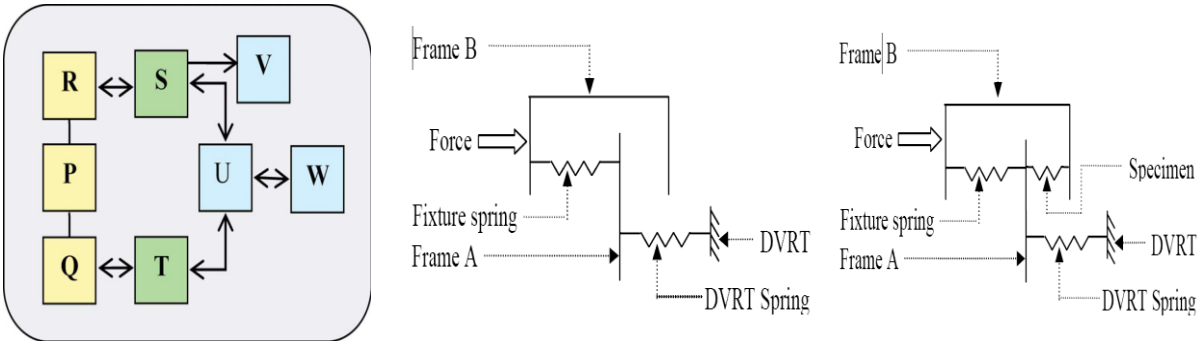

Figure 40. Overall schematic diagram of the device: P, differential fixture (frames-A and B); Q, stepper motor; R, DVRT and spring; S, noise canceling signal conditioner; T, stepper motor controller; U, DAQ; V, extra voltage display (generated from R); and W, computer.

Tensile strength characterization of fabricated nanofibers was performed using a novel 20nN to 10N micro-tensile tester developed in our laboratory [200] that uses differential motion as a sensor.

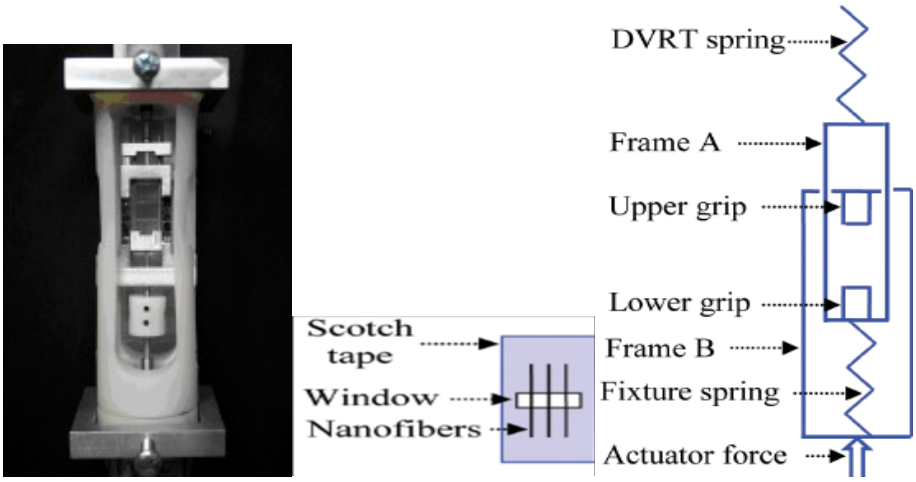

(a) (b) (c)

Figure 41. (a) 39nm resolution tensile tester with ability to support 20nN, 0.015N, or 1.0N load transducer heads; (b) two tape encapsulated specimen holder having edges of window snipped once specimen-tape ends are secured to grippers; (c) diagram illustrates differential action frames with opposing identical springs; specimen is between upper and lower grippers, see Appendix 1.

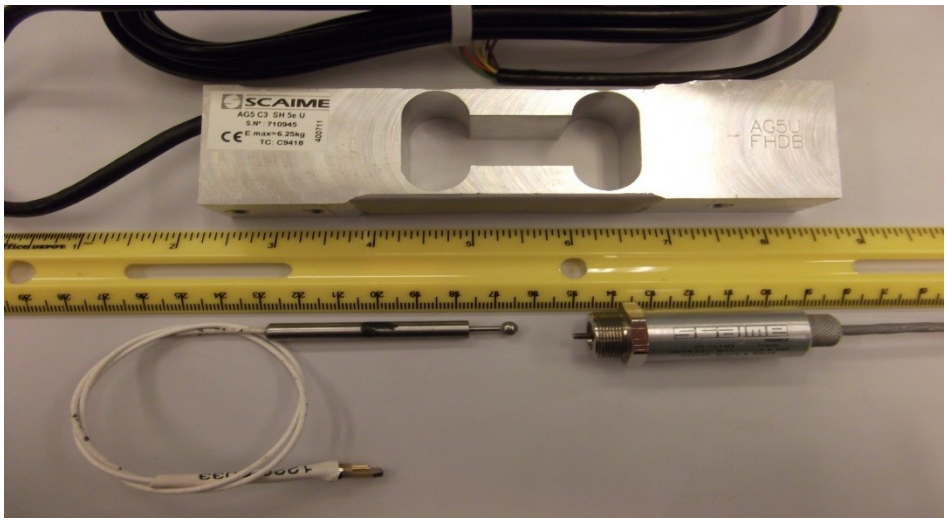

Figure 42. Transducer types used with Zhang lab nano tensile tester. Top, a 1kg (10N) load range; lower right, a +/-30 gm load range, tensile/compression range of 100nm, (both from PTC-Electronics, Wyckoff, NJ); lower left, a DVRT (differential voltage reluctance transformer) displacement/tensile-load range of 39nm and 20nN (MicroStrain, Williston, VT).

7.2 Differential Load Transducer Design (DVRT)

In the differential fixture (Figure 41), P in Figure 40, the sliding of small frame “A” into outer frame “B”, without force of friction, is performed with help from two springs having equal spring constant (0.1 N/mm). One spring, called fixture spring, is connected between left side of frame “A” and the left side of frame B, and another spring (DVRT spring) comes out of DVRT and is fixed to right side of frame “A”. When a force is applied at far left of frame “B”, Figure 43a, it moves right, generating a compressive force in fixture spring, which in turn applies a compressive force on DVRT spring through frame “A”. The mechanics behind this capability is presented in the simplified form of differential fixture (without specimen, Figure 43a; with specimen, Figure 43b).

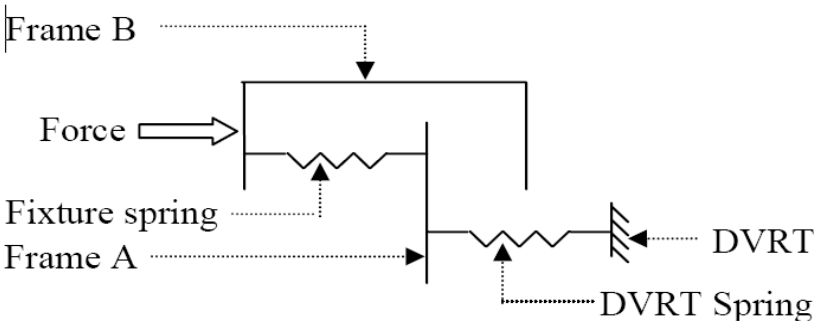

Figure 43a. Simplified form of differential fixture.

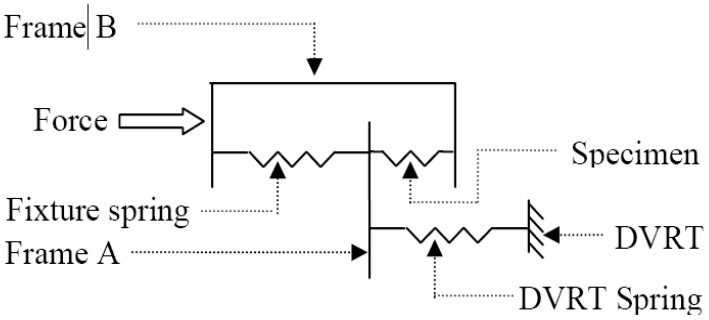

Figure 43b. With specimen present on Frame "B".

The rightward movement of frame "B" causes a tensile force applied to the specimen (if it exists) which, in turn, compels frame "A" to move rightward a distance depending on the equal spring constant of initial two springs as well as the stretching resistance (spring rate) from the specimen. Therefore, when a fiber is present between the grips, resistance from fiber against its stretching will generate an extra compressive force on the DVRT spring, and the DVRT will experience this extra force in addition to the compressive force in the spring generated by actuator extension force, causing frames "A" and "B" to move in opposite directions stretching specimen. The frames are made of magnesium to provide vibration damping as well as reduce weight effect on base spring. The aforementioned

allows frame **"**B**"** to move some distance *d* (equal to number of stepper motor steps times 39nm [0.000,000,039m]) under actuator force, causing frame **"**A**"** to displace *d*/2 for the reason that both springs have same spring constant and they are in series.

The differential voltage reluctance transformer (DVRT) will experience a force (F_1) through the compression of DVRT spring, which is equal to:

$$F = kd/2 = K_1 d, \quad (1)$$

where *k* is one spring constant, and K_1 a second spring constant equal to *k*/2. The discretized movement of stepper motor shaft produces discretized load on DVRT and the computer collects the corresponding DVRT Spring Frame "A" DVRT Frame **"**B**"** voltage signal and the number of steps in its data file (Figure 43a without specimen). Therefore, for a particular step number we can obtain value of *d* (step number times 39 nm) and the value of F_1 will be calculated using equation-1 for the obtained "*d"* value. Now both load (F_1) and voltage-signal values for a particular step number and a load-voltage conversion factor can be formulated. Thus, all generated load values for all the step numbers are collected in the data file and plotted as load values against the corresponding voltage signal and obtain an average load-voltage conversion factor. When specimen is present (Figure 43b), DVRT will experience an extra compression force from specimen stretch; thus displacement of frame "A" towards DVRT will some be "*x"* for '*d'* amount movement of frame **"**B**"**. The compression in fixture is then equal to "*d – x",* which is the elongation of specimen as the length of frame **"**B**"** is invariable. The compressive force in the DVRT spring will work against the compressive force in fixture spring as well as the force from specimen due to its elongation and therefore in equilibrium,

$$k(d - x) + k_s(d - x) = kx \quad (2)$$

Simplifying Equation-2, we get

$$x = (k + k_s / 2k + k_s)\, d = K_2\, d \quad (3)$$

where k_s is the specimen stiffness and K_2 is a constant which is equal to

$$k + k_s / 2k + k_s$$

The compression force (F_2) on DVRT is (when specimen present)

$$F_2 = kx = kK_2d = K_3d \quad (4)$$

where K_3, another new spring constant, is equal to kK_2. It is easily understood that equation 1 and equation 4 have similar format and both vary with d. This theoretical analysis has been corroborated by the experimental result. It should be noted that load and displacement are proportional to the voltage signal and step number, respectively. By comparing equations 1 and 4, it can also be realized that if there is an extra effect on DVRT due to specimen existence, K_2 should be greater than 1/2 and if this is hypothesized then,

$$K_2 > 1/2 \Rightarrow k + k_s / 2k + k_s > 1/2 \Rightarrow k_s > 0 \quad (5)$$

The inequality (5) indicates that if there is a specimen as shown in Figure 5, there is an extra effect on DVRT and therefore, its voltage vs. steps curve will be greater than curve for the system without specimen.

The highest voltage value obtained from the data file from the tensile test of specimen is then multiplied by the load-voltage conversion factor (9.8 N/V_{max}) to the obtain corresponding load. If the fibers break, the highest voltage value will be the value just before break. The achieved load value is divided by the DVRT spring constant (0.1 N/mm)

to get the corresponding displacement which is the value of *x*. The step number corresponding to the highest voltage (used for load calculation) is multiplied by actuator resolution (39 nm/step) to obtain the actuator movement *d*. Therefore, the total elongation of the specimen "*d – x"* is available, which is discretized using the discretized step numbers in the data file. To determine displacement resolution we use equation-3 for finding total elongation of specimen,

$$d - x = d - K_2 d = d(1 - K_2) \tag{6}$$

As $K_2 = k + k_s / 2k + k_s$ giving, upon rearranging, $1 - K_2 = 1/[2 + (k_s / k)]$

Now if $k_s > 0$ meaning there is kind of specimen present in the device, then

$$1 - K_2 < ½ \tag{7}$$

Considering equations 6 and 7, it can be speculated that for "*d"* axial movement of the shaft actuator, the displacement in specimen is less than *d/2* and therefore, we can conclude that minimum resolution of displacement is 19nm, which is half of the shaft's movement resolution, and the higher the stiffness of specimen the greater the displacement resolution. The axial force is provided by the stepper motor actuator screw assembly (Figure 41), and its value is measured with either a strain gage (SG) or very sensitive DVRT transducer. These displacement and force data are used by Lab View routine to calculate a point by point locus stress-strain curve (Figure 8).

7.3 Mechanical Force Transducer Parameters

The stepper motor threaded actuator shaft maintains an interference fit with the stepper motor threaded armature nut, and both having 200 threads per inch, which provides 1/200

or 0.005 inch per thread pitch. The stepper motor is controlled electronically by advancing the motor at 6400-step increments per actuator shaft revolution, resulting in 1,280,000 steps per inch of actuator shaft displacement equating to 0.000 000 781 25 inch axial advancement per step caused by servo-motor rotation. In operation the tensile tester can advance at 6400 [400 steps x 2 x 8 (the octal setting)] steps per actuator shaft revolution or 0.05625 degrees of rotation at rates to 20mm/min with motor controller-driver octal electronics used (The Motion Group, Clovis, CA).

7.3.1 The load transducer

The stepper motor actuator assembly, and specimen grippers are all proportionally sized for testing structural integrity of micro-samples. In operation the stepper motor and actuator screw supply force and displacement through controller electronics managed by Lab View software. The force determination is obtained using either a strain gauge (SG) or differential voltage reluctance transformer (DVRT) load cell transducer, and data transmitted via a data acquisition (DAQ) computer interface to Lab View system controlling software. The test specimen is sandwiched between two pieces of tape having center cutout (Figure 41b). The taped specimen ends are then attached to upper and lower grippers in Figure 57 (Appendix 1), and cutout edges snipped freeing specimen for tensile test. The axial extension (displacement) of test specimen is determined by the number of steps the stepper motor completes as directed by a Lab View program algorithm for computing the axial distance specimen stretches during tensile pull based on number of

total steps. Nano-tensile tester actuator shaft axial displacement is determined by following formula for one inch of thread length,

1 inch/{200 pitch x [400 steps/rev] x 2(8) octal}/[25.4 mm/inch/10^6nm/mm] = 19.844nm/step (8)

where 200 pitch are threads per inch, making each thread thickness 0.005 inch (0.127mm) and results in axial advancement of 19.844nm per stepper motor increment of rotation, which is 300% less than the diameter of an individual testing fiber. It requires 6400 incremental steps to complete one full stepper motor shaft revolution, which equates to one thread thickness (0.005inch) of specimen displacement. As an example, if 20 steps per input signal from Lab View to **"**GO**"** command in Lab View vi computer software routine, then axial advancement of actuator shaft will move 20 times 0.05625 degrees or 1.125 degrees of an arc. The steel actuator shaft contains 200 threads per inch (25.4mm), then each thread is 0.005 inch (0.127mm) in width providing same 0.005 inch in axial advance per one shaft revolution. Thus, for example, 20 steps (around the thread helix) input signal from a Lab View **"**GO**"** command, the actuator shaft will advance axially by 0.000 015 63 inch (0.000 396 88 mm) axially. Each step will cause load cell transducer to experience deflection, creating a current decrease change in the foil strain gage sensors in load transducer, and signal conditioner converts this change to voltage per axial movement and Lab View, Figure 44, records the value for each step and continues to do so as long as input loading is increased on test specimen. The formula used in Lab View to calculate material stress is,

$$\sigma = \text{Stress} = \text{Force/Area} = [(V_{output})(9.8\ N/V_{max})]/m^2 \qquad (9)$$

where V_{output} is load cell output voltage from SG load cell and N/V_{max} the load cell factor based on 9.8 Newtons (1000g load cell or [9.8N]) divided by maximum voltage range of load cell V_{max}, which is 10 volts, e.g., as volts out increase so does stress value.

7.4 Load Transducer Characterization

To characterize nano-tensile tester, a calibration technique using 99.995% pure gold 0.0005 inch (0.0127mm) diameter wire (Alfa-Aesar, NY) specimen having a known modulus of elasticity of 78-80GPa (11.5E6 psi) 190[7] was used. The nano-tensile tester measured a value of 78.5GPa (11.38E6 psi) (inset figure-45b). In operation actuator force compresses fixture spring, which directly compresses an equivalent spring force inside DVRT sensor. As frame “B” passes by frame “A” in opposite directions, without contact, the specimen attached between grippers is stretched.

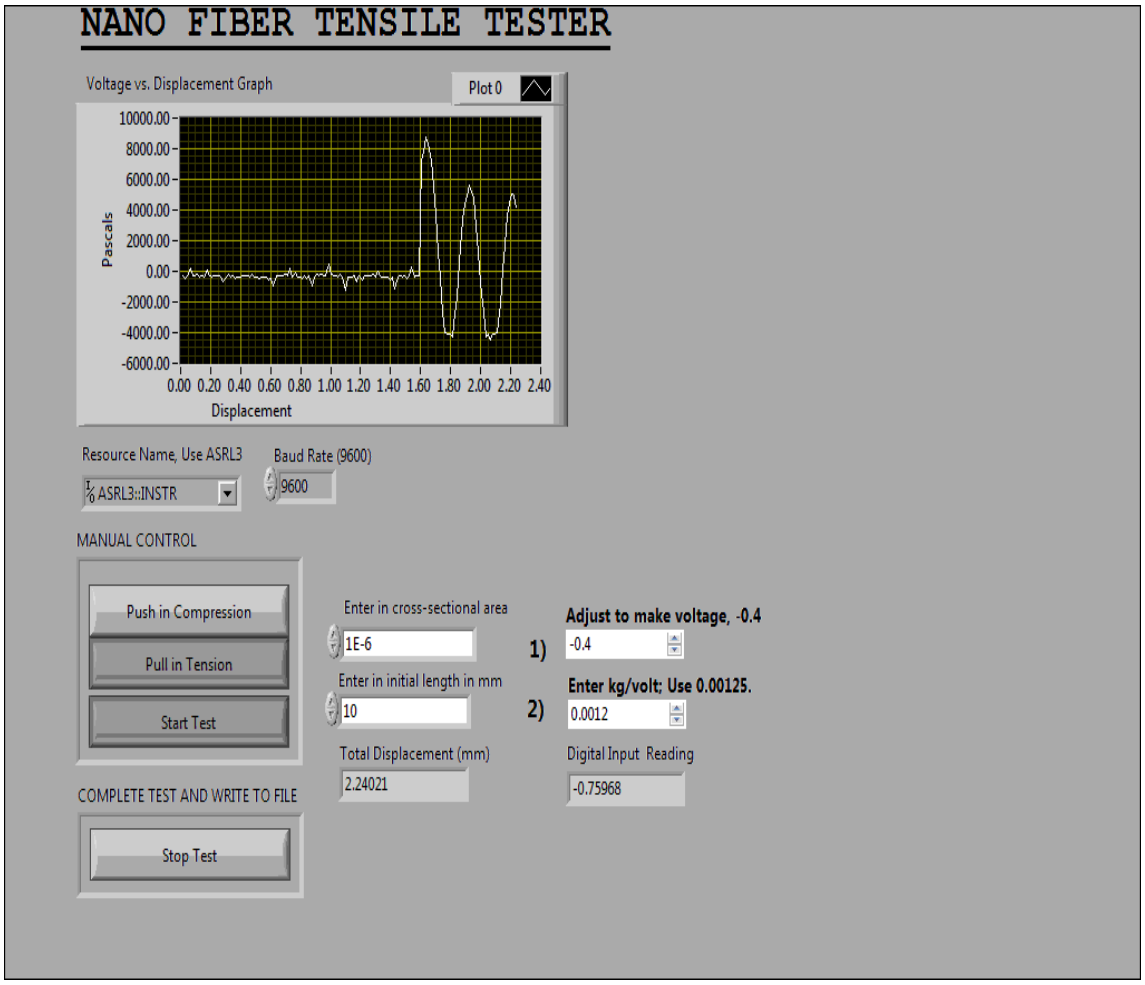

Figure 44. Labview output display for nano-tensile tester. Curve illustrates tension and compression for an up and down motion applied to load transducer via stepper motor.

Small tensile spring rate of specimen adds to further compression of DVRT spring, providing a slightly higher electronics signal from DVRT to be recorded than if specimen is missing. Then a second test is conducted without specimen and the one-for-one first test matching displacement test forces is subtracted from those of first test and the difference determines the specimen's spring rate (Figure 45a).

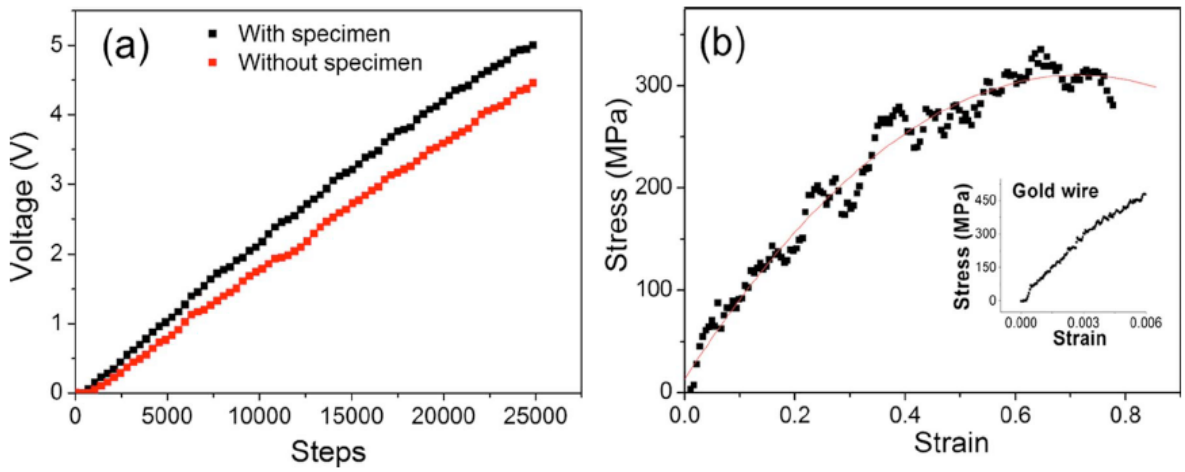

Figure 45. (a) Two separate tensile tests are conducted, one with specimen and one without, see Figures 39 and 40; (b) curve resulting from subtracting the two tensile tests arriving at specimens contribution.

Knowing the specimen's cross-sectional area and original un-stretched length allows plotting of a stress-strain curve as in Figure 45b by using standard stress and strain formulas. In Figure 46 below, a wet and dry specimen of alginate is represented by curves that characterized it in tension which provided values similar to published data.

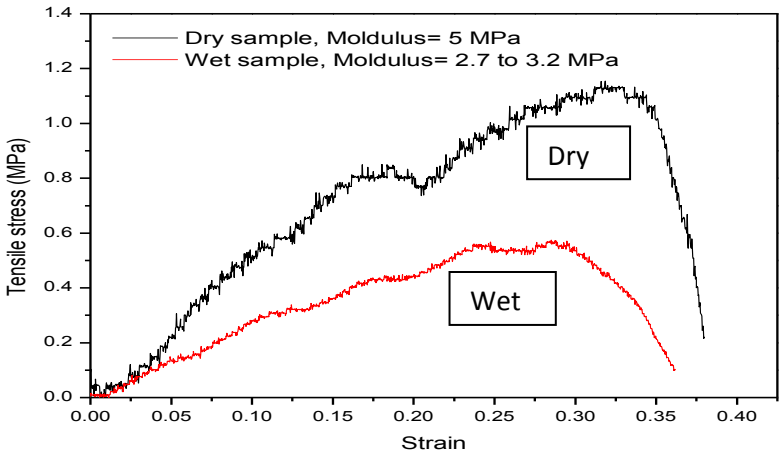

Figure 46. Alginate stress-strain curve for dry and wet specimens.

7.5 Measurement of Single Nanofibers

Aligned PEO nanofibers produced by an electrospinning process [191] were collected on a Scotch tape containing a small window at the center (Figure 41b). Another Scotch tape with the same dimension and window was placed on the first one in such a way that the nanofibers were sandwiched between two strips of tape. Scanning electron microscopy (SEM) image of aligned nanofibers is shown in Figure 47. The number of fibers present inside the tape window was determined using a light microscope. The sandwiched tape set was then attached to the grippers; the DVRT was zeroed and the tape in both sides of the window was snapped, providing freedom to the nanofibers to elongate. After the completion of tensile test, the number of broken nanofibers was counted again to verify that the same quantity of fibers was present after the test.

Using SEM, we obtained the diameters of the fibers (ranging from 300 nm to 1μm), which were used to calculate stress (load/total area of the fiber set) in fibers. The height of the window, i.e., the initial length of the fibers, was used to find the strain by using the calculated discretized elongation data (see supplementary information) [189]. Two sets of data (stress and strain) were plotted to find the tensile modulus of nanofibers (Figure 45b). The observed result on the PEO nanofiber from this differential tensile test device showed its Young's modulus of 617MPa, which lays between the published values of 45 MPa and 7±0.5 GPa 187, [192]. The variation in modulus values of PEO nanofibers is caused by the PEO concentration and fabrication method.

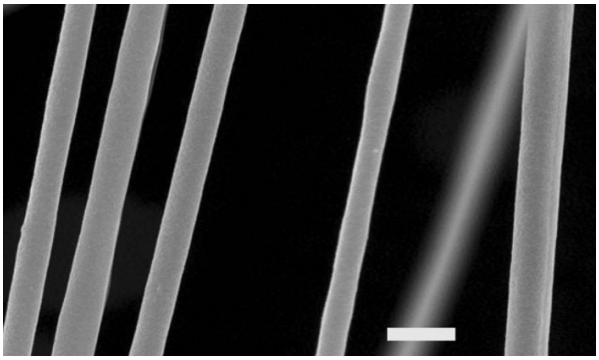

Figure 47. SEM image of electrospun PEO nanofibers used for tensile test with scale bar indicating 1μm.

7.6 Fiber Orientation Strength Comparison

The following figures present stress-strain curves obtained from using nano-tensile tester (Figure 48), using PVDF aligned fibers (Figure 49), using PVDF random fibers, and Figure 50 using PVDF film with all strength values normalized. The data for aligned fibers was taken from a specimen where fibers were not snuggly bunched, so we expect greater stress capability from real cross-sectional area over the apparent area used in aligned PVDF fibers tensile test. In Figure 49 the random fibers created from PVDF also had considerable porosity, and values will also be subjected to apparent verses real cross-sectional area. For thin film PVDF (Figure 50), the molecular structure places PVDF chains much closer together, presenting a real cross-sectional area, and yet PVDF film was not as strong as our electrospun aligned and random PVDF fibers in Figures 48 and 49, respectively. This tensile test demonstrated that there is a significant improvement in PVDF polymer strength when fiber poling is used in electrospinning aligned nanofibers as is the case with our centrifugal electrospinner. We have developed a new high-through-

put collector designed to work with the centrifugal electrospinner that displays significant promise in collecting aligned fibers (paper in process).

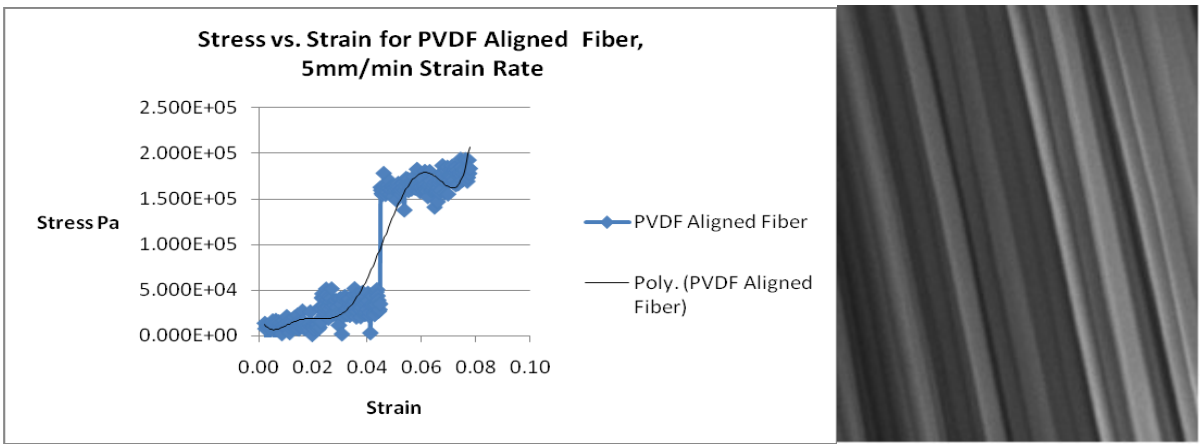

Figure 48. PVDF aligned fiber. Horizontal data compressed to display.

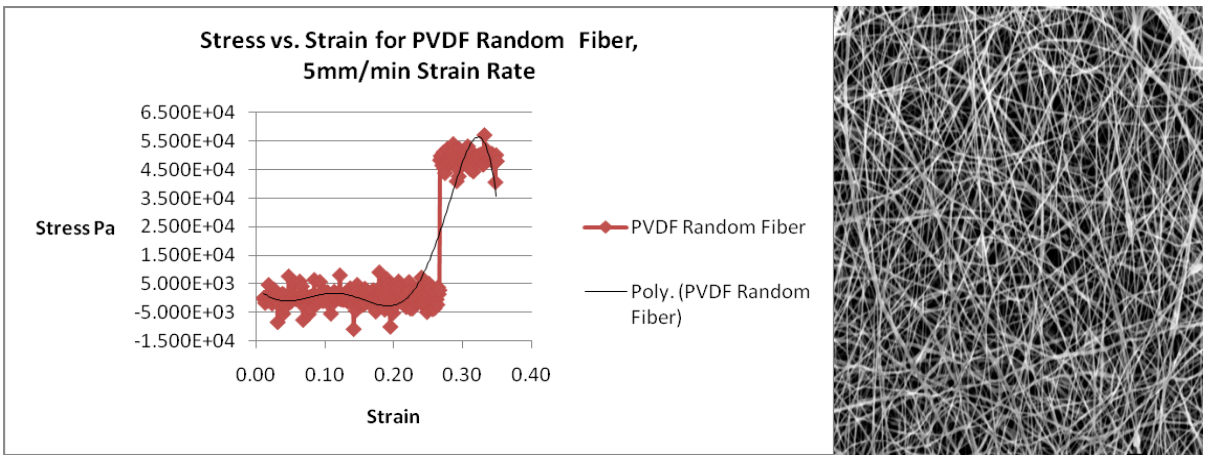

Figure 49. PVDF random fiber. Horizontal data compressed to display.

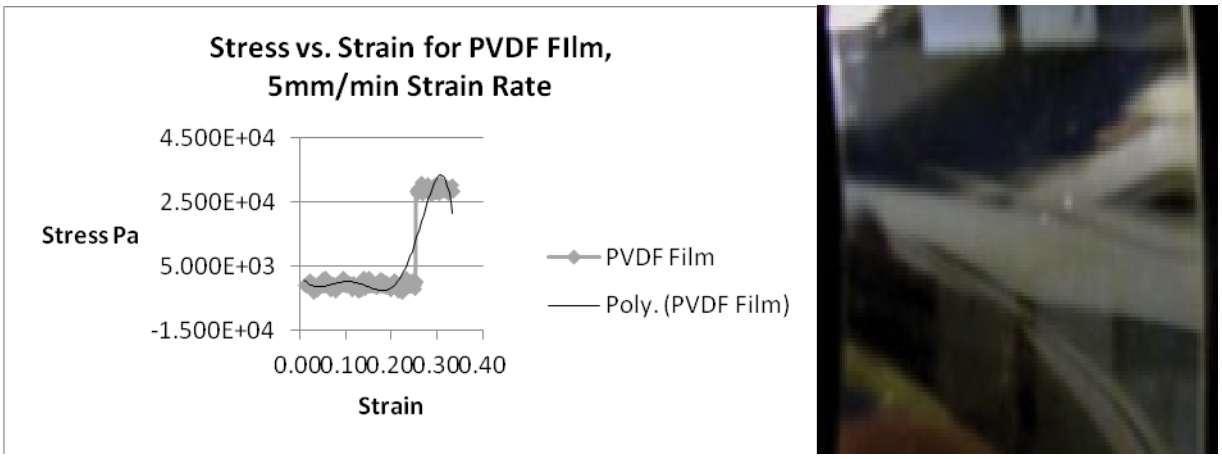

Figure 50. PVDF film. Horizontal data compressed to display.

Chapter 8: Uniaxially Aligned PVDF Nanofibers as Sensor and Transmitter for Biotelemetry

Biotelemetry has become an important part of medical research for patient care by remotely monitoring continuing biological processes and physiological functions. However, current biotelemetry systems are complex, requiring multiple electronic components to function: a battery, a sensor, a transmitter, and a receiver. Another paramount concern of biotelemetry is the coupling of its *in vivo* portion to external supporting equipment. Here we report a novel biotelemetry device made primarily of a coiled bundle of uniaxially aligned biocompatible polyvinylidene fluoride (PVDF) nanofibers of ~200 nm in diameter and with piezoelectric properties that can serve concurrently as power source, sensor, and transmitter. We tested this device on a cantilever beam that was periodically deflected at its free end. Without a power supply the coil of nanofiber bundle generates and transmits an electrical signal wirelessly in response to the beam deflection, which was received by an external receiver. The coil of nanofiber bundle was encapsulated in thin biocompatible polymer shell for device integrity and moisture isolation. Our results suggest that the device can potentially serve as a mechanical sensor and bio-telemeter for various *in vitro* and *in vivo* biomedical applications.

Biotelemetry is a telemetric method used to remotely monitor, record, and measure basic physiological functions such as body temperature, blood pressure, muscle activity, and heart rate of living organisms [203,207,209,210]. It uses onboard sensors and power source to detect and subsequently transmit information, either with wires or wirelessly, for further evaluation [210,212,214,218]. Wireless biotelemetry obviates the need for a direct

physical connection between the source and receiver [213,220], and thus is favorable for *in vivo* biomedical applications.

Since the development of the transistor and integrated circuit systems, it became possible to design small and low-power consumable biotelemetry devices for implantation in the body [211,213,215,217,219]. However, current implantable biotelemetry devices still need a separate sensor, power source, and transmitter onboard to function efficiently. These three components not only make the device sophisticated but also lead to increased device size [206,212,220]. The need for an onboard battery is more problematic as the power source miniaturization and prolonged service time remain a formidable challenge [220]. These concerns are particularly critical in cardiac applications such as pacemakers, where battery replacement is inconvenient and potentially life threatening. Moreover, batteries must be carefully sealed because even a minute degree of moisture ingression can cause its failure [214].

In our previous study [209], we describe a centrifugal electro-spinning process to produce long, aligned polyvinylidene fluoride (PVDF) nanofibers and demonstrated that these nanofibers showed a strong piezoelectric property when a small stress/strain was applied [209]. In this study, we used a bundle of uniaxially aligned PVDF nanofibers to construct a spiral coil that can serve as a bio-telemeter. Unlike other biotelemetry devices, this tiny, single-component device performs all three major functions required for biotelemetry: sensing, power sourcing, and signal transmitting. The spiral coil is completely encased by a layer of biocompatible polydimethylsiloxane (PDMS) polymer protecting the device from moisture and maintaining device integrity. We tested this device by affixing it on a

cantilever, and the signal generated by the device when the cantilever was deflected was received both wirelessly by a receiver and through wire connection to a signal conditioner (as a reference). We further assessed the influence of the degree of the cantilever reflection as well as the distance between the biotelemetry device and the receiver on the signal strength received (Figure 58).

8.1 PVDF Nanofiber Fabrication

Polyvinylidene fluoride tetrafluoroethylene and polyvinylidene fluoride (PVDF) (Arkema Corporation, King of Prussia, PA) were mixed at a 70/30 weight ratio. The polymer mixture with 0.3wt% tetrabutyl ammonium chloride (TBAC) (Sigma-Aldrich Co, St. Louis) was dissolved in dimethyl formamide (DMF)/acetone at a weight ratio of 60/40 to create a final polymer concentration of 20wt%. To aid in the dissolution, the PVDF solution was mixed at 80°C for 45 min in a magnetically stirred flask. The resulting solution was electrospun in a centrifugal electrospinner (CES) system [209] to obtain ~4 inch long uniaxially aligned PVDF nanofibers of 200–250 nm in diameter. The produced nanofibers were collected from the gap between the electrodes of the electrospinning system as a bundle to make a coil.

8.2 Encasing of PVDF Nanofibrous Bundle in PDMS

The nanofiber spiral coil was soaked in PDMS solution by holding one end of fiber bundle with lab tweezers and submerging and dragging bundle one time through PDMS, located in a one-inch deep by six-inch diameter cylinder petri dish, causing individual fibers to

become a closely packed bundle. The fiber bundle was then pulled across rounded glass edges of cylindrical petri dish ten times to scrape excess PDMS off fiber bundle. The nanofiber bundle, one end still held by tweezers, was then manually coiled into a spiral configuration onto a flat glass lab slide surface with an additional thin coating of PDMS pored over to ensure encased spiral coil would stay attached when cured. The spiral coil and the flat glass slide were then placed in an oven maintained at 80°C for 24 hours to cure PDMS. after which the spiral PVDF coil was removed from glass slide for use in voltage signal measurements.

8.3 Voltage-Current Signal Measurements

In fabrication of an aluminum cantilever test beam, a foil strain gauge (Micro-Measurements, Raleigh, NC) was attached to the bottom side of our aluminum cantilever beam using Eastman 910 super glue and connected to a signal conditioner portion of the NI9219 (National Instruments), which was connected to a computer through an NI data acquisition (DAQ) chassis. On the top side of the beam, the PVDF spiral bundle was attached just above the foil strain gauge, with wire leads connected to the voltage measurement portion of the NI9219 and then the DAQ. Two strain and one transmitted signal measurements were collected with all three recorded as voltages. A receiving antenna coil (AC) was fabricated using number 42 lacquer-coated magnet wire encased in a deep-well annular ferrite core, coated with PDMS and cured at 80°C for 24 hours. Antenna was connected to a nano-voltmeter 34420A (Agilant, Cupertino), which was connected to the computer through an NI data acquisition (DAQ) chassis. A Lab View vi program was used to obtain the signals from both the nanofiber coil and foil strain gauge.

8.4 Biotelemetry Setup

The coil of PVDF nanofiber bundle was prepared by a process described in the methods section. The diameter of nanofibers in the bundle was in the range of 200–300 nm (Figure 51a) and the size of nanofiber bundle was in the range of 6–8μm (Figure 51b). To test the effectiveness of this coil in generating and transmitting a voltage signal, the coil was attached to the top side of the aluminum cantilever beam and the foil strain gauge was attached to the bottom side of the cantilever beam right blow the coil (Figure 52). In this configuration the coil and foil strain gauges would be subjected to the same strain condition but with coil in compression and foil strain gauge in tension when beam is deflected upward (Figure 52). This stress direction would be reversed when the beam was deflected downward. Figures 58 and 59 show photographs of the coil, tensile tester, aluminum cantilever beam and foil strain gauge. Figure 52a and Figure 52b show schematically the coil and receiver antenna, respectively, whereas Figure 52c illustrates the setup of the test system. In this configuration, the foil stain gauge was used as a reference. The foil gauge is operated through an NI9219 electronics module containing both power supply and signal conditioner circuitry. When a current is supplied to the foil strain gauge, the signal conditioner determines the corresponding strain value from current variations and thus, strain values from applied voltage and bending of foil strain gauge can be compared.

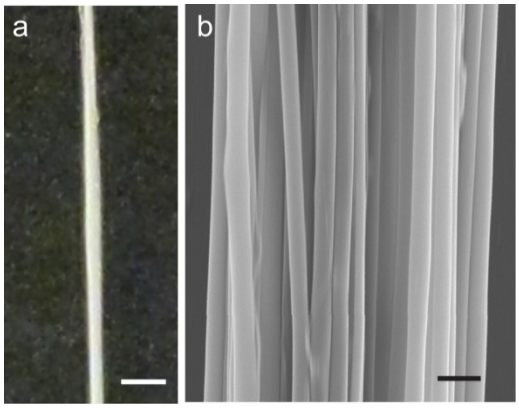

Figure 51. Aligned PVDF fiber bundle used to construct the coil (biotelemeter). (a) Photographic image of an aligned PVDF nanofiber bundle (scale: 3 mm). (b) SEM image of PVDF nanofirers in the bundle (scale: 1μm).

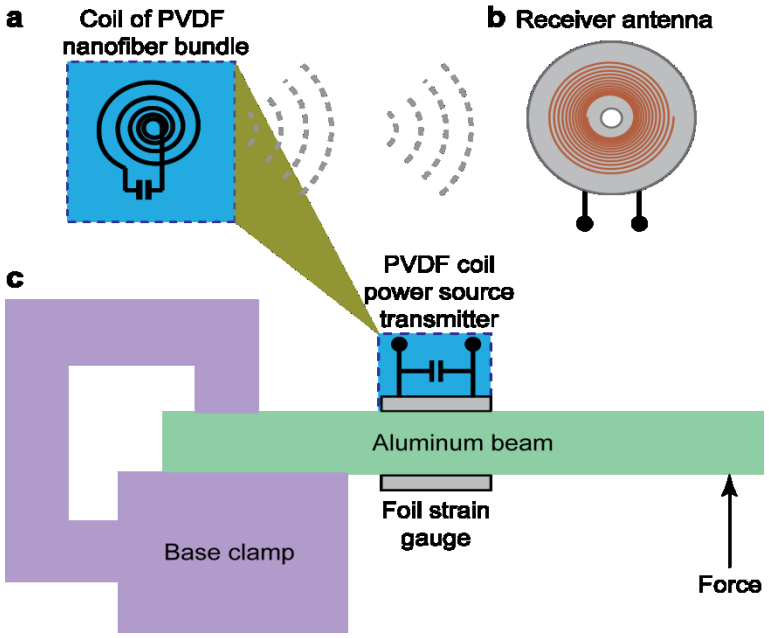

Figure 52. Schematic diagram of the test system for biotelemetry device. (a) Top view of the coil of PVDF nanofiber bundle. (b) Remote receiver antenna that receives the signal from the coil. (c) Experimental layout, where the aluminum beam (cantilever) brings the loading to the coil and foil strain gauge. See Appendix 1, Figures 58 to 59.

8.5 Data Collection System

The voltage output data from the foil strain gauge were received by a computer through an NI-9219 signal conditioner and NI data acquisition (DAQ) chassis; both from National Instruments (NI), to record voltage variation in response to the applied stress (Figure 55). To protect the foil strain gauge from a tension generated in connecting wires during bending, a metal plate was used as a mediator (Figure 55, upper left corner) attaching wires. The nanofiber coil generates an electrical current upon bending due to its piezoelectric property, internal resistance, creating an electronic field. The semi-concentric nanofiber flat spiral coil solenoid configuration accommodates a greater PVDF nanofiber concentration in a small area, creating a stronger concentrated field signal compared to a straight line bundle [206]. Although numerous energy harvesting concepts [221,223,224] are based on piezoelectric dynamics using appropriate sized capacitors for various frequency applications, our design is limited to fewer vibrations per time, requiring a large broad-band capacitance, 440μF, to extend the low frequency limit of a measurement in our system arrangement. As in higher frequency energy harvesting designs, our design utilizes the capacitor as a reservoir as well [221], but is sized for a lower frequency, approximately 0.1Hz, Figures 54 and 55.

Moreover, the spiral shape fits to work as a transmitter/antenna; thus, in addition to generating a voltage/current when deformed, it also acts as an antenna (transmitter) radiating a field signal. The field signal receiver antenna (Figure 52b), placed a distance away from the nanofiber spiral coil, is connected to a computer through a nano-voltmeter. Thus, the signal from the transmitter (i.e., PVDF nanofiber spiral coil) can be wirelessly acquired by the receiver and recorded by the computer.

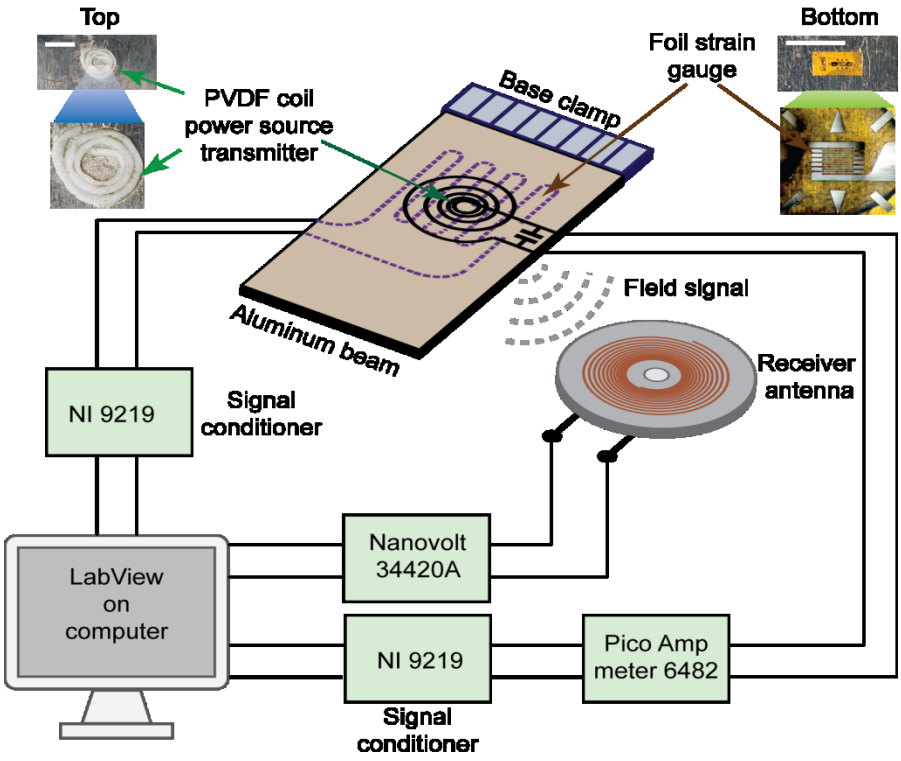

Figure 53. Schematic diagram of the testing system for the biotelemetry device showing connections of the PVDF nanofiber coil, receiving antenna, foil strain gauge, 440μF capacitor, and a computer equipped with a DAQ for data acquisition and analysis. The foil strain gauge is connected to the computer through an NI9219 signal conditioner. In additional to the wireless connection between the coil and receiving antenna, a direct wire connection is also established between the coil and the computer through a NI 9219 signal conditioner as a reference. The receiver antenna is connected to computer through a 34420A Agilant nanovolt meter. The aluminum beam is fixed on one end (base clamp) and is free on another end for bending. Photographic images show the PVDF coil affixed to the top surface of the aluminum beam (upper left corner, scale: 4 mm) and the foil strain gauge affixed to the bottom surface of the aluminum beam (upper right corner, scale bar: 2 mm) [226].

8.6 Voltage Signals at a Particular Loading and Distance

The cantilever beam affixed with the coil and foil strain gauge can be displaced either upward or downward to generate a voltage/current signal from the PVDF spiral coil that can be transmitted both wirelessly and through the connected wires, which were used to verify field transmission. With continuous alternative upward and downward bending of the cantilever beam, an alternating voltage/current would be obtained. However, we chose to deflect the beam by an applied load and then release the load, as an action of loading-and-releasing more closely resembles natural biological processes that happen in our body, for example, muscle motion during breathing, running, and heart beating.

With the periodic loading/releasing on the cantilever beam to deflect the free end of the cantilever by 0.5 mm, the signals generated in both the foil strain gauge and the coil were recorded (Figure 54). The voltage from the foil strain gauge was received through the direct wire connection (top panel), while the voltage generated in the coil was received by both direct wire connection (middle panel) and the wireless receiver antenna (bottom panel). The voltage signal from foil strain gauge was used as a control related to an equivalent strain produced through bending of the spiral coil. Electrodes used at spiral coil ends consisted of 30-gauge needles pushed into the bitter ends of PVDF spiral and held in place by PDMS. The results showed that the spiral coil served as both a sensor and an emitter and successfully transmitted the signal. The intensity of the signal received by the receiver antenna (in the range of 10E-7 – 10E-8 volt) is smaller than the same signal transmitted through the direct wire connection (in the range of 10E-4 – 10E-5 volt), which

is expected. The distance between the coil and the receiving antenna in this case was 7.5 cm.

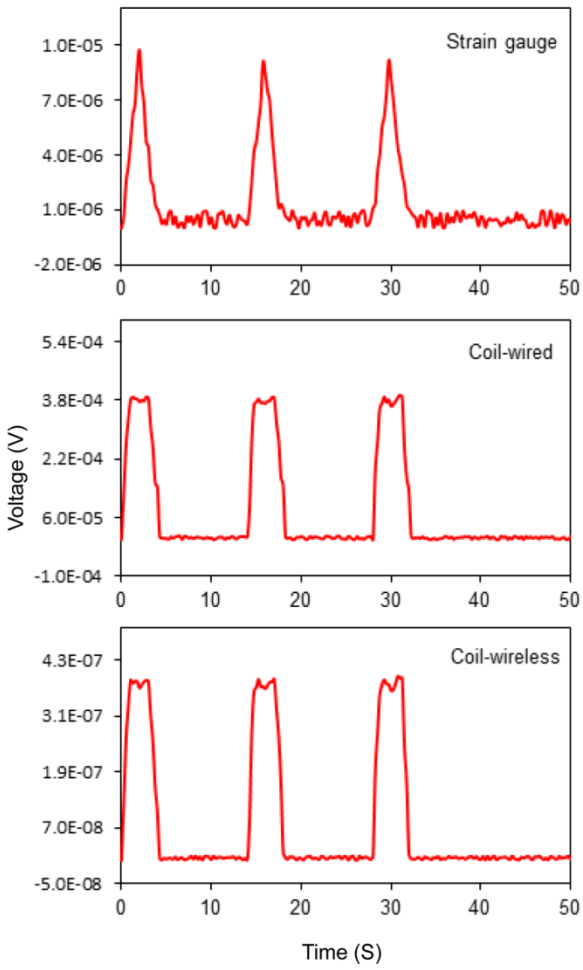

Figure 54. Voltage signal vs. time during periodic deflection of the free end of the cantilever beam by 0.5 mm. From top to bottom are the signals received from the foil strain gauge via hard wire to strain gage signal conditioner displaying peak voltage per time of beam deflection to beam release giving sawtooth profile, PVDF spiral coil via wire connection, and copper wire antenna coil via wireless communication with both displaying flatten top due to a large capacitive load, 440μF, in order to extend the very low-frequency limit of our measurement set-up.

It was also observed that the shape of the signal acquired from the foil strain gauge is triangular, whereas those acquired from the coil were trapezoidal. This might be due to the

difference in properties between the signal-generating materials. The foil strain gauge is made of metal and its resistance changes when it is deformed, causing the change in voltage signal. The coil, however, is made of PVDF nanofibers where polymeric molecular chains work as molecular batteries when it bends. Due to the polymeric properties, for a specific loading, each molecular chain could stretch to reach a plateau after reaching a particular deflection level, resulting in the trapezoidal shape in voltage signal.

8.7 Voltage Signal at Different Loadings

We further examined how the degree of cantilever deflection would affect the signal output. Figure 55 shows the signal output from the coil for cantilever deflected by 1 mm and 1.5 mm. The voltage output from the foil strain gauge is also shown (top row). For 1-mm deflection the intensities of the signal received from the coil by wire connection and wireless communication were in the ranges of 10E−4 – 10E−5 volt and 10E−7 – 10E−8 volt, respectively; both signals increased when the beam deflection was increased from 1.0 mm to 1.5 mm. Since the dimension of muscle movements in the body is mostly greater than 0.5 mm [204], this biotelemetry device can be useful for wirelessly monitoring these types of movements. Appendix 1, Figures 60 to 62, illustrate combined curve for all three deflections.

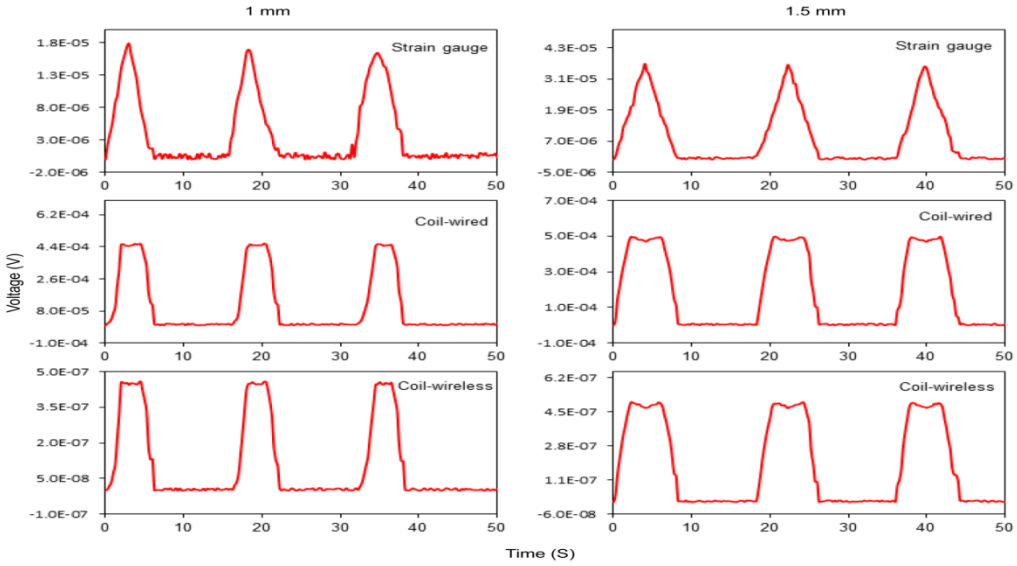

Figure 55. Voltage signal vs. time for periodic beam deflections by 1 mm (left column) and 1.5 mm (right column). From top to bottom, are the signals received from the foil strain gauge via hard wire to strain gage signal conditioner displaying peak voltage per time of beam deflection to beam release giving sawtooth profile, PVDF spiral coil by wire connection, and copper wire antenna coil by wireless communication with both displaying flatten top due to a large capacitive load, 440μF, in order to extend the very low-frequency limit of our measurement set-up.

The following Figure 56 illustrates the power output for the spiraled PVDF biosensor.

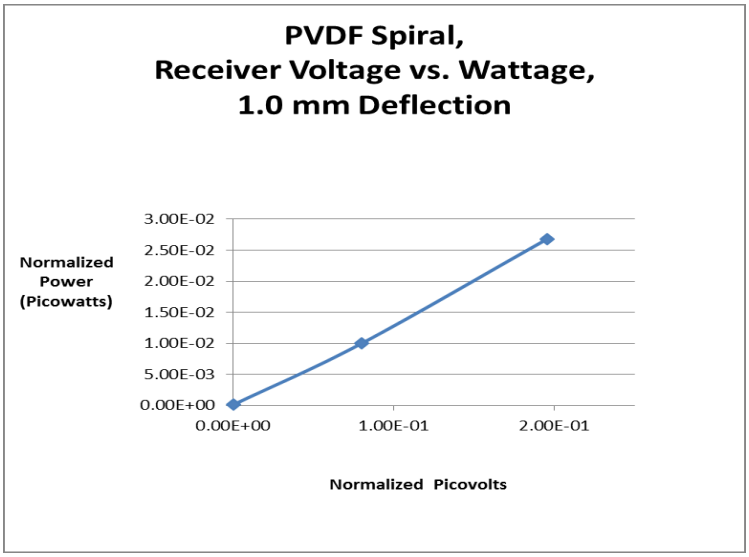

Figure 56. The power output in watts for the three different deflections of 0.5-mm, 1-mm, and 1.5-mm locations.

8.8 Voltage Signal at Different Distances Between the Transmitter and Receiver

We also examined how the distance between the transmitter (nanofiber coil) and receiver would affect the signal intensity. Figure 58 shows the intensities of the voltage signals received wirelessly from the nanofiber coil by the receiver antenna at distances of 7.5 cm, 15 cm, and 22.5 cm by deflecting the cantilever by 0.5 mm; the signal intensities were found to be 5.50 × 10E−7, 4.27 × 10E−7 and 4.07 × 10E−7, respectively. This result showed that the strength of the received signal decreased with the increase in the distance, but remained at the same order of magnitude. Thus the device can be used at greater distances if a secondary external electronic amplification is applied.

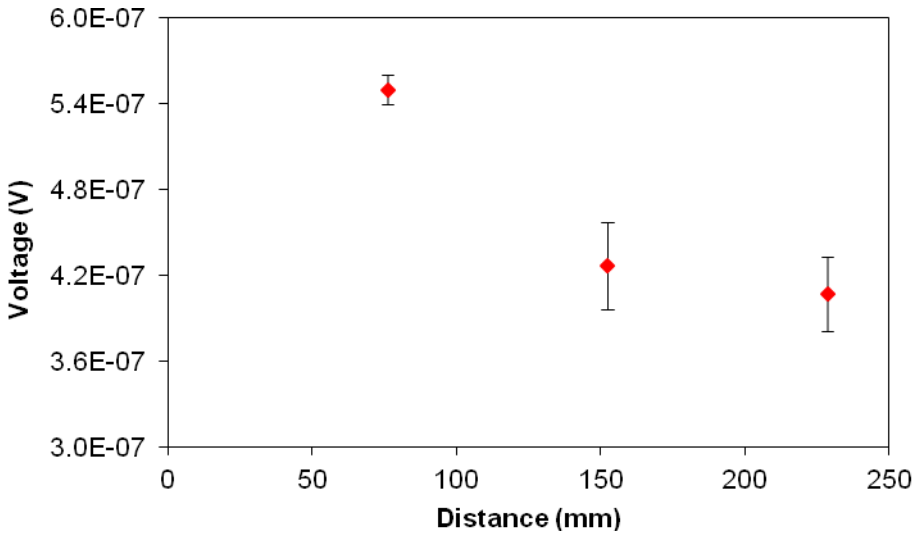

Figure 57. Voltage signal vs. distance between the nanofiber sensor coil and receiving antenna verses aluminum cantilever beam deflection of 0.5 mm.

CHAPTER 9: Conclusion

This thesis presented discussion on the basics of electrospinning and advanced it to another plateau by demonstrating a novel technique of electrospinning highly aligned nanofibers. The process began through the need to fabricate nanofibers for creating scaffolds promoting cellure immobilization and proliferation to verify the importance of highly aligned nanofibers. Although numerous journal papers have been published on aligned nanofibers and apparatus to do so, the work presented in this thesis has demonstrated that a better method using the Centrifugal Electro Spinner (CES), Figure 32, can create remarkably long, highly aligned nanofibers made from biocompatible organic polymers of PVDF-Tetra-FE (a piezoelectric material), chitosan, polyethene oxide (PEO), and poly-caprolactone (PCL). This work also demonstrated that highly or even appreciably aligned nanofibers can promote structural integrity allowing cell immobilization and subsequent cell proliferation. A number of cell types demonstrated that the novel electrospinning technology of using centrifugal force to create highly aligned nanofibers is very viable for supporting cell immobilization and proliferation. The collector design demonstrating best aligned nanofiber had vertical edge electrodes with an air gap between. As long as vertical edge electrodes were used, plates or wires, the electrospun nanofibers would align when using the centrifugal electrospinning technique. Properties of aligned nanofibers properties were characterized using nano-tensile tester developed in the lab, illustrating that linearly aligned nanofibers provide good structural strength qualities such as modulus of elasticity, ductility, and strength. Comparing collected fiber morphologies established that random nanofibers, which are easy to collect, not only

presented problems for cell proliferation but also exhibited poor structural strength in that random fibers were able to straighten during a tensile pull, wereas aligned fibers, being already straight, presented higher strength with crystallinity. The long, highly aligned PVDF piezoelectic nanofibers, similar to Figures 31,a,b,c, allowed the development of a novel piezoelectric energy harvesting biosensor capable of sensing and transmitting an electric signal to a remote receiver by using a small spiraled bundle of PVDF nanofibers and 440μF capacitor. The biocompatible biosensor output, Figure 57, is within limits of present day research that uses PVDF film [227] *in vivo*. Future research, based on current data results and power output, shows that the novel biosensor discussed in this thesis presents promising sensing and electrical transmission abiity. Its compact size, which can be drastically reduced in size from its current embryonic stage has demonstrated a patentable potential for *in vivo* applictions in the medical community.

APPENDIX 1

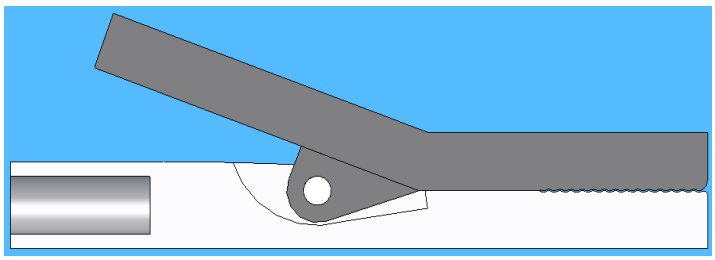

Figure 58a. Tensile tester “Titanium” clamp to hold fibers.

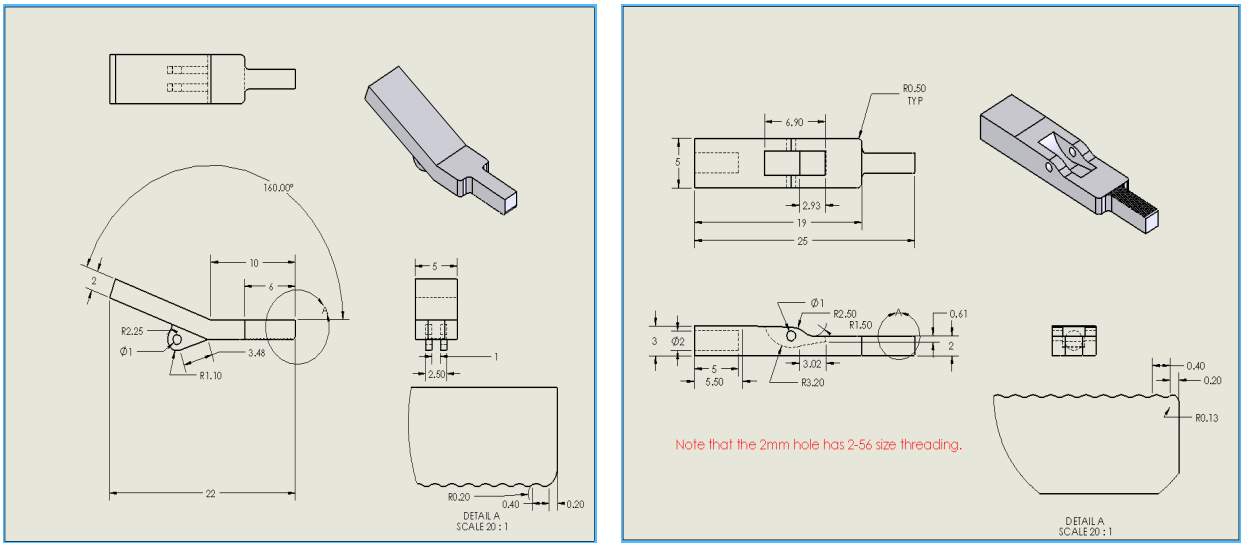

Figure 58b. Titanium nano-tensile tester specimen clamp. The device is spring loaded and also has a tightening screw to finger-tighten the specimen. 1000 grit sand paper is super glued to clamping surface, providing positive grabbing surface without crushing the fiber specimen.

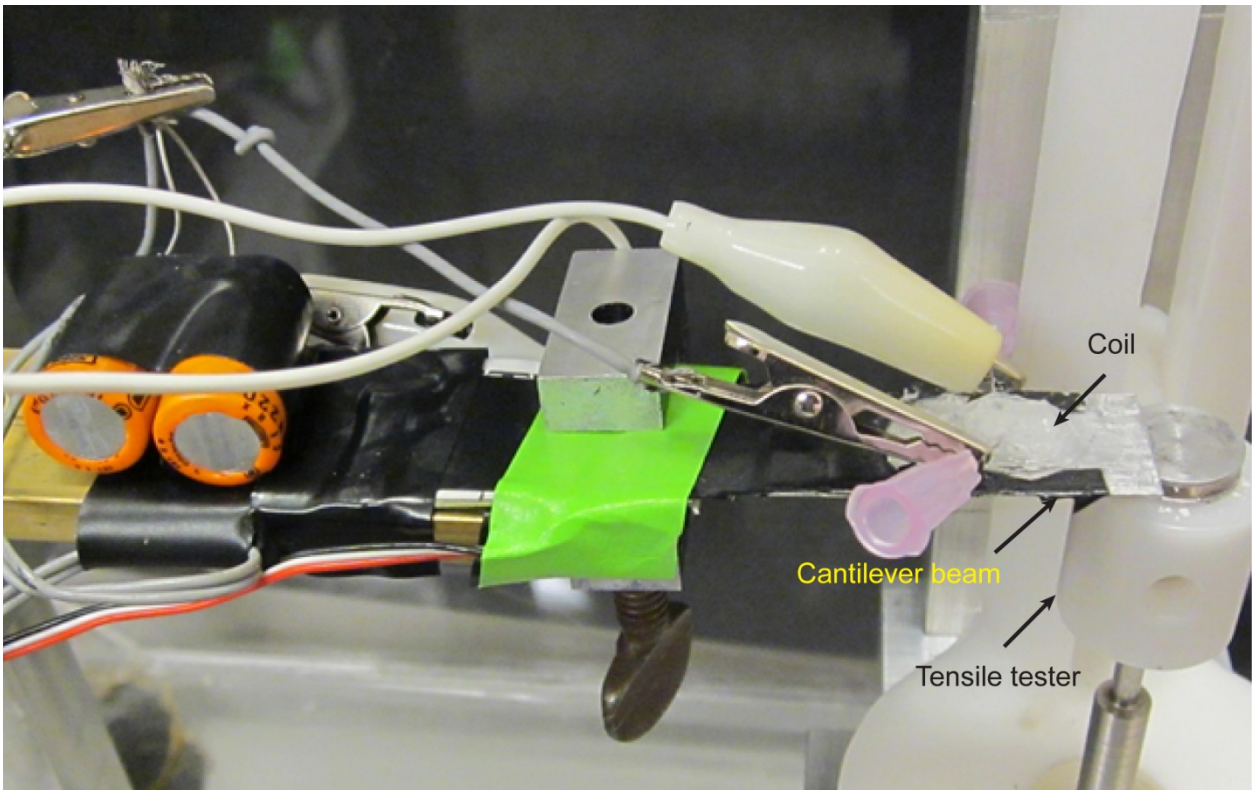

Figure 59. Photograph of the experimental set up (in part) showing the PVDF nanofiber coil encased in PDMS, cantilever beam and tensile/compression tester.

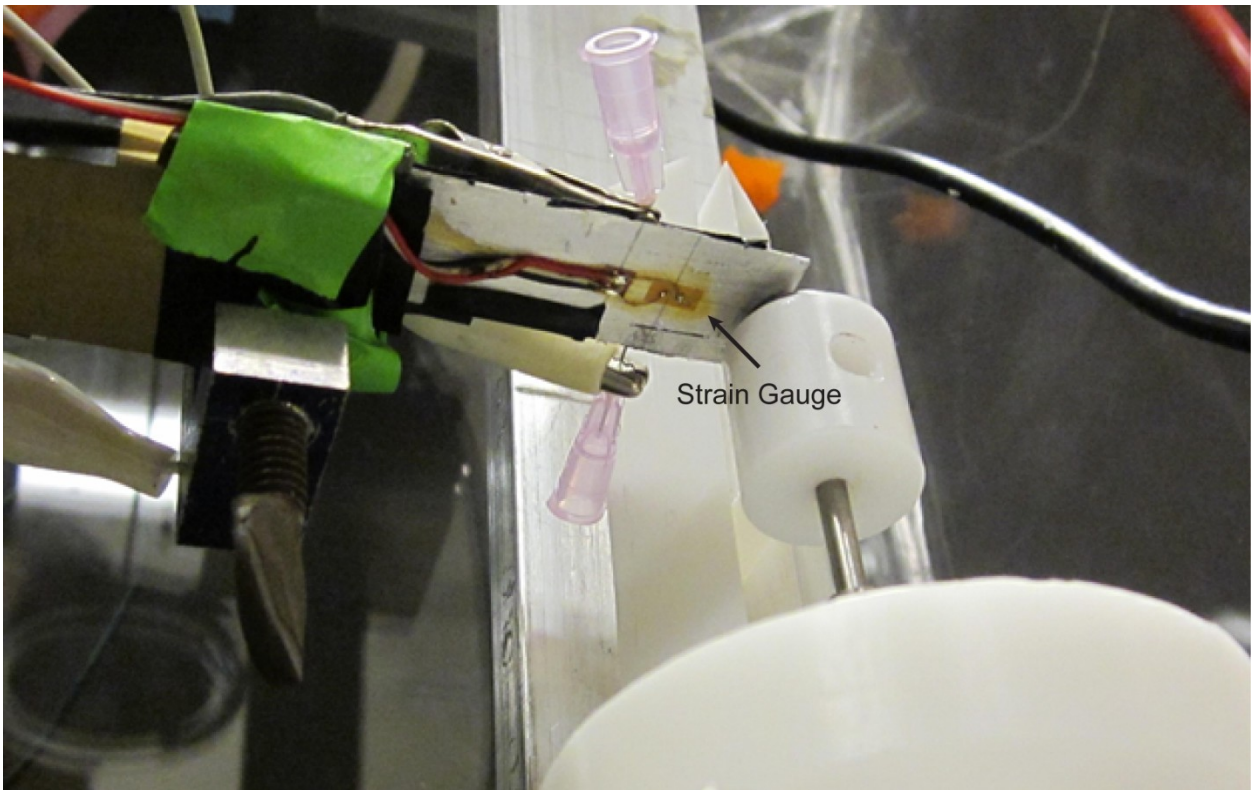

Figure 60. Photograph of the experimental apparatus (in part) showing the foil strain gauge affixed to the bottom surface of the cantilever beam and used as a control strain sensor.

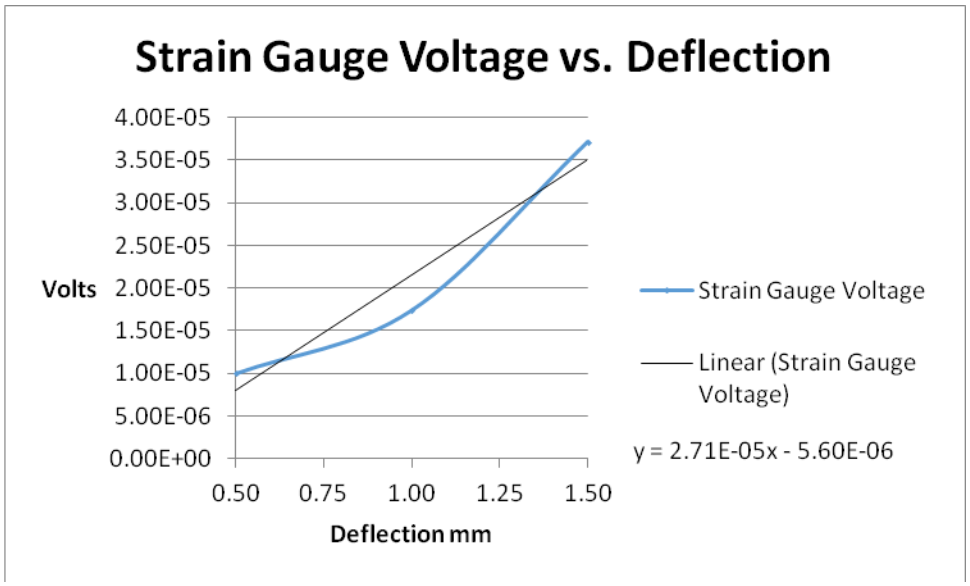

Figure 61. Strain gage voltage verses cantilever beam deflections of 0.5mm, 1.0mm, and 1.5mm.

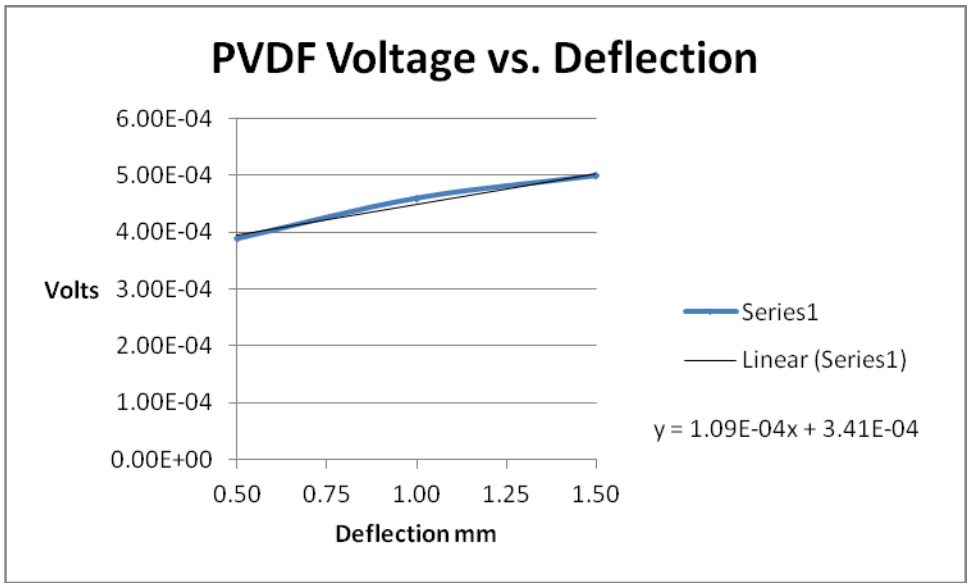

Figure 62. PVDF spiral coil voltage verses cantilever beam deflections of 0.5mm, 1.0mm, and 1.5mm.

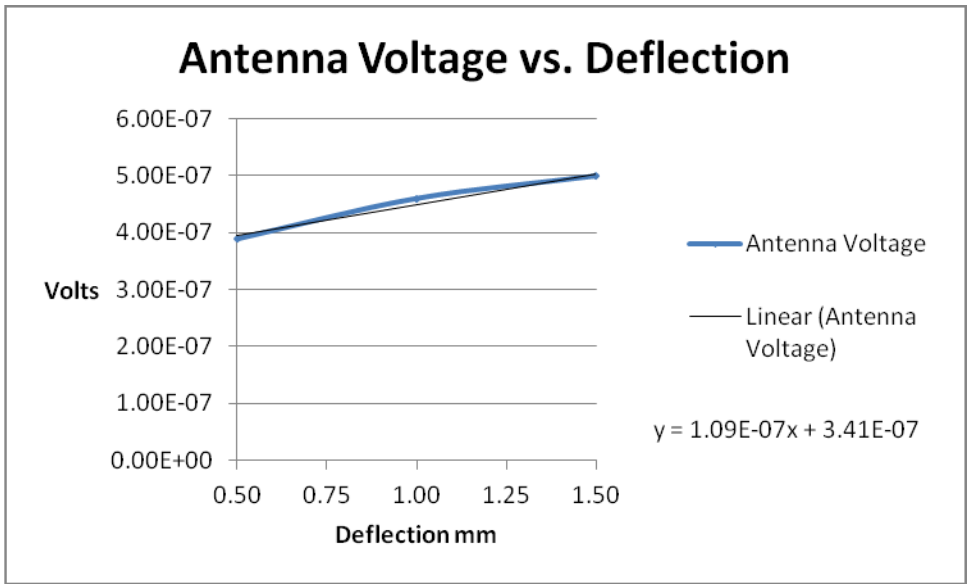

Figure 63. Voltages received by antenna verses cantilever beam deflections of 0.5mm, 1.0mm, and 1.5mm.

REFERENCES

1. Taylor, G., Disintegration of water droplets in an electric field, Proc. Roy. Soc. London 280: 383-397, 1964. Zeleny, J., The Electrical Discharge from Liquid Points, and a Hydrostatic Method of Measuring the Electric Intensity at Their Surfaces. Physical Review, 3, 1964.
2. Yu, JH., Fridrikh, SV., Rutledge, GC., The role of elasticity in the formation of electrospun fibers, Polymer,47,4789-4797, 2006.
3. Teo, WE., Ramakrishna, S., A review on electrospinning design and nanofiber assemblies, Nanotechnology, 17, R89-R106, 2006.
4. Services, U.D.o.H.a.H. 2020: A New Vision-A Future for Regenerative Medicine, 2006.
5. Lord Rayleigh, Philos. Mag., 14, 184-186, 1882.
6. Cloupeau, M., Foch, B P-,. Electrostatic spraying of liquids in cone-jet mode, Journal of Electrostatics, 22, 2, 135-159, 1989; K Hagiwaba, O Oji-Machi, K Ku, Jpn.,1, 699, 615, 1929.
7. Bhardwaj, N., Kundu, SC., Electrospinning: A fascinating fiber fabrication technique, Biotechnology Advances, Volume 28, Issue 3, Pages 325-347, May-June 2010.
8. Formhals, A., USPTO, 1,975,504, 1934.
9. Gunn, J., Zhang, M., Polyblend nanofibers for biomedical applications: perspectives and challenges, Trends in Biotechnology, 28, 189-197, 2010.
10. Simm, W., Gosling, K., Bonart, R., von Falkai, B., GB Patent Number 1346231, 1972.
11. Xie, J., MacEwan, M., Schwartz, A., Xia, Y., Electrospun nanofibers for neural tissue engineering, Nanoscale, 2, 35-44, 2010.
12. Doshi, J., Srinivasan, G., Reneker, D., Polymer News, 20, 206 – 207, 1995.
13. Gopal, R., Kaur, S., Feng, CY., Chan, C., Ramakrishna, S., Tabe, S., Matsuura, T., Electrospun nanofibrous polysulfone membranes aspre-filters: particulate removal, J. Membr. Sci., 289, 210-219, 2007; Subbiah, T., Bhat, GS., Tock, RW., Parameswaran, S., Ramkumar, SS., Electrospinning of Nanofibers, Journal of Applied Polymer Science, 96, 557-569, 2005.
14. Pawlowski, KJ., Belvin, HL., Raney, DL., Su, J., Harrison, JS., Siochi, EJ., Electrospinning of a micro-air vehicle wing skin, Polymer, 44, 1309-1314, 2003.

15. Gibson, PA., Schreuder-Gibson, HL., Rivin, D., Electrospun fiber mats: transport properties, Am Inst Chem Eng J., 45,190–195, 1999.

16. Kim, C., Kim, JS., Kim, SJ., Lee, WJ., Yang, KS., Supercapacitors prepared from carbon nanofibers electrospun from polybenzimidazol, J. Electrochem. Soc., 151, A769-A773, 2004.

17. Li, WJ., Laurencin, CT., Caterson, EJ., Tuan, RS., Ko, FK., Electrospun nanofibrous structure: a novel scaffold for tissue engineering, J. Biomater. Res.,60,613-621,2002.

18. Li, M., Mondrinos, MJ., Gandhi, MR., Ko, FK., Weiss, AS., Lelkes, PI., Electrospun protein fibers as matrices for tissue engineering, Biomaterials, 26, 5999-6008, 2005.

19. Buttafuco, L., Kolkman, NG., Engbers-Buijtenhuijs, P., Poot, AA., Dijkstra, PJ., Vermes, I., Feijen, J., Electrospinning of collagen and elastin for tissue engineering applications, Biomaterials, 27, 724-734, 2006.

20. Kidoaki, S., Kwon, IK., Matsura, T., Mesoscopic spatial designs of nano- and microfiber meshes for tissue-engineering matrix and scaffold based on newly devised multi-layering and mixing electrospinning techniques, Biomaterials, 26, 37-46, 2005.

21. Xu, CY., Inai, R., Kotaki, M., Ramakrishna, S., Aligned biodegradable nanofibrous structure: a potential scaffold for blood vessel engineering, Biomaterials, 25, 877-886, 2004.

22. Vaz, CM., van Tuiji, S., Bouten, CVC., FPT Baaijens, Design of scaffolds for blood vessel tissue engineering using a multi-layering electrospinning technique, Actabiomaterialia, 1, 575-582, 2005.

23. Matthews, JA., Wnek, GE., Simpson, DG., Bowlin, GL Electrospinning of collagen nanofibers, Biomacromolecules, 3, 232-238, 2002.

24. Mo, XM., Xu, CY., Kotaki, M., Ramakrishna, S., Electrospun P(LLA-CL) nanofiber: a biomimetic extracellular matrix for smooth muscle cell and endothelial cell proliferation. Biomaterials, 25,1883-1890, 2004.

25. Yang, F., Murugan, R., Wang, S., Ramakrishna, S., Electrospinning of nano/micro scale poly(L-lactic acid) aligned fibers and their potential in neural tissue engineering, Biomaterials, 26, 2603-2610, 2005.

26. Bini, TB., Gao, S., Tan, TC., Wang, S., Lim, A., Hai, LB., Ramakrishna, S., Electrospun poly(L-lactide-co-glycolide) biodegradable polymer nanofibre tubes for peripheral nerve regeneration, Nanotechnology,15,1459-1464, 2004.

27. Yoshimoto, H., Shin, YM., Terai, H., Vacanti, JP., A biodegradable nanofiber scaffold by electrospinning and its potential for bone tissue engineering, Biomaterials, 24,2077-2082, 2003.

28. Muzzarelli, R., Chitins and chitosans for the repair of wounded skin, nerve, cartilage and bone, Carbohydrate Polymers 76, 167-182, 2009.

29. Zhang, J., Xia, W., Liu, P., Cheng, Q., Tahirou, T., Gu, W., Li, B., Chitosan Modification and Pharmaceutical/Biomedical Applications, Marine Drugs, 8,1962,2010.

30. Heineken, FG., Skalak, R., Tissue Engineering, A Brief Overview, Journal of Biomechanical Engineering, 113, 111-112, 1991.

31. Bhardwaj, N., Kundu, SC., Electrospinning: a fascinating fiber fabrication technique, Biotechnology Advances, 28, 3, 325-347, 2010.

32. Feng, JJ., The stretching of an electrified non-Newtonian jet: A model for electrospinning, Phys. Fluids, 14,11, 3912-3926, 2002.

33. Ondarcuhu, T., Joachim, C., Drawing a single nanofiber over hundreds of microns, Europhys. Lett., 42,2, 215-220, 1998.

34. de Moel, K., Ekenstein, GORA., Nijland, H., Polushkin, E., ten Brinke, G., Ontto Maki, R., Ikkala, O., Polymeric nanofibers prepared from self organized supramolecules, Chem. Mater., 13, 12, 4580-4583, 2001.

35. Ma, PX., Zhang, R., Synthetic nano-scale fibrous extracellular matrix, J. Biomed. Mater. Res., 46,1, 60-72, 1999; Witte, D., Dijkstra, PJ., Berg, JWA., Feijen, J., Phase separation process in polymer solutions in relation to membrane formation, J. Membr. Sci., 117, 1, 199.

36. Lyons, J., Ko, FK., Pastore, C Developments in melt-spinning of thermoplastic polymers, Abstr. Pap. Am. Chem. Soc., 226, U400-401 300-POLY; Lyons, J., Li, C., Ko, F., Melt-electrospinning part-I: processing parameters and geometric properties, Polymer, 45, 7597-7603, 2004.

37. Higuera, FJ., Flow rate and electric current emitted by a Taylor cone, J. Fluid Mech. (2003), vol. 484, pp. 303–327, 2003; Chakarvarti, SK., Vetter, J., Template synthesis-membrane based technology for generation of nano-/micro materials: a review, Radiat. Meas., 29, 149, 1998.

38. Rutledge, G., Fridrikh, S., Formation of fibers by electrospinning, Advanced Drug Delivery Reviews, 59, 1384-1391, 2007.

39. Seidlits, SK., Lee, JY., Schmidt, CE., Nanostructured scaffolds for neural Applications, Nanomedicine, 3, 183,117, 2008.

40. Yang, F., Morgan, R., Wang, S., Ramakrishna, S., Electrospinning of nano/micro scale poly(L-lactic acid) aligned fibers and their potential in neural tissue engineering, Biomaterials, 26, 2603-2610, 2005.

41. Bhardwaj, N., Kundu, S., Electrospinning: A fascinating fiber FabricationTechnique, Biotechnology Advances, 2010.

42. Larrondo, L., Manley, RS., Electrostatic fiber spinning from polymer melts. II., Examination of the flow field in an electrically driven jet, J. Polym. Sci. Pol. Phys., 19, 921-932, 1981.

43. Xing, ZC., Han, SJ., Shin, YS., Kang, IK., Fabrication of biodegradable polyester nano-composites by electrospinning for tissue engineering, Journal of Nano Materials, 2011, 929378,2011.

44. Schiffman, J., Schauer, CA., Review: Electrospinning of Biopolymer Nanofibers and their Applications, Polymer Reviews 48, 317-352, 2008.

45. Gunatillake, PA., Adhikari, R., Biodegradable synthetic polymers for tissue engineering, European Cells and Materials, 5, 1-16, 2003.

46. Alfrey Jr, T., Goldberg, AI., Price, JA., Dilute-solution viscosity poly-methyl methacrylate and a methyl methacrylate styrene copolymer, Journal of Collide Science, 5, 3,251-259, June 1950.

47. Frantz, C., Stewart, K., Weaver, V., The extracellular matrix at a glance, Journal of Cell Science,123, 4195-4200, 2010.

48. Schiffman, J., Schauer, C., A Review: Electrospinning of Biopolymer Nanofibers and their Applications, Polymer Reviews ,48, 317-352, 2008.

49. Teo, WE., Ramakrishna, S., A reviewon electrospinning design and nanofiber assemblies, Nanotechnology 17, 14, 89, 2006.

50. Lee, KS., El-Sayed, MA., J. Phys. Chem., B, 109, 20331-20338, 2005; WU Huynh, JJ Dittmer, AP Alivisatos, Science, 295, 2425-2427, 2002.

51. Thompson, C., Chase, G., Yarin, G., Reneker, DA., Effects of parameters on nanofiber diameter determined from electrospinning model, Polymer 48, 6913-6922, 2007; Lu C., Chen P., Li J., Zhang,Y., Polymer, Vol. 47, 915-921, 2006; Luo, C., Nangrejo, M., Edirisinghe, M., A novel method of selecting solvents for polymer electrospinning, Polymer,2010.

52. Baumgarten, PK., Electrostatic spinning of acrylic microfibers, J. Colloid Interf. Sci., 36, 75-79, 1971.

53. Kessick, R., Fenn, J., Tapper, G., The use of AC potentials in electrospraying and electrospinning processes, Polymer, 45, 2981-2984, 2004.

54. Taylor, G., Disintegration of water droplets in an electric field, Proc. R. Soc. Of London, 280, 383–397, 1964.

55. Khan, WS., Asmatulu, R., Eltabey, MM., Dielectric properties of electrospun PVP and PAN Nanocomposite fibers at various temperatures, J. Nanotechnol. Eng. Med., 1, 4, 041017, Nov 2010.

56. Reneker, DH., Yarin, AL., Fong, H., Koombhongse, S., Bending instability of electrically charged liquid jets of polymer solutions in electrospinning, J. Appl. Phys., 87, 4531, 2000.

57. Yarin, AL., Koombhongse, S., Reenter, DH., Bending instability in electrospinning of Nanofibers, J. Appl. Phys. 89, 3018, 2001; Feng, JJ., The stretching of an electrified non-Newtonian jet: A model for electrospinning, Physics of Fluids,14, 11, 3912-3926, November 2002.

58. Tascan, M., Vaughan, EA., Effects of fiber denier, fiber cross-sectional shape and fiber density on acoustical behavior of vertically lapped nonwoven fabrics, Journal of Engineered Fibers and Fabrics, 3, 2, 32-38, 2008.

59. Nieh, S., Nuguyen, T., Effects of humidity, conveying velocity, and particle size on electrostatic charges of glass beads in a gaseous suspension flow, Journal of Electrostatics, 21, 99-114, 1988.

60. Casper, CL., Stehens, JS., Tassi, NG., Chase, DB., Rabolt, JF., Controlling surface morphology of electrospun polystyrene fibers: Effect of humidity and molecular weight in the electrospinning process, Macromolecules, 37, 573-578, 2004.

61. Zhong, X., Kim, K., Fang, D., Ran, S., Hsiao, BS., Chu, B., Structure and process relationship of electrospun bio-absorbable nanofiber membranes, Polymer, 43, 4403-4412, 2002.

62. Jarusuwannapoom, T., Hongrojjanawiwat, W., Koombhongse, P., Rangkupan, R., Supaphol, P., Effect of solvents on electro-spinnability of polystyrene solutions and morphological appearance of resulting electrospun polystyrene fibers, Euro. Polym. J., 41, 409-421, 2005.

63. Wannatong, L., Sirivat, A., P Supaphol, Effects of solvents on electrospun polymeric fibers: preliminary study on polystyrene, Polym. Int., 53, 1851-1859, 2004.

64. Bhat, PP., Appathurai, S., Harris, MT., Pasquali, M., Mckinley, GH., Basaran, OA., Formation of beads-on-a-string structures during break-up of viscoelastic filaments, Nature Physics, 6, 625-631, 2010.

65. Mo, X., Xu, CY., Kotaki, M., Ramakrishna, S., Electrospun P(LLA-CL) nanofiber: a biomimetric extracellular matrix for smooth muscle cell and endothelial cell proliferation, Biomaterials, 25, 1883-1890, 2004.

66. Zeng, J., Xu, X., Chen, X., Liang, Q., Bian, X., Yang, L., Jing, X., Biodegradable electrospun fibers for drug delivery, J. Control. Release, 92, 227-231, 2003.

67. Thompson, C., Chase, G., Yarin, A., Reneker, D., Effects of parameters on nanofiber diameter determined from electrospinning model, Polymer 48, 6913-6922, 2007.

68. Son, WK., Youk, JH., Lee, TS., Park, WH., Electrospinning of ultrafine cellulose acetate fibers: studies of a new solvent system and deacetylation of ultrafine cellulose fibers, J. Polym. Sci. Pt. B-Polym. Phys., 42, 5-11, 2004.

69. Lu, C., Chen, P., Li, J., Zhang, Y., Polymer, 47, 915-921, 2006; Uyar, T., Besenbacher, F., Electrospinning of uniform polystyrene fibers: The effect of solvent conductivity, Polymer, 49, 5336-5343, 2008.

70. Deitzel, JM., Kleinmeyer, JD., Hirvonen, Tan, JK NCB., Control deposition of electrospun poly(ethylene oxide) fibers, Polymer, 42, 8163-8170, 2001; Deitzel, JM., Kleinmeyer, JD., Harris, D., Tan, NCB., The effect of processing variables on the morphology of electrospun nanofibers and textiles, Polymer, 42, 261-272, 2001; Deitzel, JM., Kosik, W., McKnight SH., Tan, NCB., DeSimone, JM., Crette, S., Electrospinning of polymer nanofibers with specific surface chemistry, Polymer, 43, 1025-1029, 2002.

71. Li, D., Xia, Y., Direct fabrication of composite and ceramic hollow nanofibers by electrospinning, NanoLetters, 4, 933-938, 2004; Li, D., McCann, JT G., Xia, Y., Collecting electrospun nanofibers with patterned electrodes, NanoLetters, ASAP, 2005.

72. Fallahi, D., Rafizadeh, M., Mohammadi, N., Vahidi, B., Effect of applied voltage on surface and volume charge density of the jet in electrospinning of polyacrylonitrile solutions, Polymer Engineering and Science, 50, 7, 1372–1376, July 2010.

73. Badrossamay, MR., Mollwee, HA., Gross, JA., Parker, KK .,Nanofiber assembly by rotary jet spinning, Nano Letters, 2257-2261, May, 21, 2010.

74. Reznik, S N., Yarin, AL., Theron, A., Zussman, E., J. Fluid Mech., 516, 349-377, 2004; Cloupeau, M., Prunet-Foch, B., J. Electrost., 22, 135-159, 1989; Yarin, AL., Koombhongse, S., Reneker, DH., J. Appl. Phys., 90, 4836-4846, 2001.

75. Krishnappa, RVN., Desai, K., Sung, CM., Morphological study of electrospun polycarbonates as a function of the solvent and processing voltage, J. Mater. Sci., 38, 2257-2365, 2003.

76. Demir, MM., Yilgor, I., Yilgor, E., Erman, B., Electrospinning of polyurethane fibers, Polymer, 43, 3303-3309, 2002.

77. Buchko, CJ., Chen, LC., Shen, Y., Martin, DC., Processing and microstructural characterization of porous biocompatible protein polymer thin films, Polymer, 40, 7397-7407, 1999.

78. Lee, JS., Choi, KH., Ghim, HD., Kim, SS., Chun DH.,, Kim, HY., Lyoo, WS., Role of molecular weight of atactic poly(vinyl alcohol) (PVA) in the structure and properties of PVA nanofabric prepared by electrospinning, J. Appl. Polym. Sci., 93, 1638-1646, 2004.

79. Zhao, SL., Wu, XH., Wang, LG., Huang Y.,, Electrospinning of ethyl-cyanoethyl cellulose/tetrahydrofuran solutions, J. Appl. Polym. Sci., 91, 242-246, 2004; Zhao, SL., Wu, XH., Wang, LG., Huang, Y., Electrostatically generated fibers of ethyl-cyanoethyl cellulose, Cellulose, 10, 405-409, 2003.

80. Mit-Uppatham, C., Nithitanakul, M., Supaphol, P,. Ultrafine Electrospun Polyamide-6 Fibers: Effect of Solution Conditions on Morphology and Average Fiber Diameter, Macromolecular Chemistry and Physics, 205, 2327-2338, 2004.

81. Srnivasarao, M., Collings, D., Philips, A., Patel, C,. Three-dimensionally ordered array of air bubbles in a polymer film, Science, 292, 79-83, 2001.

82. Megelski, S., Stephens, JS., Chase, DB., Rabolt, JF., Micro- and nanostructured surface morphology on electrospun polymer fibers, Macromolecules, 35, 8456, 2002.

83. Bhattarai, N., Edmondson, D., Veiseh, O., Matsen, FA., Zhang, M., Electrospun chitosan-based nanofibers and their cellular compatibility, Biomaterials, 26, 6176, 2005; Jayaraman, K., Kotaki, M., Zhang, YZ., Mo, XM., Ramakrishna, S., Recent advances in polymer nanofibers, J. Nanosci. Nanotechno., 4, 52-65, 2004; Ellis-Behnke, RG., Liang, YX., You, SW., Tay, DKC., Zhang, S., So, KF., Schneider, GE,. Nano neuro knitting: Peptide nanofiber scaffold for brain repair and axon regeneration with functional return of vision, PNAS, vol. 103, no. 13, 5054-5059, March 28, 2006.

84. Gunatillake, PA., Adhikari, R., Biodegradable synthetic polymers for tissue engineering, European Cells and Materials, 5, 1-16, 2003; Walton, M., Cotton, NJ., Long Term in vivo Degradation of Poly-L-lactide (PLLA) in Bone, Journal of Biomaterials Applications, 21:395, 2007.

85. Zhang, SG., Nature Biotechnology, 22, 151, 2004; Zhang, SG., Nature Biotechnology, 21, 1171, 2003; Huang, ZM., Zhang, YZ., Kotaki, M., Ramakrishna, S., Composites Science and Technology, 63, 2223, 2003; Zhang, R., Ma, PX., J. Biomed. Mater. Res., 52, 430, 2000.

86. Frenot, A., Chronakis, IS., Polymer nanofibers assembled by electrospinning, Current Opinion in Colloid and Interface Science, 8, 64, 2003; Elsdale, T., Bard, J.,

Collagen substrata for studies on cell behavior, J. Cell. Biol., 54, 626, 1972; ED Hay, FASEB J., 13 Suppl. 2:S281-3, 1999.

87. Rho, KS., Jeong, L., Lee, G., Seo, BM., Park, YJ., Hong, SD., Roh, S., Cho, JJ., Park, WH., Min, BM., Electrospinning of collagen nanofibers: Effects on the behavior of normal human keratinocytes and early-stage wound healing, Biomaterials, 27, Issue 8, Pages 1452-1461, March 2006.

88. Laurencin, CT., Ambrosio, AM., Borden, MD., Cooper Jr. JA., Tissue Engineering: Orthopedic Applications., Annu. Rev. Biomed. Eng., 1, 19, 1999; Teixeira, AI., Abrams, GA., Bertics, PJ., Murphy, CJ., Nealey, PF., Epithelial contact guidance on well-defined micro- and nanostructured substrates, J. Cell. Sci.,116,1881, 2003.

89. Li, WJ., Laurencin, CT., Caterson, EJ., Tuan, RS., Ko, FK., Electrospun nanofibrous structure: A novel scaffold for tissue engineering, Journal of Biomedical Materials Research, 60, 613, 2002.

90. Zhang, Y., Lim, CT., Ramakrishna, S., Huang, ZM., Recent development of polymer nanofibers for biomedical and biotechnological applications, J. Mater. Sci. Mater. Med.,16, 933, 2005.

91. Suh, JKF., Matthew, HWT., Application of chitosan-based polysaccharide biomaterials in cartilage tissue engineering: a review, Biomaterials, 21, 2589, 2000; Hutmacher, DW., Goh, JC., Teoh, SH., An introduction to biodegradable materials for tissue engineering applications, Ann. Acad. Med. Singapore, 30, 183, 2001.

92. Hsu, SH., Whu, SW., Hsieh, SC., Tsai, CL., Chen DC, Tan, TS., Evaluation of Chitosan-alginate-hyaluronate Complexes Modified by an RGD-containing Protein as Tissue-engineering Scaffolds for Cartilage Regeneration, Artificial Organs, 28, 693, 2004.

93. M., Xu, X., A review on biodegradable polymeric materials for bone tissue Journal of Materials Science, Volume 44, Number 21, 5713-5724, 2007.

94. Kumar, MNVR., A Review of Chitin and Chitosan Applications, Polymer, 46, 1, 1-27, 2000.

95. Shield, KJ., Beckman, MJ., Bowlin, GL., Wayne, JS., Mechanical Properties and Cellular Proliferation of Electrospun Collagen Type II, Tissue Engineering, 10, 1510, 2004; Mo, XM., Xu, CY., Kotaki, M., Ramakrishna, S., Biomaterials, 25, 1883, 2004.

96. Temenoff, JS., Mikos, AG., Review: tissue engineering for regeneration of articular cartilage, Biomaterials, 21, 431, 2000; Yang, S., Leong, KF., Du, Z., Chua, CK., The Design of Scaffolds for Use in Tissue Engineering. Part I. Traditional Factors, Tissue Engineering, 7, 679, 2001.

97. Iozzo, RV., Murdoch, AD., Proteoglycans of the extracellular environment: clues from the gene and protein side offer novel perspectives in molecular diversity and function Faseb Journal, 10, 598, 1996; Johnson, FA., Craig, DQ., Mercer, AD., Characterization of the Block Structure and Molecular Weight of Sodium Alginates ,J. Pharm. Pharmacol., 49, 639, 1997; Hashimoto, T., Suzuki, M., Tanihara, Y., Kakimaru, Y., Suzuki, K., Development of alginate wound dressings linked with hybrid peptides derived from laminin and elastin, Biomaterials, 25, 1407, 2004.

98. Li, Z., Zhang, M., Chitosan–alginate as scaffolding material for cartilage tissue engineering, J. Biomed. Mater. Res., A, 75, 485, 2005.

99. Alsberg, E., Anderson, KW., Albeiruti, A., Franceschi, RT., Mooney, DJ., Cell-interactive Alginate Hydrogels for Bone Tissue Engineering, J. Dent. Res., 80, 2025, 2001.

100. Yang, J., Chung, TW., Nagaoka, M., Goto, M., Cho, CS., Akaike, T., Hepatocyte-specific porous polymer-scaffolds of alginate/galactosylated chitosan sponge for liver-tissue engineering, Biotechnology Letters, 23, 1385, 2001.

101. Dar, A., Shachar, M., J Leor, S Cohen, Optimization of cardiac cell seeding and distribution in 3D porous alginate scaffolds, Biotechnology and Bioengineering, 80, 305, 2002.

102. Hartgerink, JD., Beniash, E., Stupp, SI., Peptide-amphiphile nanofibers: A versatile scaffold for the preparation of self-assembling materials,Proceedings of the National Academy of Sciences of the United States of America, 99, 5133, 2002.

103. Wan, YQ., He, JH., Wu, Y., Yu, JY., Vibrorheolgical Effect on Electrospun Polyacrylonitrile (PAN) Nanofibers, Materials Letters, 60, 3296-3300, 2006.

104. Amiji, M., Park, K., Surface modification of polymeric biomaterials with poly(ethylene oxide), albumin, and heparin for reduced thrombogenicity, J. Biomater. Sci. Polym. Ed., 4, 217,1993; Park, K., Shim, HS., Dewanjee, MK., Eigler, NL., In vitro and in vivo studies of PEO-grafted blood-contacting cardiovascular prostheses, J. Biomater. Sci. Polym. Ed., 11, 1121, 2000.

105. Huang, ZM., Zhang, YZ., Kotaki, M., Ramakrishna, S., A review on polymer nanofibers by electrospinning and their applications in nanocomposites, Compos. Sci. Technol., 63, 2223-2253, 2003.

106. Ohkawa, K., Cha, DI., Kim, H., Nishida, A., Yamamoto, H., Electrospinning of chitosan, Macromolecular Rapid Communications, 25, 1600-1605, 2004.

107. Duan, B., Dong, CH., Yuan, XY., Yao, KD., Electrospinning of chitosan solutions in acetic acid with poly(ethylene oxide), Journal of Biomaterials Science-Polymer Edition 15, 797-811, 2004.

108. Costa,KD., Lee, EJ., Holmes, JW., Creating alignment and anisotropy in engineered heart tissue: Role of boundary conditions in a model three-dimensional culture system, Tissue Engineering 9, 567-577, 2003.

109. Matthews, JA., Wnek, GE., Simpson, DG., Bowlin, GL., Electrospinning of collagen nanofibers, Biomacromolecules, 3, 232-238, 2002.

110. Li, D., Wang, YL., Xia, YN., Electrospinning of polymeric and ceramic nanofibers as uniaxially aligned arrays, Nano Letters, 3, 1167-1171, 2003.

111. Zussman, E., Theron, A., Yarin, AL., Formation of nanofiber crossbars in electrospinning, Appl. Phys. Lett., 82, 973-975, 2003.

112. Bhattarai, SR., Bhattarai, N., Yi, HK., Hwang, PH., Cha, DI., Kim, HY., Novel biodegradable electrospun membrane: scaffold for tissue engineering, Biomaterials, 25, 2595-2602, 2004.

113. Elsdale, T., Bard, J., Collagen substrata for studies on cell behavior, J. Cell. Biol., 54, 626-37, 1972.

114. Edmondson, D., Bhattarai, N., Soumen, J., Kim, A., Zhang, M., Design and evaluation of a nanoscale differential tensile testing device for nanofibers, Applied Physics Letters 94, 103101, 2009.

115. Sharpe, WN., Murray Lecture Tensile Testing at the Micrometer Scale: Opportunities in Experimental Mechanics, Society for Experimental Mechanics, Vol.43, No.3, September 2003.

116. Mathew, HWT., Salley, SO., Peterson, WD., Klein, MD., Complex coercervate microcapsules for mammalian cell culture and artificial organ development, Biotechnology Progress, 9, 510-519,1993.

117. Zielinski, BA., Aebischer, P., Chitosan as a matrix for mammalian cell encapsulation, Biomaterials, 15, 1049-1056, 1994.

118. Takahashi, T., Takayama, K., Machida, Y., Nagai, T., Characteristics of poly-ion complexes of chitosan with sodium alginate and sodium polyacrylate, Int. J. Pharm., 61, 35-41, 1990.

119. Li, W., Jiang, YJ., Tuan, RS., Chondrocyte phenotype in engineered fibrous matrix is regulated by fiber size, Tissue Eng., 12:1775–1785, 2006.

120. Nain, AS., Phillippi, JA., Sitti, M., MacKrell, J., Campbell, PG., Amon, C., Control of cell behavior by aligned micro/nanofibrous biomaterial scaffolds fabricated by spinneret-based tunable engineered parameters (STEP) technique, Small, 4, 1153–1159, 2008.

121. Sun, T., Norton, D., Vickers, N., McArthur, SL., Neil, SM., Ryan, AJ., Haycock, JW., Development of a bioreactor for evaluating novel nerve conduits, Biotechnol. Bioeng., 99, 1250– 1260, 2008.

122. Bini, TB., Gao, S., Wang, S., Ramakrishna, S., Poly(L-lactide-co-glycolide) biodegradable microfibers and electrospun nanofibers for nerve tissue engineering: an in vitro study, J. Mater. Sci., 41, 6453–6459, 2006.

123. Yu, TT., Shoicet, MS., Guided cell adhesion and outgrowth in peptide-modified channels for neural tissue engineering, Biomaterials, 26, 1507, 2005.

124. Pham, QP., Sharma, U., Mikos, AG., Electrospinning of Polymeric Nanofibers for Tissue Engineering Applications: A Review, Tissue Engineering, 12, 1197, 2006.

125 Dzenis, Y., Spinning Continuous Fibers for Nanotechnology, Science, 304, 1917, 2004.

126. Chew, SY., Wen, Y., Dzenis, Y., Leong, KW., The Role of Electrospinning in the Emerging Field of Nanomedicine, Curr. Pharm. Des., 12, 4751, 2006.

127. Ellis-Behnke, RG., Liang, YX., You, SW., Tay, DK., Zhang, S., So, KF., Schneider, GE., Nano neuro knitting: Peptide nanofiber scaffold for brain repair and axon regeneration with functional return of vision, Proc. Natl. Acad. Sci. U S A,103, 5054, 2006.

128. McKee, MG., Layman JM., MP Cashion, TE Long, Phospholipid Nonwoven Electrospun Membranes, Science, 311, 353, 2006.

129. Bhattarai, N., Li, ZS., Edmondson, D., Zhang, M., Alginate-Based Nanofibrous Scaffolds: Structural, Mechanical, and Biological Properties, Advanced Materials,18, 1463, 2006.

130. Bhattarai, N., Edmondson, D., Veiseh, O., Matsen, FA., Zhang, M., Electrospun chitosan-based nanofibers and their cellular compatibility, Biomaterials, 26, 31, 6176, 2005.

131. Lutolf, MP., Hubbell, JA .,Synthetic biomaterials as instructive extracellular microenvironments for morphogenesis in tissue engineering, Nature Biotechnology, 23, 47, 2005.

132. Hollister, SJ., Porous scaffold design for tissue engineering, Nature Material, 4, 518, 2005.

133. Gross, RA., Kalra, B., Biodegradable Polymers for the Environment, Science, 297, 803-807, 2002.

134. Schmidt, CE ., Leach, JB., NEURAL TISSUE ENGINEERING: Strategies for Repair and Regeneration, Annu. Rev. Biomed. Engineeering, 5, 293, 2003.

135. Johnson, EO., Zoubos, AB., Soucacos, PN., Regeneration and repair of peripheral nerves, Injury, 36 Suppl., 4, S24, 2005.

136. Matsuda, A., Kagata, G., Kino, R., Tanaka, J., Preparation of chitosan nanofiber tube by electrospinning, J. Nanosci. Nanotechnol., 7, 852, 2007.

137. Chew, S., RMi, Y., Hoke, A., Leong, KW .,Aligned protein-polymer composite fibers enhance nerve regeneration: A potential tissue engineering platform, Advanced Functional Materials, 17,1288-1296, 2007.

138. Bini, TB., Gao, SJ., Tan, TC., Wang, S., Lim, A., Hai, LB., Ramakrishna, S., Electrospun poly(L-lactide-co-glycolide) biodegradable polymer nanofibre tubes for peripheral nerve regeneration Nanotechnology, 15, 1459, 2004.

139. Doolabh, VB., Hertl, MC., Mackinnon, SE., The role of conduits in nerve repair: a review, Reviews in the neurosciences, 7, 47-84, 1996.

140. Belkas, JS., Shoichet, MS., Midha, R., Peripheral nerve regeneration through guidance tubes, Neurol. Res., 26, 151, 2004; A. Cooper, N. Bhattarai, and M. Zhang “Fabrication and cellular compatibility of aligned chitosan-PCL fibers for nerve tissue regeneration", Carbohydrate Polymers, 85 (1), 149-156 (2011).

141. El-Hadi, A., Schnabel, R., Straube, E., Muller, G., Henning, S., Correlation between degree of crystallinity, morphology, glass temperature, mechanical properties and biodegradation of poly (3-hydroxyalkanoate) PHAs and their blends, Polymer Testing, 21, 665, 2002.

142. Honma, T., Zhao, L., Asakawa, N., Inoue, Y., Poly(ε-Caprolactone)/Chitin and Poly(ε-Caprolactone)/Chitosan Blend Films With Compositional Gradients: Fabrication and Their Biodegradability, Macromolecular Bioscience, 6, 241, 2006.

143. Yoshtyuki Nishio, RSJM., Blends of cellulose with nylon 6 and poly(ε-caprolactone) prepared by a solution-coagulation method, Polymer Engineering and Science, 30, 71, 1990.

144. Monzingo, AF., Marcotte, EM., Hart, PJ., Robertus, JD., Chitinases, chitosanases, and lysozymes can be divided into procaryotic and eucaryotic families sharing a conserved core, Nat. Struct. Biol., 3,133, 1996.

145. Rydevik, B., Lundporg, G., Olmarker, K., Myers, R., Basic biomechanics of the musculoskeletal system, (Eds: M. Nordin, V. H. Frankel), Lippincott Williams & Wilkins,Philadelphia 2001, xvii.

146. Tenchov, B., Koynova, R., Rapp, G., New Ordered Metastable Phases between the Gel and Subgel Phases in Hydrated Phospholipids, Biophysical Journal, Volume 80, April, 1873–1890, 2001.

147. Fukae, R ., Midorikawa, T., Preparation of gelatin fiber by gel spinning and its mechanical properties, Journal of Applied Polymer Science, 110 (6), 4011, 2008.

148. Kong, CS., Lee, TH., Lee, SH., Nano-web formation by the electrospinning at various electric fields, Journal of Materials Science, 42,19, 8106 , 2007.

149. Ma, PX., Elisseeff, J., Scaffolding in Tissue Engineering, First ed., CRC, 2005.

150. Smith, P., Lemstra, PJ., Ultra-high-strength polyethylene filaments by solution spinning/drawing, Journal of Materials Science,15, 2, 505,1980.

151. Smook, J., Pennings, AJ., Preparation of ultra-high strength polyethylene fibers by gel-spinning/hot-drawing at high spinning rates, Polymer Bulletin, 9, 1-3, 75, 1983.

152. Zhang, LF., Hsieh, YL., Carbon nanofibers with nano-porosity and hollow channels from binary polyacrylonitrile systems European Polymer Journal, 45, 1, 47, 2009.

153. Zhang, YZ., Su, B., Ramakrishna, S., Chitosan Nanofibers from an Easily Electrospinable for UHMWPEO- Doped Chitosan Solution System Biomacromolecules, 9, 1, 136, 2008.

154. Amrinder, SN., Wong, JC., Amon, C., Drawing suspended polymer micro-/nanofibers using glass micropipettes, Applied Physics Letters, 89, 18,183105 , 2006.

155. Ellis-Behnke, RG., Liang, Y-X., You, Si-W., Nano Neuro Knitting: Peptide Nanofiber Scaffold for Brain Repair and Axon Regeneration with Functional Return of Vision Nano Neuro Knitting: Peptide Nanofiber Scaffold for Brain Repair and Axon Regeneration with Functional Return of Vision, Proc. Natl. Acad. Sci., USA, 103, 13, 5054, 2006.

156. Ma, PX., Zhang, R., Synthetic nano-scale fibrous extracellular matrix, J. Biomed. Mater. Res., 46, 1, 60, 1999.

157. Mankidy, PJ., Rajagopalan, R., Foley, HC., Facile catalytic growth of cyanoacrylate nanofibers, Chem. Commun. (Camb), 14, 10, 1139, 2006.

158. Li, D., Xia, Y., Electrospinning of Nanofibers: Reinventing the Wheel, Advanced Materials, 16, 14,1151, 2004.

159. Sill, TJ., von Recum, HA., Electrospinning for Tissue Engineering and Drug Delivery, Biomaterials,29,13,1989-2006, 2008.

160. Teo, WE., Ramakrishna, S., A review on electrospinning design and nanofiber assemblies, Nanotechnology 17, 14, 89, 2006.

161. Bergshoef, MM., Vancso, GJ., Transparent Nanocomposites with Ultrathin, Electrospun Nylon-4,6 Fiber Reinforcement, Advanced Materials 11, 16, 1362, 1999.

162. Doshi, J., Reneker, DH., Electrospinning process and applications of electrospun fibers, Journal of Electrostatics, 35, 151, 1995.

163. Li, D., Wang, YL., Xia, YN., Electrospinning of Polymeric and Ceramic Nanofibers as Uniaxially Aligned Arrays, Nano Letters, 3, 8, 1167, 2003.

164. Soundarrajan, P., Patil, A., Dai, LM., Surface modification of aligned carbon nano tube arrays for electrochemical sensing applications, Journal of Vacuum Science and Technology 21, 4, 1198, 2003.

165. Xu, CY., Inai, R., Kotaki, M., Aligned biodegradable nanofibrous structure: a potential scaffold for blood vessel engineering, Biomaterials, 25, 5, 877, 2004.

166. Deitzel, JM., Kleinmeyer, J., Harris, D., The effect of processing variables on the morphology of electrospun nanofibers and textiles, Polymer, 42, 1, 261, 2001.

167. Dersch, R., Liu, TQ., Schaper, AK., Electrospun nanofibers: Internal structure and intrinsic orientation, Journal of Polymer Science Part a-Polymer Chemistry, 41, 4, 545, 2003.

168. Huang, ZM., Zhang, YZ., Kotaki, M., A review on polymer nanofibers by electrospinning and their applications in nano-composites, Compos. Sci. Technol., 63, 15, 2223, 2003.

169. Katta, P., Alessandro, M., Ramsier, RD., Continuous Electrospinning of Aligned Polymer Nanofibers onto a Wire Drum Collector, Nano Letters, 4, 11, 2215, 2004.

170. Theron, A., Zussman, E., Yarin, AL., Electrostatic field-assisted alignment of electrospun nanofibres, Nanotechnology, 12, 384, 2001.

171. Liu, L., Dzenis, Y., Analysis of the effects of the residual charge and gap size on electrospun nanofiber alignment in a gap method, Nanotechnology, 19 (355307), 2008; Li, D ., Wang, Y., Xia, Y., Electrospinning of Polymeric and Ceramic Nanofibers as Uniaxially Aligned Arrays, NANO LETTERS, 3, 8,1167-1171, 2003.

172. Gefter, PL., Stysis, VN., Measurements of electrical charge on moving dielectric fibers, Measurement Techniques, 21, 5, 683,1978.

173. Uyar, T., Besenbacher, F., Electrospinning of uniform polystyrene fibers: The effect of solvent conductivity, Polymer, 49, 24, 5336, 2008.

174. Gaumer, J., Prasad, A., Lee, D., Structure–function relationships and source-to-ground distance in electrospun polycaprolactone, Acta Biomaterialia, 5, 5, 1552, 2009.

175. Murugan, R., Ramakrishna, S., Design strategies of tissue engineering scaffolds with controlled fiber orientation, Tissue Eng., 13, 1845-1866 (2007); L Yao, N

O'Brien, A Windebank, A Pandit, Orienting neurite growth in electrospun fibrous neural conduits, J. Biomed. Mater. Res., B, Appl. Biomater., 90,483-491, 2009.

176. Martins, A., Araujo, JV., Reis, R., NM Neves, Electrospun nanostructured scaffolds for tissue engineering applications, Nanomedicine, 2, 6, 929-942, 2007; Agarwal, S., Wendorff, JH., Greiner, A., Use of electrospinning technique for biomedical applications, Polymer, 49, 26 ,5603-5718.

177. Teo, WE., Ramakrishna, S., A review on electrospinning design and nanofiber assemblies, Nanotechnology, 17, 14, R89-R106, 2006; Teo, WE., Inai, R., Ramakrishna, S.,Technological advances in electrospinning of nanofibers, Sci. Technol. Adv. Mater., 12, 013002, 2011.

178. Yarin, AL., Koombhongse, S., Reneker, DH., Bending instability in electrospinning of nanofibers, Journal of Applied Physics, 89, 3018-3026, 2001.

179. Menon, A., Somasekharan, K., Velocity- acceleration and jerk in electrospinning, The Internet Journal of Bioengineering, Volume 4, Number 2, 2009.

180. Yuan, Y., Zhang, P., Yang, Y., Wang, X., Gu, X., The interaction of Schwann cells with chitosan membranes and fibers in vitro, Biomaterials, 25,18, 4273-4278, 2004.

181. Weiner, JA., Fukushima, N., Contos, JJ., Scherer, SS., J Chun, Regulation of Schwann cell morphology and adhesion by receptor-mediated lysophosphatidic acid signaling, J. Neuroscience, 21, 18, 7069-7078, 2001.

182. Bryan, DJ., Holway, AH., Wang, KK., Silva, AE., Trantolo, DJ., Wise, D., Summerhayes, IC., Influence of glial growth factor and Schwann cells in a bioresorbable guidance channel on peripheral nerve regeneration, Tissue Engineering, 6, 2, 129-38, 2000.

183. Weyland, JA., Patterson, JD., Rotating water sprinkler, American Journal of Physics, 44, 11, 1106-1109, November 1976.

184. Pham, QP., Sharma, U., Mikos, AG., Electrospinning of Polymeric Nanofibers for Tissue Engineering Applications: A Review, Tissue Eng., 12, 1197, 2006.

185. Nukavarapua Kumbara, SG., Jamesb, SP., Hogana, R., Laurencin, MV., Recent Patents on Biomedical Engineering 1, 68, 2008.

186. Greiner, A., Wendorff, JH., Electrospinning: A Fascinating Method for the Preparation of Ultrathin Fibers, Angew. Chem., Int. Ed. 46, 5670, 2007).

187. Naraghi, M., Chasiotis, I., Kahn, H., Wen, Y., Dzenis, Y., Novel method for mechanical characterization of polymeric nanofibers, Rev. Sci. Instrum. 78, 085108, 2007.

188. Tan, EPS., Lim, CT., Mechanical characterization of nanofibers – A review, Compos. Sci. Technol. 66, 1102, 2006.

189. Hemker, KJ., Sharpe, WN., Microscale Characterization of Mechanical Properties, Annu. Rev. Mater. Res. 37, 93, 2007.

190. Li, XD., Hao, HS., Murphy, CJ., Caswell, KK., Nanoindentation of Silver Nanowires, Nano Lett. 3,1495, 2003.

191. VanLandingham, MR., Villarrubia, JS., Guthrie, WF., Meyers, GF., Nanoindentation of polymers: an overview, Macromol. Symp. 167, 15, 2001.

192. Johnson, KL., Kendall, K., Roberts, AD., Surface Energy and the Contact of Elastic Solids, Proc. R. Soc. London, Ser. A, 324, 301, 1971.

193. Ko, F., Gogotsi, Y., Ali, A., Naguib, N., Ye, HH., Yang, GL ., Li, C., Willis, P., Electrospinning of Continuous Carbon Nanotube-Filled Nanofiber Yarns, Adv. Mater., (Weinheim, Ger.) 15, 14, 1161, 2003.

194. Tan, EPS., Goh, CN., Sow, CH., Lim, CT., Tensile test of a single nanofiber using an atomic force microscope tip, Appl. Phys. Lett. 86, 073115, 2005.

195. Yuya, PA., Wen, YK., Turner, JA., Dzenis, YA., Li, Z .,Determination of Young's modulus of individual electrospun nanofibers by microcantilever vibration method,

196. Boussaad, S., Tao, NJ., Polymer Wire Chemical Sensor Using a Microfabricated Tuning Fork, Nano Lett. 3, 1173, 2003.

197. Wu, B., Heidelberg, A., Boland, JJ., Mechanical properties of ultrahigh-strength gold nanowires, Nature Materials, 4, 525, 2005.

198. Li, D., Wang, YL., Xia, YN., Electrospinning of Polymeric and Ceramic Nanofibers as Uniaxially Aligned Arrays, Nano Lett., 3, 1167, 2003.

199. Bellan, LM., Kameoka, J., Craighead, HG., Measurement of the Young's moduli of individual polyethylene oxide and glass nanofibers, Nanotechnology 16, 1095, 2005.

200. Edmondson, D., Bhattarai, N., Jana, S., Kim, A., Zhang, M., Design and evaluation of a nanoscale differential tensile test device for nanofibers, Appl. Phys. Lett. 94, 103101, 2009.

201. Tripathy, T., Pankey, SR., Karmaker, NC., Bhagat, RP., Singh, RP., European Polymer Journal, 35, 2057, 1999; Bhattarai, N., Li, ZS., Edmondson, D., Zhang, M., Alginate-Based Nanofibrous Scaffolds: Structural, Mechanical, and Biological Properties, Advanced Materials,18, 1463, 2006.

202. Hamano, T., Chiba, D., Teramoto, A., Kondo, Y., Abe, K., Effect of polyelectrolyte complex (PEC) on human periodontal ligament fibroblast functions in the presence of glucocorticoids, J. Biomater. Sci. Polymer Ed., 9, 985-1000,1998.

203. Axelsson, M., Pitsillides, K., Munns, S., Hicks, J.W., A biotelemetry implant for measurement of blood flow, blood pressure, ECG and temperature. Faseb Journal 20(5), A1198-A1198, 2006.

204. Brian, M., Phillip, G., Alan, M., Skeletal Muscle: Form and Function, 2nd ed. Human Kinetics, 2005.

205. Chang, C.-L., Chang, C.-W., Hsu, C.-M., Luo, C.-H., Chiou, J.-C., Power-efficient wireless sensor for physiological signal acquisition. Journal of Micro-Nanolithography Mems and Moems 8(2), 2009a.

206. Chang, C., Fuh, Y-K., Lin, L., A direct-write piezoelectric PVDF Nanogenerator, Solid-State Sensors, Actuators and Microsystems Conference, 2009. TRANSDUCERS 2009,1485 – 1488, 21-25 June 2009b.

207. Donaldson, M.R., Arlinghaus, R., Hanson, K.C., Cooke, S.J., Enhancing catch-and-release science with biotelemetry. Fish and Fisheries 9(1), 79-105, 2008.

208. Edmondson, D., Bhattarai, N., Jana, S., Kim, A., Zhang, M., Design and evaluation of a nanoscale differential tensile test device for nanofibers. Applied Physics Letters 94(10), 2009.

209. Edmondson, D., Cooper, A., Jana, S., Wood, D., Zhang, M., Centrifugal electrospinning of highly aligned polymer nanofibers over a large area. Journal of Materials Chemistry 22, 18646-18652, 2012.

210. Ferguson, J.E., Redish, A.D., Wireless communication with implanted medical devices using the conductive properties of the body. Expert Review of Medical Devices 8(4), 427-433, 2011.

211. Grans, A., Axelsson, M., Pitsillides, K., Olsson, C., Hojesjo, J., Kaufman, R.C., Cech, J.J., Jr., A fully implantable multi-channel biotelemetry system for measurement of blood flow and temperature: a first evaluation in the green sturgeon. Hydrobiologia 619, 11-25, 2009.

212. Hsu, C.-M., Liao, W.-Y., Luo, C.-H., Chou, T.-C., The 2.4 GHz biotelemetry chip for healthcare monitoring system. Sensors and Actuators a-Physical 139(1-2), 245-251, 2007.

213. Jung, J., Zhu, S., Liu, P., Chen, Y.-J.E., Heo, D., 22-pJ/bit Energy-Efficient 2.4-GHz Implantable OOK Transmitter for Wireless Biotelemetry Systems: In Vitro Experiments Using Rat Skin-Mimic. Ieee Transactions on Microwave Theory and Techniques 58(12), 4102-4111, 2010.

214. Keuchle, V.B., State of the art of biotelemetry in North America. Symposia of the Zoological Society of London 49, 1-18, 1982.

215. Kiourti, A., Nikita, K.S., A Review of Implantable Patch Antennas for Biomedical Telemetry: Challenges and Solutions. Ieee Antennas and Propagation Magazine 54(3), 210-228, 2012.

216. LH, O., The heart physiology: From cell to circulation 3rd ed. Lippincot-Raven, Philadelphia, 1998.

217. Liu, W.-C., Yeh, F.-M., Ghavami, M., Miniaturized implantable broadband antenna for biotelemetry communication. Microwave and Optical Technology Letters 50(9), 2407-2409, 2008.

218. Valdastri, P., Susilo, E., Foerster, T., Strohhoefer, C., Menciassi, A., Dario, P., Wireless Implantable Electronic Platform for Chronic Fluorescent-Based Biosensors. Ieee Transactions on Biomedical Engineering 58(6), 1846-1854, 2011.

219. Weiss, M.D., Smith, J.L., Bach, J., RF Coupling in a 433-MHz Biotelemetry System for an Artificial Hip. Ieee Antennas and Wireless Propagation Letters 8, 916-919, 2009.

220. Wong, A.C.W., Kathiresan, G., Chan, C.K.T., Eljamaly, O., Omeni, O., McDonagh, D., Burdett, A.J., Toumazou, C., A 1 V wireless transceiver for an ultra-low-power SoC for biotelemetry applications. Ieee Journal of Solid-State Circuits 43(7), 1511-1521, 2008.

221. Tang, L., Yang, Y., Soh, CK., Toward Broadband Vibration-based Energy Harvesting, Journal of Intelligent Material System and Structure, 21(18) 1867-1897, 2010.

222. Roundy, S., Wright, PK., Rabaey, J., A study of low level vibrations as a power source for wireless sensor nodes, Computer Communications, 26(11) 1131-114, 2003.

223. Chen, YY., Vasic, D., Costa, F., Wu, WJ., Lee, CK., 7-10, Self-powered Piezoelectric Energy Harvesting, IEEE IECON 2010, Phoenix, Arizona, USA, November 2010.

224. Liu, YP., Vasic, D., Costa, F., Piezoelectric Energy Harvester Circuit for Capacitive Storage Buffer, Electrimacs 2011, June 6-8, Paris, France, 2011.

225. Cooper, A., Bhattarai, N., Zhang, M., Fabrication and cellular compatibility of aligned chitosan-PCL fibers for nerve tissue regeneration, Carbohydrate Polymers, 85 (1), 149-156, 2011.

226. **Edmondson, D**., Jana, S., Wood, D., Fang, C., Zhang, M., Uniaxially-aligned nanofibers as sensor and transmitter for biotelemetry", Analyst, 138 (23), 7135-7139, 2013.

227. Yang, R., Qin, Y., Dai, L., Wang, ZL., Power generation with laterally packaged piezoelectric fine wires, Nature Nanotechnology 4, 34 – 39, 2009.

PUBLICATIONS

(Research papers associated with)

T. Low, M. Leung, X. Wang, J. J. F. Chang, C. T. Tsao, J. Sham, **D. Edmondson**, and M. Zhang “Bi-layer scaffold of chitosan/PCL-nanofibrous mat and PLLA-microporous disc for skin tissue engineering", Journal of Biomedical Nanotechnology, accepted.

F. M. Kievit, A. Cooper, S. Jana, M. C. Leung, K. Wang, **D. Edmondson**, D. Wood, J. S. H. Lee, R. G. Ellenbogen, and M. Zhang “Aligned chitosan-polycaprolactone polyblend nanofibers promote the migration of glioblastoma cells", Advanced Healthcare Materials, (accepted).

D. Edmondson, S. Jana, D. Wood, C. Fang, and M. Zhang “Uniaxially-aligned nanofibers as sensor and transmitter for biotelemetry", Analyst, 138 (23), 7135-7139 (2013).

D. Edmondson, A. Cooper, S. Jana, D. Wood, and M. Zhang “Centrifugal Electrospinning of Highly-Aligned Polymer Nanofibers over Large Area", Journal of Materials Chemistry, 22 (35), 18646-18652 (2012)

Dennis Edmondson, Narayan Bhattarai, Soumen Jana, Abraham Kim, and Miqin Zhang, Design and evaluation of a nanoscale differential tensile test device for nanofibers, APPLIED PHYSICS LETTERS 94, 103101, 2009.

Narayan Bhattarai, Zhensheng Li, Jonathan Gunn, Matthew Leung, Ashleigh Cooper, **Dennis Edmondson**, Omid Veiseh, Ming-Hong Chen, Yong Zhang, Richard G. Ellenbogen, and Miqin Zhang, Natural-Synthetic Polyblend Nanofibers for Biomedical APPLICATIONS, ADVANCED MATERIALS, 21, 1–6, 2009.

Fareid Asphahani, Myo Thein, Omid Veiseh, **Dennis Edmondson**, Ryan Kosai, Mandana Veiseh, Jian Xub, Miqin Zhang, Influence of cell adhesion and spreading on impedance characteristics of cell-based sensors, BIOSENSORS AND BIOELECTRONICS 23, 1307–1313, 2008.

Caroline Dang, Narayan Bhattarai, **Dennis Edmondson**, Ashleigh Cooper, Miqin Zhang, Aligning poly(L-lactic acid) nanofibers with magnetic Fe_3O_4 nanoparticles using modified electrospinning methods, JOURNAL OF UNDERGRADUATE RESEARCH IN BIOENGINEERING 29

Narayan Bhattarai, Zhensheng Li, **Dennis Edmondson**, and Miqin Zhang, Alginate-Based Nanofibrous Scaffolds: Structural, Mechanical, and Biological Properties, ADVANCED MATERIALS, 18, 1463–1467, 2006.

Narayan Bhattarai, **Dennis Edmondson**, Omid Veiseh, Frederick A. Matsen, Miqin Zhang, Electrospun chitosan-based nanofibers and their cellular compatibility, BIOMATERIALS 26, 6176–6184, 2005.